1991

A superconducting compact hydrogen maser resonator

David B. Opie
College of William & Mary - Arts & Sciences

INFORMATION TO USERS

This manuscript has been reproduced from the microfilm master. UMI films the text directly from the original or copy submitted. Thus, some thesis and dissertation copies are in typewriter face, while others may be from any type of computer printer.

The quality of this reproduction is dependent upon the quality of the copy submitted. Broken or indistinct print, colored or poor quality illustrations and photographs, print bleedthrough, substandard margins, and improper alignment can adversely affect reproduction.

In the unlikely event that the author did not send UMI a complete manuscript and there are missing pages, these will be noted. Also, if unauthorized copyright material had to be removed, a note will indicate the deletion.

Oversize materials (e.g., maps, drawings, charts) are reproduced by sectioning the original, beginning at the upper left-hand corner and continuing from left to right in equal sections with small overlaps. Each original is also photographed in one exposure and is included in reduced form at the back of the book.

Photographs included in the original manuscript have been reproduced xerographically in this copy. Higher quality 6" x 9" black and white photographic prints are available for any photographs or illustrations appearing in this copy for an additional charge. Contact UMI directly to order.

U·M·I

University Microfilms International
A Bell & Howell Information Company
300 North Zeeb Road, Ann Arbor, MI 48106-1346 USA
313/761-4700 800/521-0600

Order Number 9219101

A superconducting compact hydrogen maser resonator

Opie, David B., Ph.D.

The College of William and Mary, 1991

U·M·I

300 N. Zeeb Rd.
Ann Arbor, MI 48106

A SUPERCONDUCTING COMPACT HYDROGEN MASER RESONATOR

A Dissertation

Presented to

The Faculty of the Department of Physics

The College of William and Mary in Virginia

In Partial Fulfillment

Of the Requirements for the Degree of

Doctor of Philosophy

---

by

David B. Opie

1991

APPROVAL SHEET

This dissertation is submitted in partial fulfillment of the

requirements for the degree of

Doctor of Philosophy

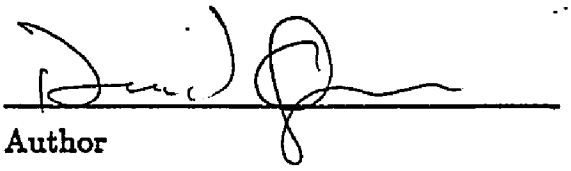

Author

Approved, November 1991

Harlan E. Schone

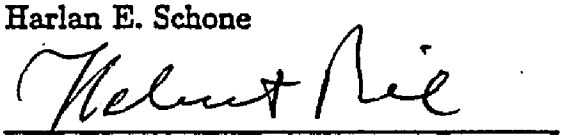

H. Piel

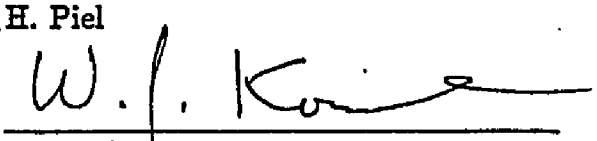

William J. Kossler

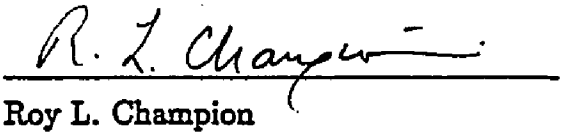

Roy L. Champion

Vincent J. Folen
Naval Research Laboratory, Wash. D.C.

TABLE OF CONTENTS

Page

ACKNOWLEDGEMENTS

The author wishes to thank all those who helped in creating this work. From the University of Wuppertal, Dr. Piel, Matthias Hein, and Frau Zelesko all deserve special thanks for their support. From the Naval Research Laboratory, Vince Folen, Mike Golding and Alick Frank have all been very helpful in offering their expertise and advice on topics herein. At William and Mary, Dr. Schone and the rest of the department have provided the environment that made the last several years enjoyable.

My wife has always been supportive and offered encouragement.

LIST OF TABLES

Table Page

LIST OF FIGURES

ABSTRACT

The discovery of high critical temperature superconductors (HTSC) has raised the temperature at which the greatly reduced surface resistance, characteristic of superconducting materials, may be exploited. For microwave frequencies below 100 GHz, the surface resistance, R_s, at liquid nitrogen temperatures ($77K$) of the new HTSC materials is found to be better than copper measured at the same temperature and frequency. Consequently, the miniaturization of passive microwave components will be among the first applications of these new materials. This dissertation details the development, testing and evaluation of a superconducting compact hydrogen maser resonator made from electrophoretic $Y_1Ba_2Cu_3O_{7-\delta}$ (YBCO). Such a resonator could sustain active maser oscillation and would therefore be a an excellent compact frequency source. This compact maser could yield significant volume and weight savings for space applications where masers are used as frequency standards. The compact resonator is a loop-gap (split-ring) lumped element resonator similar to that previously suggested for compact maser applications. This resonator is made superconducting using an electrophoretic process developed for the deposition of thick film polycrystalline HTSC on large non-planar metallic substrates. The low R_s of the YBCO deposited onto the surface of the electrode loading structure, inside of the loop-gap resonator, yields cavity quality factors comparable to those of the much larger TE_{011} maser resonator but in a much smaller package. The fields

of the loop-gap resonator are uniform in the hydrogen interaction region. However, in the neighborhood of the electrodes, the fields are analogous to the TEM fields associated with stripline geometries. These microwave fields have been investigated by numerical analysis and the dependence of the filling factor, (η') and the cavity quality factor, (Q_c), as a function of the cavity dimensions is discussed. With this information, the cavity design has been optimized to find the cavity size and shape that will yield the lowest Allan deviation with respect to the random thermal frequency fluctuations.

A SUPERCONDUCTING COMPACT HYDROGEN MASER RESONATOR

CHAPTER 1

1 Introduction

With the discovery of high critical temperature superconductors (HTSC), development of a new class of superconducting devices which operate at $77K$ is now feasible. This opens new opportunities for commercial application as existing superconducting devices are re-developed with HTSC material and new devices are invented. The miniaturization of microwave components has become one of the first applications of these new materials. Using the HTSC materials, miniaturized antennae [1], filters [2], stripline [2] and cavity [16] resonators have been developed and tested.

To stimulate and support research and production of HTSC devices, the Naval Research Laboratory has sponsored the High Temperature Superconducting Space Experiment (HTSSE). During this test, superconducting devices will be placed aboard a satellite scheduled for future launch and monitored throughout the space flight to determine the effects of space environment on the HTSC materials. Two loop-gap cavities (described in this thesis) have been constructed, tested and delivered to NRL for this program; one of which will be assembled into the satellite test system.

One particularly interesting application of HTSC's is the construction of a compact superconducting hydrogen maser resonator. It has been reported that a

loop-gap resonator is well suited as a miniaturized hydrogen maser resonator [3]. However, as the size of the resonator is reduced, the resonator quality factor is also reduced. The reduction of the quality factor is enough that such a maser cannot sustain self oscillation. The suggested solution is that the compact maser resonator be constructed from the HTSC $Y_1Ba_2Cu_3O_{7-\delta}$(YBCO) [4]. If the cavity quality factor of the superconducting maser resonator were nearly as large as the full size TE_{011} maser resonator quality factor, then the maser could sustain self oscillation.

The motivation to reduce the size of a hydrogen maser comes from the unique capability of a hydrogen maser to provide a very stable frequency based on the fundamental transition frequency between the hydrogen hyperfine states. A stable frequency source is the heart of navigation systems like the Navstar Global Positioning System (GPS) , coordinated very long baseline interferometry (VLBI) and time keeping standards. The size and weight of a ground based frequency source is not as critical as the size and weight of space based frequency sources. The economics of launching full size hydrogen frequency standards for programs like GPS is prohibitive. The largest component of a full size hydrogen maser is the TE_{011} $1.420GHz$ cylindrical cavity resonator with its vacuum container and magnetic shields. These components form a cylindrical package $45cm$ in diameter and about $50cm$ tall. Currently, GPS uses cesium frequency standards that are significantly smaller than masers but are also less stable. Whereas masers have a fractional frequency stability of parts in 10^{16}, a small cesium standard is stable to parts in 10^{13}. By using the compact maser resonator, the cylindrical cavity would

be about $10cm$ in length and diameter but with the stability of a hydrogen maser, as will be shown in this dissertation.

This compact resonator is a loop-gap (split-ring) lumped element resonator similar to that suggested for compact maser applications [3]. This resonator is made superconducting using an electrophoretic process developed for the deposition of thick film polycrystalline HTSC on large non-planar metallic substrates [24]. As a result of this thesis, the low surface resistance, R_s, of the YBCO deposited onto the surface of the electrode loading structure inside of the loop-gap resonator was found to yield cavity quality factors comparable to those of the much larger TE_{011} maser resonator but in a much smaller package. The rf magnetic fields of the loop-gap resonator are uniform in the hydrogen interaction region. However, in the neighborhood of the electrodes, the fields are analogous to the TEM fields associated with stripline geometries. These microwave fields have been investigated by numerical analysis and relationships for the filling factor, η' and the cavity quality factor, Q_c were calculated as a function of the cavity dimensions. Given this information, the cavity design may be optimized to find the cavity size and shape that will yield the lowest Allan deviation with respect to the random thermal frequency fluctuations.

The HTSC material YBCO is superconducting at temperatures below the $92K$ critical temperature. To operate the maser with the superconducting resonator the maser parameters for this temperature environment need to be calculated and the effects that these will have on maser performance must be addressed. To date,

there are no operating masers at liquid nitrogen temperatures although this has been attempted [5,6]. The challenge for $77K$ masers lies in the solution of the temperature control problem. It is the interaction of the hydrogen with the teflon surfaces in the maser that make the $77K$ maser especially sensitive to temperature fluctuations. Consequently, the temperature control requirements have been calculated for the particular geometry of the loop-gap resonator design.

At the time that this work began, there existed reports in literature about compact hydrogen maser development, the effects of teflon and hydrogen in a $77K$ maser were already measured, the fields of the loop-gap resonator were still under investigation and the HTSC's were new and not as well characterized as they are today. In this document, all of these topics are brought together to solve one problem: is the development of a high precision oscillating compact hydrogen maser feasible using the HTSC materials.

In the following, the development, testing and evaluation of a superconducting compact maser resonator made from electrophoretic YBCO are described. The topics of superconductivity, hydrogen masers and stability measurements are introduced in section 2. In section 3, the construction and electrophoretic deposition for the loop-gap resonator are described and the measured results are given. Section 4 covers the evaluation of the loop-gap resonator as a maser resonator at $77K$. This includes noise measurements, frequency shifts and relaxation rate calculations and the calculated frequency sensitivity of temperature fluctuations. In section 5, the electromagnetic fields of the loop-gap resonant mode are described and from

these field descriptions, the loop-gap design is optimized with respect to frequency stability. Section 6 summarizes the results and conclusions from this work.

CHAPTER 2

2.1 Superconductivity

Superconductivity was first discovered by H. Kamerlingh Onnes, more than eighty years ago [68]. What he discovered was the complete loss of dc resistance in a metallic sample when the temperature of the sample was lowered below a critical transition temperature, T_c. This zero resistivity phenomenon has since been found to be a property of most of the non-magnetically ordered metals and thousands of alloys [7]. The properties of superconductors are: zero resistivity for currents below a critical value, J_c, and perfect diamagnetism in applied fields that are not above a critical field value, H_c [7].

Before 1986, superconductivity was strictly a low temperature phenomenon in which the highest T_c's were near $20K$. The discovery by Bednorz and Mueller of a new class of superconductors has led to the development of materials with T_c's up to $125K$ [8,72]; which is well above the $77K$ boiling point of liquid nitrogen. For application, the HTSCs offer the reduced losses and persistent currents found in low temperature superconductors but without the required expense of liquid helium cryogenics.

Some of the first applications of the HTSC materials will be as passive microwave components [1,9]. From this class of high temperature superconductors, YBCO ($T_c = 92K$) is often preferred for application because of its phase purity

and sharp rf transition [9]. At low power levels, polycrystalline YBCO has already been measured to have lower rf losses than copper at $77K$ and at frequencies below $50GHz$ [10].

Generally, the HTSC's (YBCO) are manufactured as either bulk material, thick films or thin films. The bulk material is the sintered ceramic superconductor consisting of randomly oriented grains. Bulk material is not a likely candidate for applications because the oxide superconductor material is difficult to produce, machine, and handle in the ceramic form. Thick films use the mechanical properties of the substrate for form and strength. These films are granular but can be textured in a variety of ways (electrophoretic magnetic texturing [24], melt texturing on zirconia [10], or 'sinter texturing' on silver [28], to name a few). Since the HTSCs are anisotropic, the orientaion is designed to take advantage of the superior current carrying properties of the crystallographic $a - b$ plane. The texturing of the thick films orients the c-axis of the material perpendicular to the plane in which the dc or rf currents will flow,.thereby improving the superconducting properties. In general, the thin films are highly oriented epitaxial films on single crystal substrates. The thin films have fewer defects and grain boundaries than the thick films, as the substrate surface orients the superconducting crystal axes by matching the substrate and film lattice spacing.

The thin films exhibit the best superconducting properties of the three types mentioned above [70]. The thin films on single crystal substrates show great potential for applications to planar passive microwave components. The lowest surface

resistance, dc magnetic field sensitivity, rf power sensitivity and the highest current carrying capacity is measured with thin films. Unfortunately, with today's level of technology, the thin films are restricted to planar structures. Therefore, for application to large non-planar surfaces, textured thick films are the best alternative.

In this introduction, properties of superconductors are reviewed and a phenomenological two fluid model is described [69]. This two fluid model takes into account the granular nature of the HTSC materials. The grains and grain boundaries are described by lumped element circuit components that represent the inductive and resistive nature of the material. This model will be needed to interpret the response of the maser resonator to magnetic microwave fields at the surface of the YBCO (section 3.2).

Two Fluid Model

This development of the two fluid model can be used to describe the electrodynamic behavior of the granular superconductors. In superconductors, it is presumed that a fraction of the electrons are in the low energy superconducting state and that these superconducting electrons do not make collisions. It is further assumed that the characteristic lengths of the material are related by, $\xi, l \ll \lambda_l$. ξ is the spatial range of phase coherence of the superconducting electron wave function, l is the electron mean free path, and λ_l is the depth of field penetration into a superconductor. With these assumptions, the depth of field penetration is much larger than characteristic lengths of either the normal or superconducting electrons and local electrodynamics may be used.

The fields are limited to the penetration depth because the motion of the superconducting electron pairs screen the fields from entering the superconductor. If there is no damping effects retarding the motion of the superconducting charge carriers, then one may write [11],

$$m^* \frac{d\vec{v}}{dt} = e^* \vec{E} \ , \tag{2.1.1}$$

where m^* and e^* are the mass and charge of the paired electrons, respectively and $\vec{E}$ is the field induced in the surface of the superconductor. When n_s is the number density of the superconducting charge carriers, the current density of the superconducting electrons can be written as

$$\vec{J}_s = n_s e^* \vec{v} \ . \tag{2.1.2}$$

Combining equations (2.1.1) and (2.1.2) yields

$$\vec{E} = \Lambda \frac{d\vec{J}_s}{dt} \ , \tag{2.1.3}$$

where

$$\Lambda = \frac{m^*}{n_s e^{*2}} = \mu_o \lambda_L^2 \ , \tag{2.1.4}$$

where λ_L is the London penetration depth.

The above results can be used to explain the dc resistivity measured in superconductors. For dc currents, the superconducting current will be time independent and the derivative in equation (2.1.3) will equal zero, implying that $\vec{E} = 0$. Since ohmic losses can be described by the normal electron current density J_n and Ohm's law,

$$\vec{J}_n = \sigma_n \vec{E} \ , \tag{2.1.5}$$

a time independent J_s implies that $J_n = 0$. Thus, dc currents are carried completely by the superconducting electrons.

When the time dependence of the fields is sinusoidal with freequency ω, equation (2.1.3) becomes

$$\vec{E} = \Lambda(i\omega)\vec{J}_s \ . \tag{2.1.6}$$

Equation (2.1.6) can be interpreted in terms of Ohm's law,

$$\vec{J}_s = i\sigma_s\vec{E} = -i\left(\frac{n_s e^{*2}}{\omega m^*}\right)\vec{E} \ , \tag{2.1.7}$$

where σ_s is the superconducting conductivity. In general, there will be normal conducting electrons as well as superconducting electrons. The total current density

$$\vec{J} = \vec{J}_n + \vec{J}_s \ , \tag{2.1.8}$$

where $\vec{J}_n$ is the normal conducting current density. Including the normal conducting electrons in equation (2.1.7) yields,

$$\vec{J} = (\sigma_n - i\sigma_s)\vec{E}; \quad \sigma_n = \frac{n_n e^2 \tau}{m} \ , \tag{2.1.9}$$

and σ_n is in the familiar form of the Drude model of conductivity. The complex conductivity of the superconductor can be defined as

$$\sigma = \sigma_n - i\sigma_s = \frac{n_n e^2 \tau}{m} - i\frac{n_s e^{*2}}{m^*\omega} \ , \tag{2.1.10}$$

where each term describes a 'fluid' of electrons in the metal and thus a two fluid model. This approach is valid in the local limit, where the spatial range of phase coherence in the superconducting electron wave function is small compared to the London penetration depth [9].

The behavior of superconductors in high frequency electro-magnetic fields can be characterized by the surface impedance Z_s, where [32]

$$Z_s \equiv \frac{E_\parallel}{H_\parallel} = \left(\frac{i\omega\mu}{\sigma}\right)^{1/2} . \tag{2.1.11}$$

Equation (2.1.10) can be used to separate Z_s into real and imaginary components, such that

$$Z_s = R_s - iX_s . \tag{2.1.12}$$

When $\sigma_s \gg \sigma_n$, X_s is the surface reactance and can be written as

$$X_s \simeq \omega\mu_o\lambda_L , \tag{2.1.13a}$$

and R_s is the surface resistance,

$$R_s \simeq \frac{1}{2}\mu_o^2\omega^2\lambda_L^3\sigma_n . \tag{2.1.13b}$$

From equation (2.1.13b) the frequency dependence of the surface resistance is found to be proportional to ω^2, which is the expected result. Also, the surface resistance will be proportional to the the number density of normal electrons through the σ_n term ($\sigma_n \sim n_n$).

The temperature dependence of the surface impedance is a result of the temperature dependence of λ_L and σ_n. Close to T_c, the temperature dependence of n_n can be obtained from the Gorter and Casimir model with n_n proportional to t^4, where t is the reduced temperature $t = T/T_c$ [68]. This gives the temperature dependence of the London penetration depth as

$$\lambda_L(T) = \frac{\lambda_L(0)}{\sqrt{1-t^4}} ; \quad . \tag{2.1.14}$$

For the low temperature superconductors (i.e. Nb, Pb, Hg, ...) the surface resistance drops about two orders of magnitude as the temperature is lowered from the normal state to just below T_c. This sharp decrease in R_s is a result of the penetration depth being much smaller than the normal state skin depth. As the temperature is decreased further, λ_l becomes constant but the surface resistance follows the exponential temperature dependence of the normal electrons condensing to the lower energy state according to the Boltzman factor $e^{\frac{\Delta}{k_b T}}$. Here Δ is the electron excitation energy. As $T \rightarrow 0$, R_s reaches a level of residual resistance that is nearly temperature independent [9]. At the lower temperatures, $\sigma_s \gg \sigma_n$ and this two fluid model remains valid [9].

For the HTSC material, the condition that the imaginary part of the conductivity is much greater than the real part is not clearly met in every circumstance. In the HTSC materials there is a large residual R_s component that can remain finite and quite large even at $4.2K$. At $21GHz$ and $4.2K$ a magnetically textured electrophoretic sample was measured and found to have real and imaginary conductivity components of similar magnitude ($\sigma_n = 1.1 \times 10^7/\Omega m$ and $\sigma_s = 3.9 \times 10^7/\Omega m$) [9]. The measurement of R_s and X_s is detailed in reference [9].

For the evaluation of the hydrogen maser resonator, the frequency of interest is $1.42GHz$. According to equation (2.1.10), σ_n is independent of frequency while σ_s is inversely proportional to ω. Therefore, if the sample measured at $21GHz$ was then measured at $1.42GHz$, σ_s should be about 15 times larger, while σ_n would remain the same.

The large residual R_s in the HTSC material is quite likely caused by the granularity and defects in the bulk of the material [9]. All of the HTSC materials are more sensitive to applied dc and rf magnetic fields than the LTSC's. Evidence that grain boundaries are at least partially responsible for the R_s is found by comparing single crystalline thin films of YBCO and polycrystalline thick YBCO films. The surface resistance of single crystalline films show little or no magnetic field dependence, whereas the R_s of polycrystalline films is very sensitive to the presence of fields [9]. The grain boundaries are presumed to act as Josephson junctions whose critical current is a function of the applied magnetic field [69]. Therefore, the two fluid model above cannot describe this behavior and needs to be augmented to include this effect.

A phenomenological supplement to the two fluid model has been proposed by A. Portis and M. Hein for polycrystalline materials [69]. This supplement is expected to be valid in temperature regions where the grain boundary contribution to the losses is dominant. In this model, the grain boundaries, influence of rf fields and the effects of dc fields have been considered. The response of the superconductor is modelled as a lumped element circuit whose inductivity and resistivity describes the macroscopic response of the material [69]. The effective medium inductivity and resistivity are given in terms of the effective medium penetration depth λ_2, the macroscopic critical current J_c, grain diameter d and Josephson junction inductivity l_j.

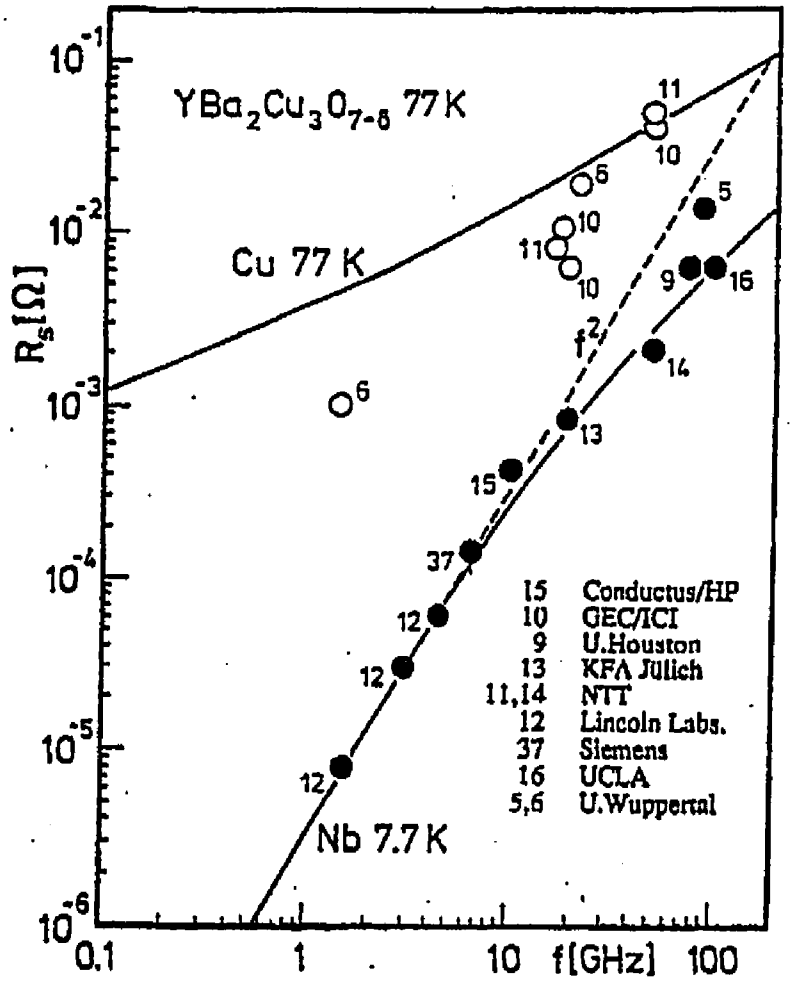

Figure 2.1.1 Best published results of YBCO on $LaAlO_3$ (full circles) compared with textured thick YBCO films (open circles). The point labled as number 6 refers to refers to the superconducting electrodes used in the compact maser resonator. The other references are listed elsewhere [73].

According to this model, Z_s can be written as [69],

$$Z_s = -i\omega\mu_o\lambda_2\left(1+\frac{iH_{rf}}{\lambda_2 J_c}\right)^{1/2} \quad , \tag{2.1.15}$$

where λ_2 is the macroscopic penetration depth due to Josephson junctions (grain boundaries), and J_c is the macroscopic critical current. When H_{rf} is small, equation (2.1.15) can be expanded for low rf surface magnetic fields H_{rf} yielding,

$$R_s \approx \frac{\omega\mu_o H_{rf}}{2J_c} \ , \tag{2.1.16}$$

and

$$X_s \approx -i\omega\mu_o\lambda_2\left[1+1/8\left(\frac{H_{rf}}{\lambda_2 J_c}\right)^2\right] \ . \tag{2.1.17}$$

As H_{rf} is increased, then the change in X_s will be much smaller than the change in R_s and therefore, the slope of the change of R_s versus X_s is

$$\frac{\Delta X_s}{\Delta R_s} = \frac{1}{4}\frac{H_{rf}}{\lambda_2 J_c} \ll 1 \ . \tag{2.1.18}$$

For very high fields, equation (2.1.15) can be expanded to give [69],

$$R_s \approx \omega\mu_o\left(\frac{\lambda_2 H_{rf}}{2J_c}\right)^{1/2}\left[1-\frac{1}{2}\left(\frac{2\lambda_L l_j J_c}{d\mu_o\lambda_2 H_{rf}}\right)^2\right] \ , \tag{2.1.19}$$

and

$$X_s \approx \omega\mu_o\left(\frac{\lambda_2 H_{rf}}{2J_c}\right)^{1/2}\left[1+\frac{1}{8}\left(\frac{2\lambda_L l_j J_c}{d\mu_o\lambda_2 H_{rf}}\right)^2\right] \ . \tag{2.1.20}$$

As H_{rf} increases further, R_s is proportional to $H_{rf}^{1/2}$ and X_s is nearly equal to R_s. It will be shown in section 5.1 of this dissertation that the surface rf fields of the loop-gap resonantor become extremely large at the upper and lower edges of

the electrodes and the high field expression for the impedance is appropriate for describing the measured results.

Also from equation (2.1.15), the dependence of R_s on the frequency ω is found to be linear and not proportional to ω^2 as with losses that are not dominated by grain boundaries. The trend of best polycrystalline R_s data plotted as a function of frequency indicates that at $77K$, $R_s \propto \omega$ and at $4.2K$, $R_s \propto \omega^2$. This is shown in figure 2.1.1.

From equations (2.1.16), (2.1.17), (2.1.18) and (2.1.19), the response of the superconductors surface resistance to microwave surface fields can be interpreted in terms of this extended two fluid model. Usually, for the polycrystalline YBCO, R_s exhibits a critical state behavior where the surface resistance as a function of the surface fields remains constant up to a critical value. As the rf surface fields are increased past this value, R_s increases sharply [64]. This sharp increase is qualitatively represented in equation (2.1.16) where $R_s \propto H_{rf}$. Further increases in the magnetic microwave fields brings the YBCO into a saturated state where R_s is somewhat less dependent on H_{rf} [33]. At these high fields, $R_s \propto H_{rf}^{1/2}$.

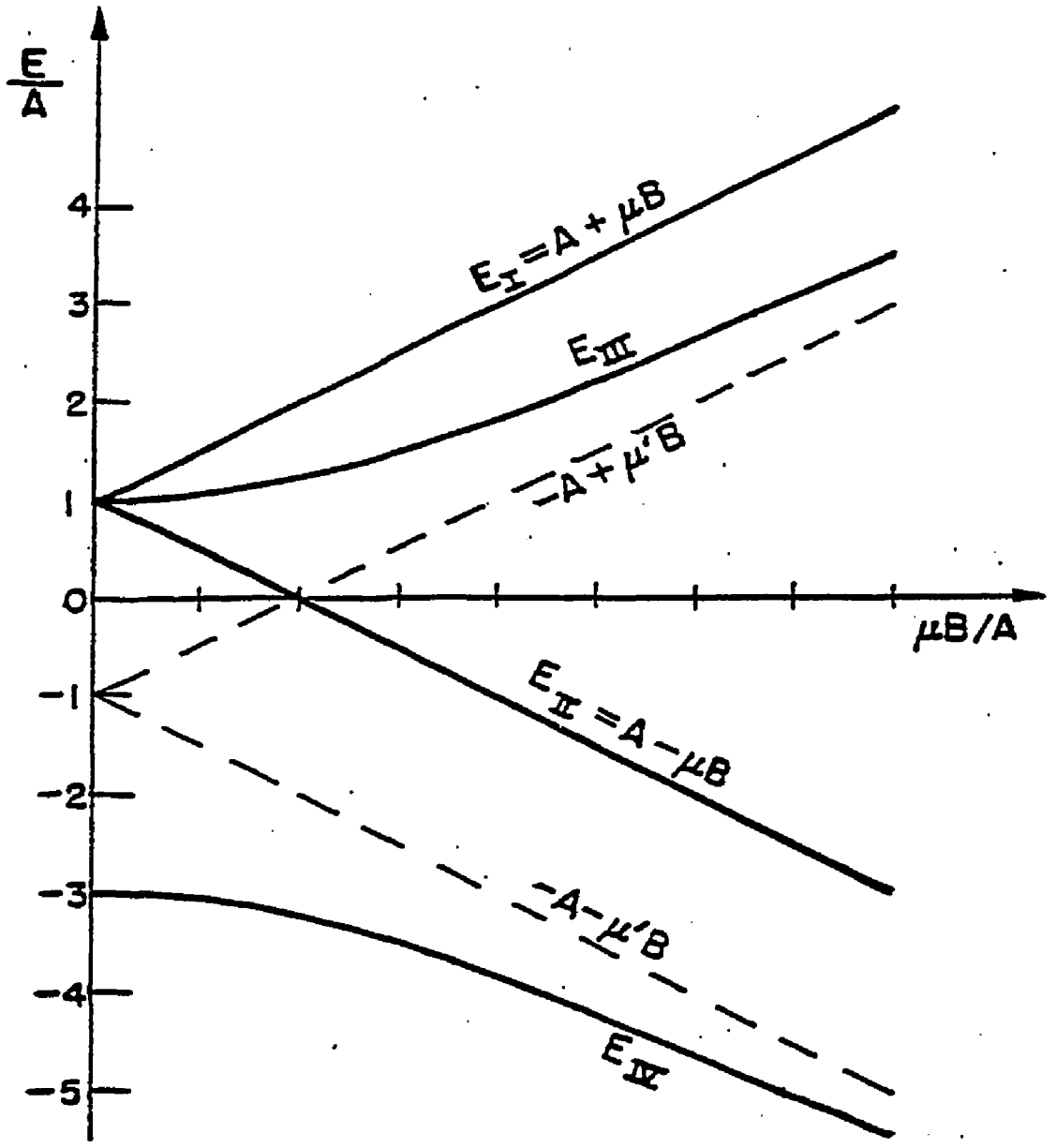

Figure 2.2.1 The energy levels of the ground state hydrogen atom in an external magnetic field B. If B is small, then the energy level E_{III} corresponds to the $| F = 1, m = 0 \rangle$ state and E_{IV} corresponds to the $| F = 0, m = 0 \rangle$ state.

(2.2) Description of Maser Operation

A hydrogen maser frequency standard is based on the stimulated hyperfine magnetic dipole transition from the $|F = 1, m_f = 0\rangle$ triplet state to the $|F = 0, m_f = 0\rangle$ singlet state, corresponding to a frequency of $1,420,405,751.769 \pm 0.002 Hz$. For the configuration where the rf magnetic field is parallel to the applied dc magnetic field direction, the transition where $\Delta F = 1$ and $\Delta m_f = 0$ is the only allowed transition and all others are forbidden, according to the selection rules.

Figure 2.2.1 shows the energy levels of the hyperfine Zeeman states as a function of magnetic field. The notations used in this diagram are from reference [65], where the energy levels of the hydrogen hyperfine states are derived. In figure 2.2.1, E_I and E_{II} are the $|F = 1, m_f = 1\rangle$ and $|F = 1, m_f = -1\rangle$ triplet states, respectively. When the these two triplet states can be ignored (because of the selection rules), the system is simplified to a transition between two energy levels, with values E_1 and E_2, with $E_2 > E_1$. For hydrogen, the upper energy level corresponds to the remaining triplet state and E_1 represents the singlet state. Now consider a large number of atoms, where the number of particles with the energies E_1 and E_2 is n_1 and n_2, respectively. At thermal equilibrium, the number of particles in the higher energy state is

$$n_2 = n_1 \exp \frac{-(E_2 - E_1)}{kT} \,. \tag{2.2.1}$$

In the presence of electromagnetic radiation with the frequency ν given by

$$\nu = \frac{(E_2 - E_1)}{h} \,, \tag{2.2.2}$$

the power absorbed by the system of atoms is given in terms of the transition

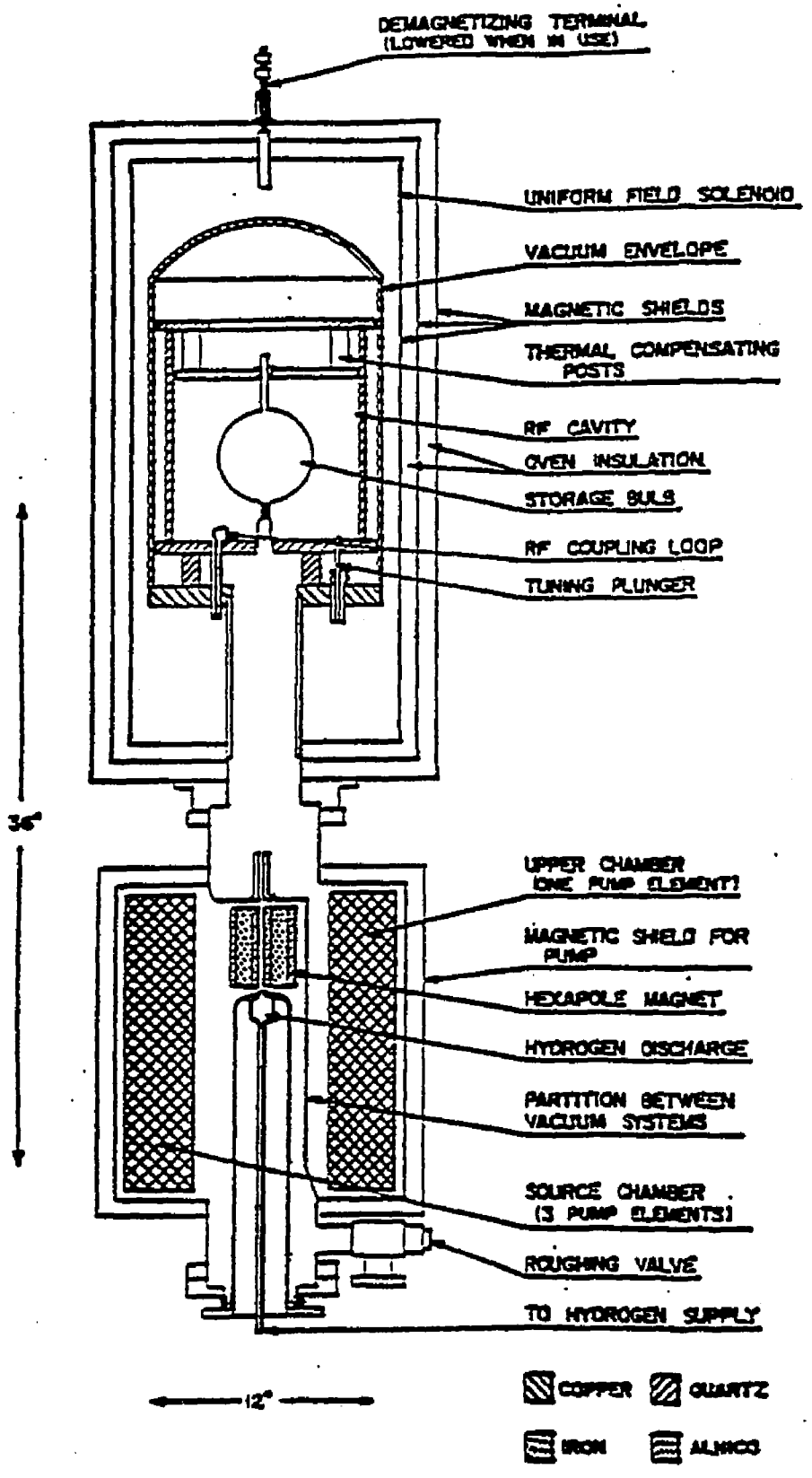

Figure 2.2.2 Hydrogen maser with a TE_{011} cylindrical cavity resonator [15].

probability as

$$P_A = W_{12} n_1 h\nu \ . \tag{2.2.3}$$

The transition probability W_{12} describes transitions from state 1 to 2 by the induced absorbtion of a photon from the radiation field. The power emitted by the atoms due to stimulated emission of the atoms is given by

$$P_E = W_{21} n_2 h\nu \ . \tag{2.2.4}$$

If spontaneous transitions are neglected so that $W_{12} = W_{21}$, then the net power emitted from the atoms will be

$$P_E - P_A = P = W_{12}(n_2 - n_1)h\nu \ . \tag{2.2.5}$$

Equation (2.2.5) shows that the atoms will emit radiation with the frequency ν if $n_2 > n_1$. The thermal equilibrium populations of the two energy states is given in equation (2.2.1) indicating that for all positive values of temperature $n_1 > n_2$(a population inversion corresponds to a negative temperature, from equation (2.2.1)) [14]. If the population inversion of the states can be maintained, in the presence of stimulating radiation, the atoms will contribute to the total power of frequency ν in the radiation field. To stimulate and measure this transition frequency, the appropriate device must maintain a radiation field at the transition frequency and a population difference between the two energy levels such that $n_2 > n_1$. Such conditions are realized in the device shown schematically in figure 2.2.2 [15].

In this device, the hydrogen maser, an atomic hydrogen beam from an rf dissociator passes through a state selection magnet where the $|F = 1, m_f = 1\rangle$ and

$|F = 1, m_f = 0\rangle$ states are focused into the interaction region of a microwave cavity. The atoms in the other states are directed away from the cavity opening and then pumped away. The atoms selected to be in the upper hyperfine states enter a storage bulb where the atoms remain for about a second. This storage bulb traps the atoms in the interaction region of a microwave cavity whose oscillating magnetic field has the correct orientation and frequency to stimulate the desired hyperfine transition. When the number of atoms in the atomic beam is increased beyond a critical value, then a high level of microwave energy can be maintained in the cavity from the stimulated emission alone. Under certain conditions, there is enough microwave energy liberated from the atomic beam so that the maser can oscillate. This self oscillation occurs when the power emitted from the beam compensates for the power lost to the cavity walls and through the microwave coupling ports [13].

The microwave cavity is tuned to the transition frequency and has the correct rf and dc field orientations to coherently stimulate the atoms in the storage bulb. The hydrogen transition frequency is dependent on the static magnetic field and therefore, magnetic shields surround the cavity. A small dc magnetic field is applied to remove the degeneracy with transitions from the other states and thus establishes an axis of quantization. Usually, the TE_{011} mode of a cylindrical resonant cavity is used to couple to the hydrogen transition and the dc field is applied parallel to the longitudinal cavity axis. Such a cavity measures nearly $28cm$ in length and diameter. This mode is a high Q mode with a cavity quality factor Q_c of about 60000 for copper surfaces at room temperature.

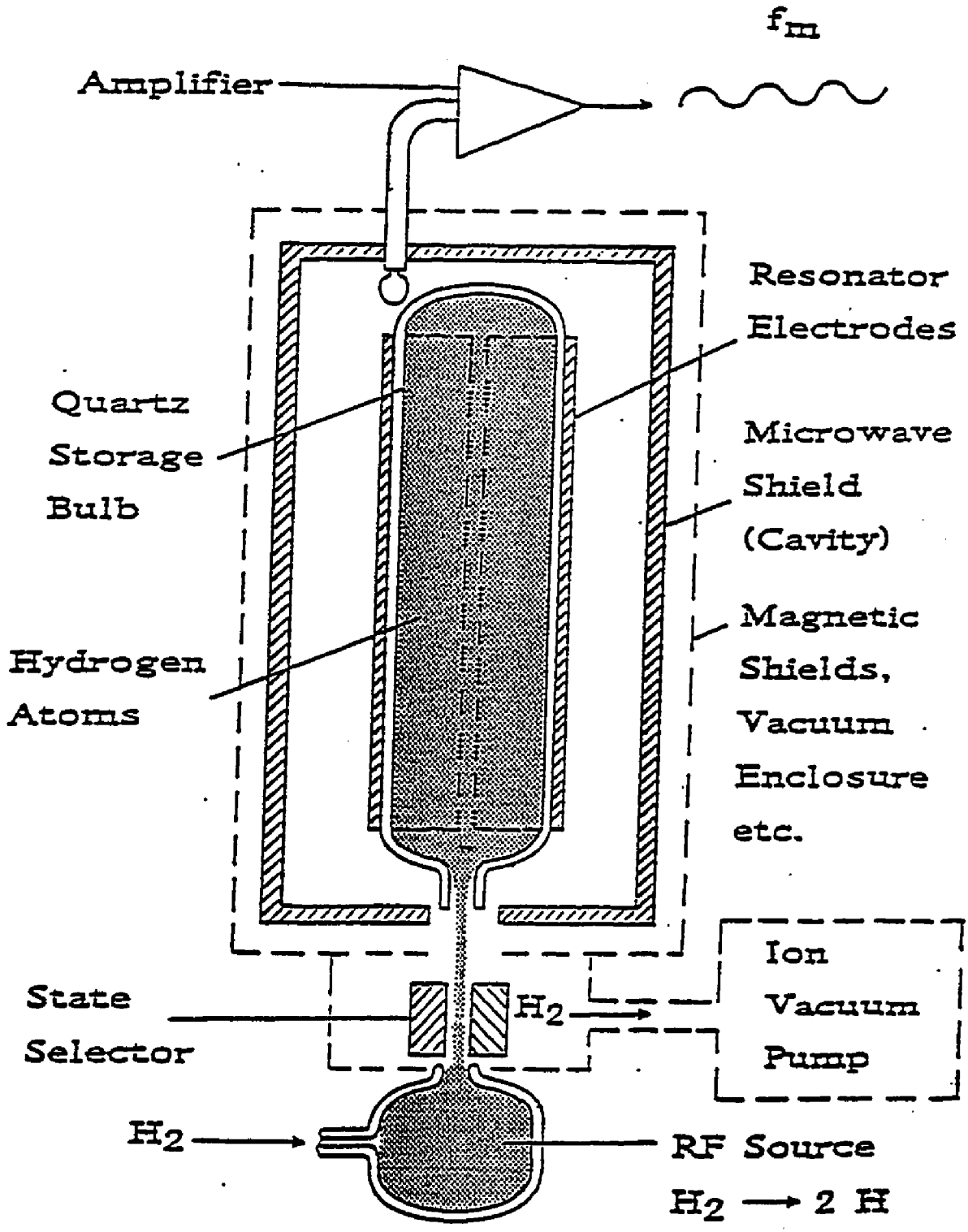

Figure 2.2.3 Compact hydrogen maser with a split-ring type loop-gap resonator [3].

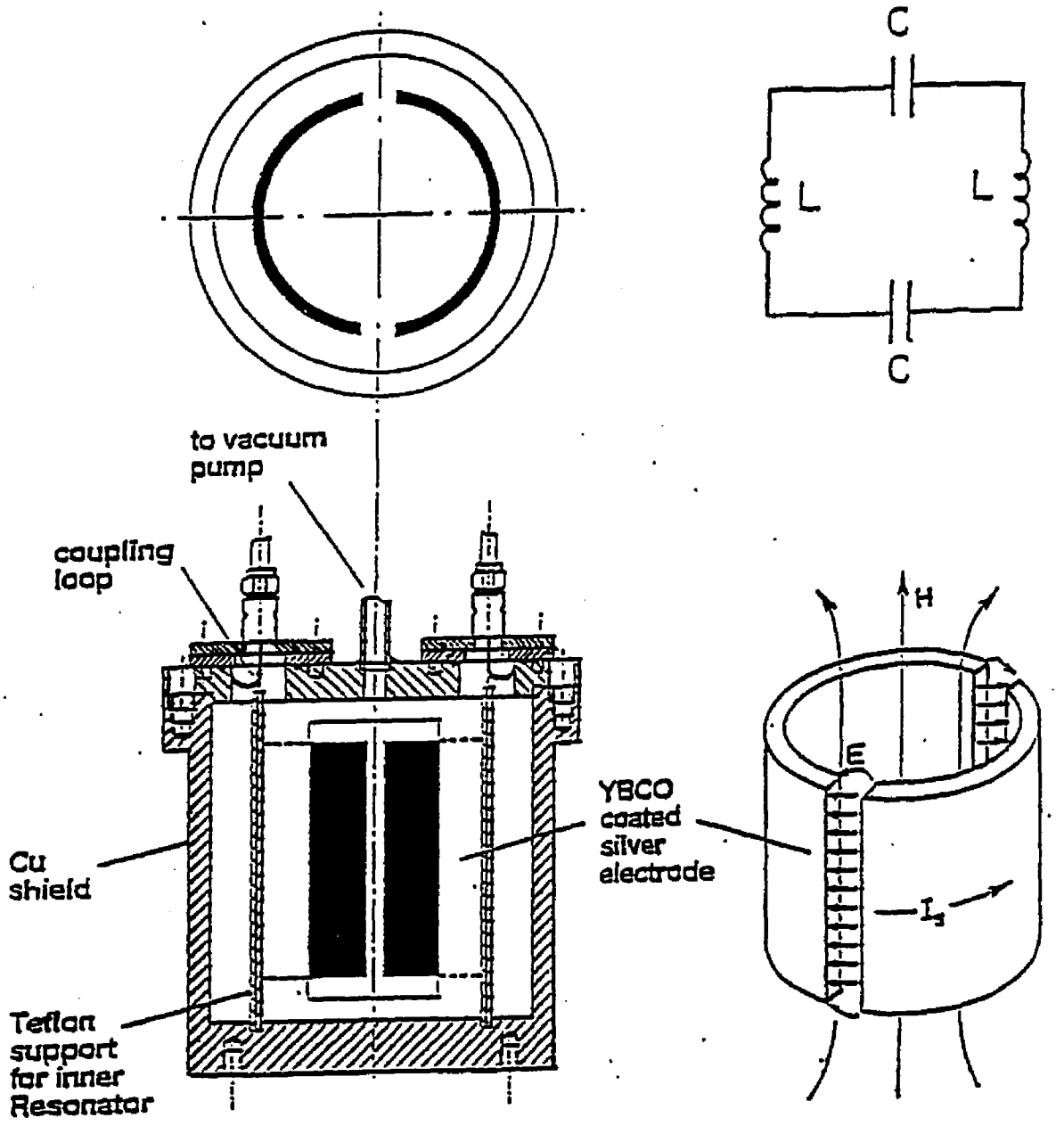

Figure 2.2.4 Schematic of a compact loop-gap maser resonator with the field configuration near the inner electrodes and the equivalent circuit.

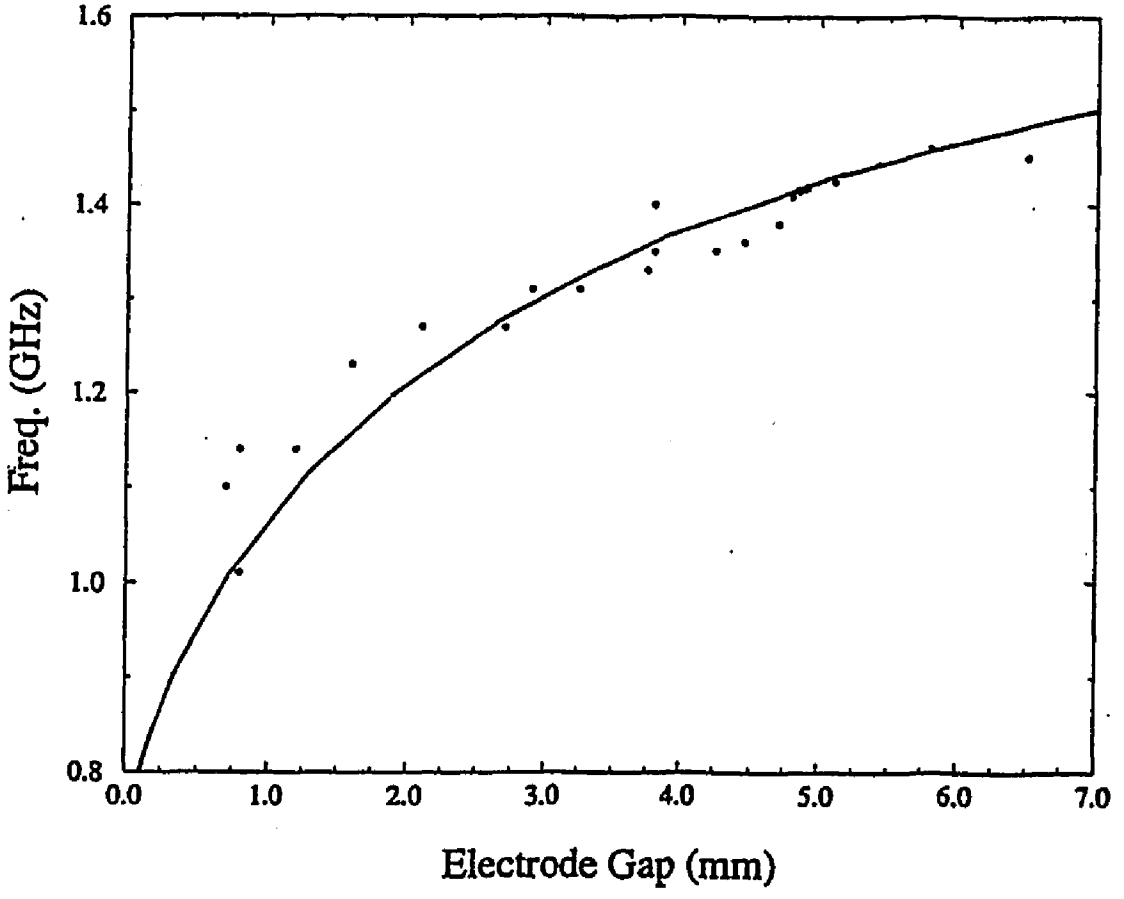

Figure 2.2.5 Graph of the measured loop-gap resonator frequency as a function of the separation distance between the electrode halves.

Compact Hydrogen Maser

As mentioned above, for some applications a smaller maser resonator may offer significant economic gain to warrant the development of a compact version of the hydrogen maser frequency standard. A magnetron type lumped element resonator has been proposed as a viable, compact alternative to replace the standard TE_{011} cylindrical cavity [3]. This suggested cavity design is shown in figure 2.2.3 [3]. The loop-gap resonator is not constrained by the rf boundary conditions to be as large as the TE_{011} cavity because the resonance is of a completely different nature. The loop-gap is a inductance-capacitance resonant circuit. The currents that flow azimuthally on the surface of the electrodes shown in figure 2.2.4 create a magnetic field that is qualitatively solenoidal and forms the inductive part of the circuit. The gaps between the electrode halves are the capacitive elements of the LC circuit. This circuit is shown schematically in the same diagram. The loop-gap can be made in different sizes; the cavity described here has a diameter and height of $7.5cm$, and the electrodes that form the resonant structure have a diameter and height of $5.0cm$.

The frequency of the loop-gap resonator is given by

$$\omega_c = \frac{1}{\sqrt{LC}} \,. \tag{2.2.6}$$

Here L is the inductance of the circuit and C is the capacitance. The inductance of the loop-gap resonator will depend on the size of the electrodes, the size of the shield-can and the distribution of the currents on the electrodes [3]. The current distribution will be addressed later, in detail. The relevant capacitance is that formed by the gaps between the electrode halves. The frequency of the resonator

is most easily adjusted by varying the gap size. When the gap is widened, the capacitance is reduced and from equation (2.2.5), the frequency increases. The possible tuning range for the maser resonator was found to be from $700MHz$ to $1.6GHz$. Figure 2.2.5 shows the measured frequency for different gap widths. The data points in figure 2.2.5 were measured between 1988 and 1991 with copper, silver, steel, and YBCO electrodes and were held by teflon and PVC interlocking cylinders. Even with such a variety of measurement conditions, the scatter of the points is quite small. The solid curve shows the behavior expected when the capacitance is evaluated for the geometry of the electrode gaps. The solid line in figure 2.2.5 is the calculated frequency as a function of the gap size where the capacitance is found using a Schwarz-Christoffel transformation. As the gap becomes small, the resonant frequency becomes quite sensitive to changes in the gap size.

The loop-gap resonator mode is not a high Q_c mode. A copper version of the loop-gap cavity at room temperature has a quality factor of about 5000 (the quality factor is the ratio of the stored energy to the power lost per cycle). The Q_c of the loop-gap is ten times lower than that of the TE_{011} cavity and the hydrogen atoms cannot deliver enough power to the cavity to make it oscillate. If the cavity power losses are equated to the power delivered from the atomic beam, then by equation (2.2.5), the number of atoms radiating should be increased to bring the system back into oscillation. This is an over simplification, as will be shown later. The relationship for the power delivered to the cavity as a function of the number of atoms reaches a maximum and then decreases as the number of atoms is further

increased. This is due to line broadening from collision related relaxation processes such as spin exchange, which will be described later.

Since the compact resonator has a lower Q_c and the maser made with this cavity cannot be made to oscillate by increasing the number of hydrogen atoms in the upper hyperfine state, then a method must be found to store the resonant energy radiated by the atoms more efficiently. Increasing the Q_c of the compact resonator by using a superconducting version of the loop-gap resonator is the proposed solution. However, oscillation is not the only criteria for developing a high quality frequency standard; the stability of the oscillator must also be considered during the oscillator design phase.

2.3 Introduction to Stability

In designing a precision oscillator, the stability must be addressed because the geometry can have a significant influence on the fundamental stability limitations of the oscillator [16]. In general, the signal that is measured from a stable oscillator is a function of the signal amplitude A, angular frequency ω and is a sinusoidal function given by,

$$V(t) = Asin\omega t \; . \tag{2.3.1}$$

With the amplitude and the phase fluctuations written explicitly the general form of the measured signal is,

$$V(t) = A(1 + \epsilon(t))sin(\omega t + \phi(t)) \; . \tag{2.3.2}$$

In the above equation, $\epsilon(t)$ and $\phi(t)$ describe the time-dependent fractional amplitude fluctuations and the time-dependent phase changes, respectively. Given a signal that may be characterized by the above equation, the standard developement of the stability leads to a method by which parameters characterizing the amplitude and phase fluctuations can be quantitatively measured [17].

Any stability measurement is a comparison between the oscillator under test and a reference oscillator. To minimize complications, the reference is assumed to be significantly more stable than the test oscillator. To describe the measured difference between the oscillator frequencies, the following standard definitions are made:

$$y(t) = \frac{\nu - \nu_o}{\nu_o} = \frac{1}{2\pi\nu_o}\frac{d\phi(t)}{dt} = \frac{dx}{dt} \; , \tag{2.3.3}$$

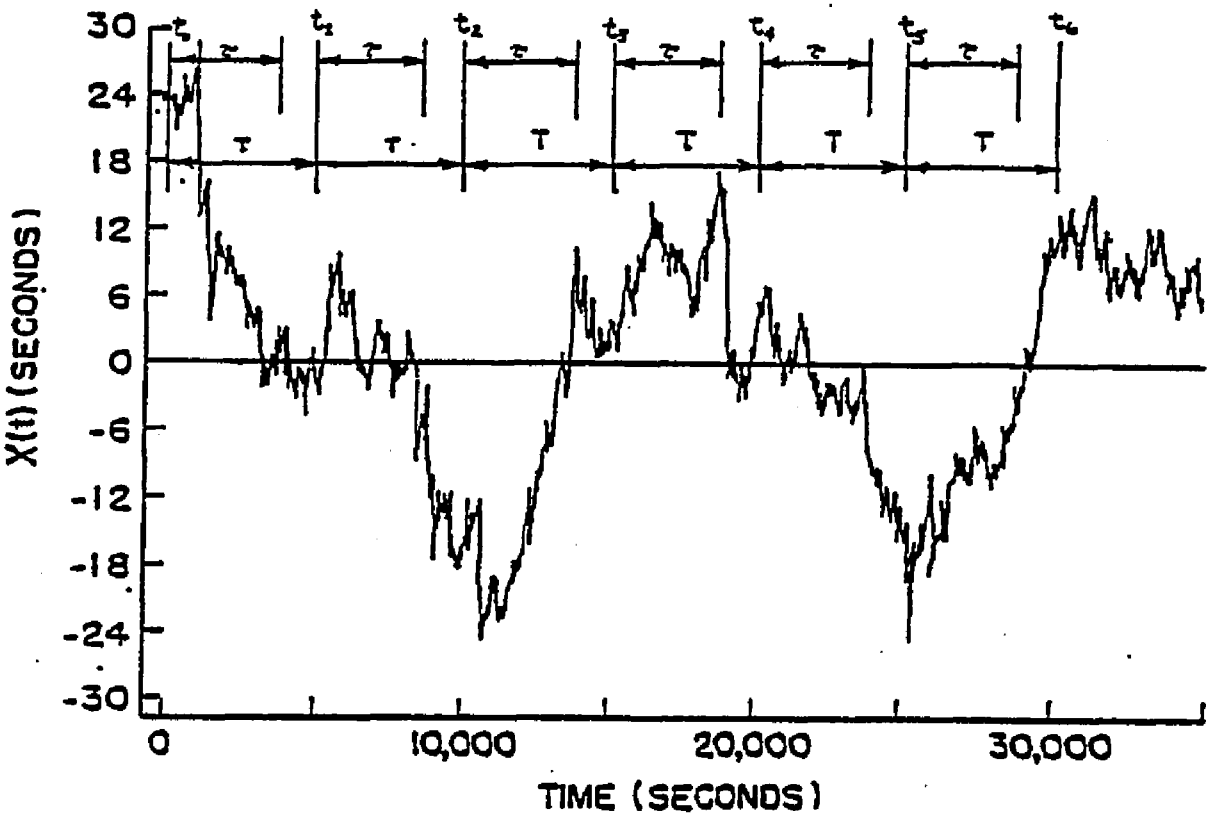

Figure 2.3.1 Measured time difference $x(t)$ between two oscillators plotted as a function of time. τ is the integration time and T is the time interval between measurements. The difference $T - \tau$ is the 'dead-time' where the measured time difference does not contribute to the variance.

where the frequency of the signal to be measured is $\nu = \omega/2\pi$, and ν_o is the reference oscillator frequency. The dimensionless quantity $y(t)$ can be used to find the time deviation, $x(t)$, of an oscillator over a time t, from the formula,

$$x(t) = \int_0^t y(t')dt' = \frac{\phi(t)}{2\pi\nu_o} \ . \tag{2.3.4}$$

Likewise, for the time interval t_k to $(t_k + \tau)$, the average fractional frequency deviation is given by

$$\bar{y}_k = \frac{1}{\tau}\int_{t_k}^{t_k+\tau} y(t)dt \ . \tag{2.3.5}$$

Substituting the results from the previous equation into equation (2.3.4) yields,

$$\bar{y}_k = \frac{x(t_k+\tau) - x(t_k)}{\tau} = \frac{1}{2\pi\nu_o}\frac{\phi(t_k+\tau) - \phi(t_k)}{\tau} \ . \tag{2.3.6}$$

From the measurements of $\bar{y}_k$, where k goes from 1 to N, the variance of N samples is found to be,

$$\langle\sigma_y^2(N,T,\tau)\rangle = \langle\frac{1}{N-1}\sum_{n=1}^{N}\left(\bar{y}_n - \frac{1}{N}\sum_{k=1}^{N}\bar{y}_k\right)^2\rangle \ . \tag{2.3.7}$$

The brackets indicate infinite integration time. The square root of the expectation value gives the deviation.

To illustrate what is being measured, assume that the graph in figure 2.3.1 is a plot of the phase difference, $x(t)$, between the two oscillators as a function of time. The interval time between measurements is T, and the time over which the fractional frequency deviation is integrated is τ. The difference between these two times is the so-called 'dead time', given by $T - \tau$. Frequency differences during the dead time contribute no information to the variance.

There are two problems with the general description of the N-sample variance given above. The first is the loss of information during the dead time, and second is the fact that as $N \rightarrow \infty$, the N-sample does not always converge. This second problem would result in a divergence of the variance that is a manifestation of the statistics and not from the measured frequency stability. For these reasons, the 2-sample variance (Allan variance) is preferred. This variance converges for all major types of noise in precision oscillators [18]. The Allan variance is written as,

$$\sigma_y^2(\tau) = \langle \frac{1}{2}(\bar{y}_{k-1} - \bar{y}_k)^2 \rangle \ . \tag{2.3.8}$$

For N discrete time measurements, where $N < \infty$, the variance is approximately given by,

$$\sigma_y^2(\tau) \approx \frac{1}{2(N-2)} \sum_{i=1}^{N-2} (y_{i+1} - y_i)^2 \ , \tag{2.3.9}$$

or by using the phase difference information of equation (2.3.6), this can be written as,

$$\sigma_y^2(\tau) \approx \frac{1}{2(N-2)\tau^2} \sum_{i=1}^{N-2} (x_{i+2} - 2x_{i+1} + x_i)^2 \ . \tag{2.3.10}$$

The frequency domain spectral density of phase fluctuations can also be calculated from the measurement described above [18]. These spectral densities are defined as,

$$S_y(f) = \left(\frac{f}{\nu_o}\right)^2 S_\phi(f) = 2\pi f^2 S_x(f) \ , \tag{2.3.11}$$

where $S_y(f)$ is the spectral density of frequency fluctuatuations, $S_\phi(f)$ is the spectral density of phase fluctuations and $S_x(f)$ is the time deviation spectral density. Strictly speaking, the time and frequency domain measurements of the fluctuations

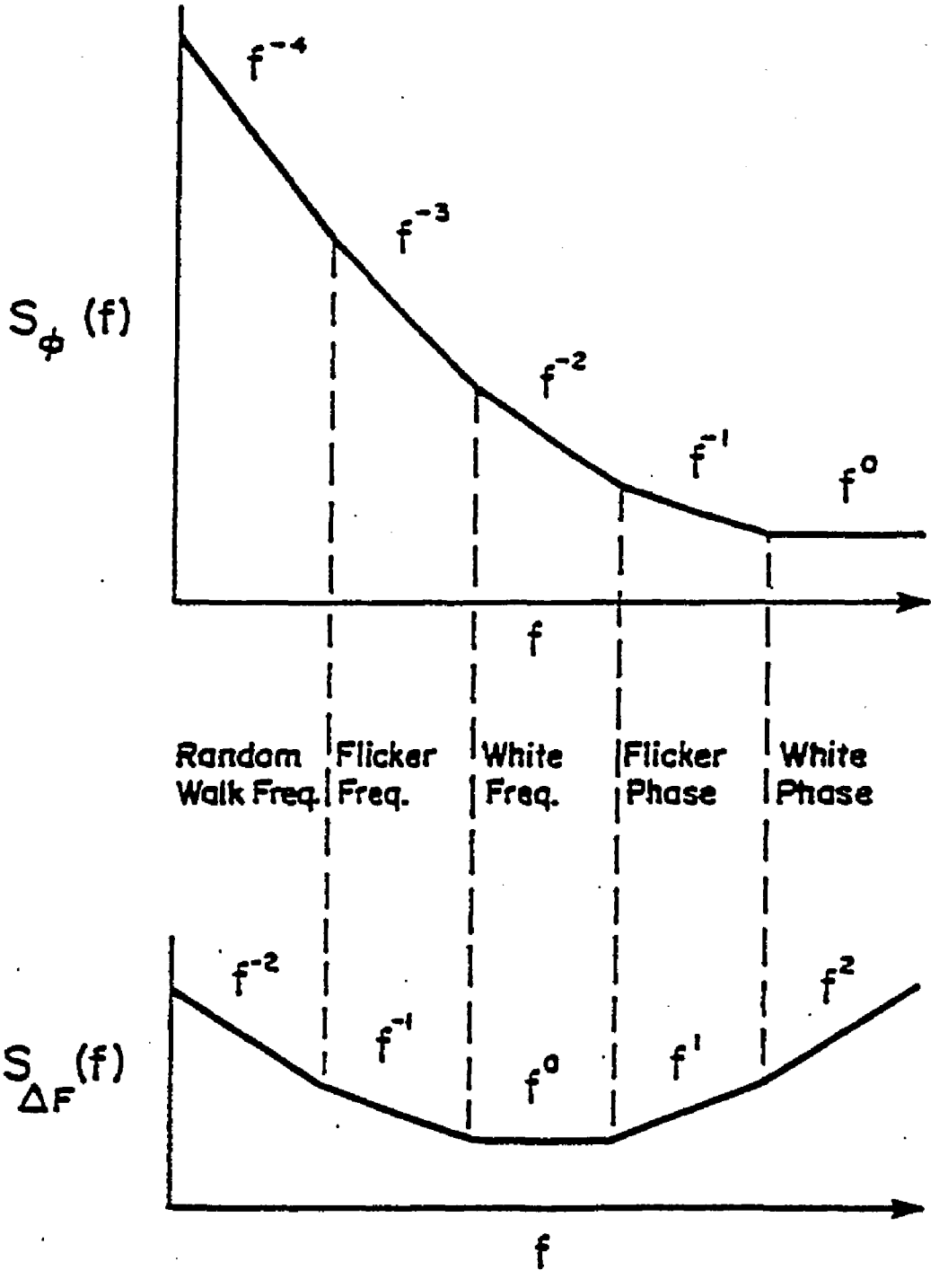

Figure 2.3.2 Log-log plot of $S_{\Delta f}(f)$ and $S_\phi(f)$ as a function of frequency, representing the power-law model of frequency fluctuations.

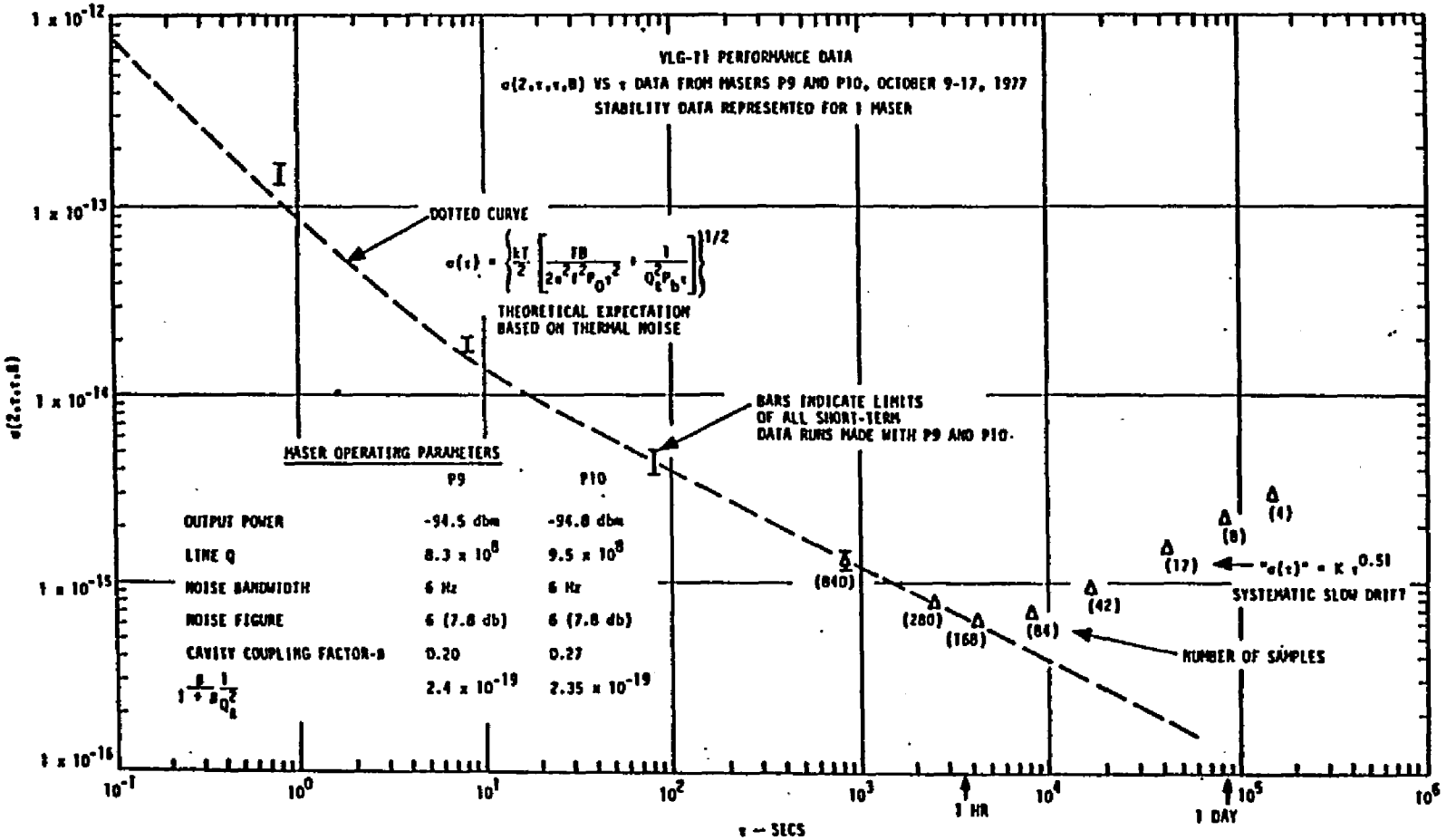

Figure 2.3.3 Measured Allan deviation for the VLG-11 masers at the Smithsonisn Astronomical Observatory. The deviation clearly demonstrates the validity of the power-law representation of frequency fluctuations.

Table 2.3.1

Relationships Between Power Spectral Densities and Allan Variance

	$S_{\Delta F}(f)$	$S_\phi(f)$	$\sigma_y^2(\tau)$
White Phase	$K_0 f^2$	K_0	$\frac{3 K_0 F_H}{4\pi^2 F_O^2 \tau^2}$
Flicker Phase	$K_1 f$	$\frac{K_1}{f}$	$\frac{K_1}{4\pi^2 F_O^2 \tau^2}\left(3.81 + 3 \ln (2\pi F_H \tau)\right)$
White Frequency	K_2	$\frac{K_2}{f^2}$	$\frac{K_2}{2 F_O^2 \tau}$
Flicker Frequency	$\frac{K_3}{f}$	$\frac{K_3}{f^3}$	$2 \ln (2) \frac{K_3}{F_O^2}$
Random Walk Frequency	$\frac{K_4}{f^2}$	$\frac{K_4}{f^4}$	$\frac{(2\pi)^2 K_4 \tau}{6 F_O^2}$

Ref. "Characterization of Frequency Stability," J.A. Barnes, et al., IEEE Transactions on Inst. and Meas., Vol. IM-20, no. 2, pp.105, 1971

are related by a Fourier transformation. However, as mentioned in reference [18], the Fourier transformation is seldom used to convert between the two descriptions of the same noise process. Instead, many techniques have been developed to translate between the various measures of stability. The power-law model is the most common method that describes both time and frequency domain spectral densities. In this model simple relationships are given that transform from one noise description to another.

In the power-law model, it is assumed that the spectral density of frequency fluctuations may be written as a sum of terms, each of which are proportional to an integer power of the frequency. For example, $S_y(f)$ may be written as,

$$S_y(f) = \sum_{\alpha=-\infty}^{\infty} K_\alpha f^\alpha \ . \tag{2.3.12}$$

With this equation the spectral density of frequency fluctuations is expressed as a function of a constant K_α, and an exponent α. On a log-log plot of $S_y(f)$ versus f, each term is shown as a straight line of slope α over a given range of f. Figure 2.3.2 shows a plot of the $S_y(f)$ and $S_\phi(f)$ for $-2 \leq \alpha \leq 2$. Table 2.3.1 lists each of the terms shown in figure 2.3.2 and the noise process that they represent.

Using the relationships from table 2.3.1, the time domain Allan deviation can be plotted as a function of the integration time, τ from the measured $S_y(f)$ or $S_\phi(f)$ curves. Shown in figure 2.3.3 is the power-law time domain spectrum of the Allan deviation and, for comparison, data measured from an active maser oscillator [19]. The data in figure 2.3.3 has been interpreted using the power-law model, where each term of the deviation corresponds to a specific physical noise process, represented by

a specific slope on the graph. For the data shown in figure 2.3.3, the fluctuations of a maser oscillator are typically dominated by the fundamental terms of the power-law spectrum where the time domain fluctuations are those proportional to τ^n, where $n = -1, -1/2, 1/2$.

The dominant noise source for each of the terms given in table 2.3.1 falls into one of two categories; random or systematic fluctuations. Random processes are fundamental uncorrelated fluctuations of the frequency. Systematic fluctuations are fluctuations in the frequency of a stable oscillator caused by: (1) environmental variables; including ambient temperature, magnetic field, humidity, barometric pressure, vibrations, gravity, and time; (2) basic internal mechanisms, including cavity pulling, internal magnetic fields and field gradients, wall shifts, collisional frequency shifts, and second order Doppler shifts; and (3) internal structures and systems that transduce environmental changes into basic mechanisms [20].

It has been possible to determine empirical relations in terms of the power-law model for measured time domain spectra [21]. For example, consider the data shown in figure 2.3.3; this curve can be described by three terms, when the Allan variance is given as

$$\sigma^2(\tau) = \sigma_e^2(\tau) + \sigma_l^2(\tau) + \sigma_p^2(\tau)\ , \tag{2.3.13}$$

with

$$\sigma_e^2(\tau) = \left[\frac{FkTB}{4\pi^2\nu^2\tau^2}\right]\left(\frac{1+\beta}{\beta}\right)\frac{1}{P} \tag{2.3.14}$$

$$\sigma_l^2(\tau) = \left[\frac{kT}{2\tau}\right]\frac{1}{PQ_l^2} \tag{2.3.15}$$

$$\sigma_p^2(\tau) = (1.5 \times 10^{-13}\frac{Q_c}{Q_l})^{1/2}\ \tau\ . \tag{2.3.16}$$

Here F is the noise figure of the maser's receiver system, B is the bandwidth of the receiver, β is the coupling factor of the cavity, P is the power delivered to the cavity by the hydrogen atoms, and τ is the time over which $\sigma(\tau)$ is measured.

For the Allan deviation proportional to τ^{-1}, the dominant source of the fluctuations are found to be associated with the electronics that process the maser signal. In the region where $\sigma(\tau)$ is proportional to $\tau^{-1/2}$, thermal fluctuations are the dominant noise source. Where the Allan deviation is proportional to τ, environmental fluctuations of the oscillator system (cavity pulling, ...) are responsible. Some oscillators are found to have a deviation 'flicker floor' corresponding to a constant σ; to date, this process is not identified [21]. Assuming perfect isolation from systematic influences, an oscillator is expected to have a frequency stability limited only by random fluctuations. As mentioned above, a maser is found to be limited by random thermal fluctuations for integration times between 10 and 10000 seconds.

The evaluations of proposed maser oscillators in the past have been based on the fact that the limiting frequency stability is due to thermal fluctuations within the hyperfine line width [21,22]. Before a maser is constructed the noise contributions from systematic effects or from particular microwave components are not predictable. For the compact superconducting hydrogen maser, if it is assumed that the systematic effects can be controlled to the same level of isolation typically found in full size masers, then the fundamental thermal fluctuations will limit the stability. Since the thermal fluctuations can be calculated as a function of the maser parameters, this term should be minimized, where possible, during the design phase

of the maser development.

As an application of the electrophoretic technique, a superconducting loop-gap resonator can be made to replace the TE_{011} mode maser resonator. The improvement in the quality factor gained by using the superconducting design may allow maser oscillation at $77K$. The Allan deviation is used in section 5 to find the cavity design that provides the most stable oscillator.

CHAPTER 3

3.1 The Loop-gap Resonator Construction

The constructed loop-gap resonator consists of two parts: the loop-gap electrodes and the rf shield-can, shown in figure 2.2.4. The electrodes have a diameter and height of $5.0cm$ and are $0.5mm$ thick. The rf shield-can has an inner diameter and height of $7.5cm$. The electrodes, which are the resonant structure, are supported concentrically inside the shield-can by two interlocking teflon cylinders. Since the electric field is concentrated in the gaps between the electrode halves, windows are cut in the teflon support cylinders to minimize dielectric losses. The teflon is made $2mm$ longer than the inner length of the shield-can and grooves are cut in the shield-can end plates to accomodate this extra length. This centers the teflon holders in the cavity and keeps the electrodes from moving.

The shield-can is made from OFHC copper and serves as a radiation shield that can also be evacuated. There are two cryogenic coaxial feedthroughs for microwave coupling. The top of the cavity is flanged and is sealed with an indium o-ring. The walls of the shield-can are $0.3cm$ thick. This construction provides a sturdy vacuum can that remains sealed to temperature as low as $4.2K$.

The superconducting version of the loop-gap resonator has electrodes that are fabricated from silver that is electrophoretically covered with an YBCO thick film. Only the electrodes are made superconducting in the first version of this maser

resonator because, in an all copper resonator, nearly 75% of the power losses occur on the electrode surfaces.

Electrophoresis

We have used an electrophoretic deposition process in the formation of polycrystalline YBCO thick films on silver substrates. Electrophoresis is the migration of charged particles under the influence of an applied electrostatic field [23]. Most material that come into contact with a polar (e.g. aqueous) medium will develop a surface charge and likewise, under such circumstances, grains of YBCO powder also develop a surface charge when introduced into this type of liquid [64]. Applying a potential between two electrodes placed in the YBCO liquid solution drives the powder grains toward the oppositely charged electrode; in our case, the cathode. When the desired metallic substrate is used as the cathode, the deposition of the grains onto the substrate produces a uniform $10 - 20\mu m$ thick film coating of the superconducting grains. Substrates of different materials have been investigated to find which would provide the best superconducting films and have suitable mechanical properties for cavity construction. During annealing(sintering), the grains grow together to form intergranular contacts. As is demonstrated with the hydrogen maser resonator, this method offers greater flexibility in choice of substrate shape and sizes compared to thin film deposition onto single crystal substrates.

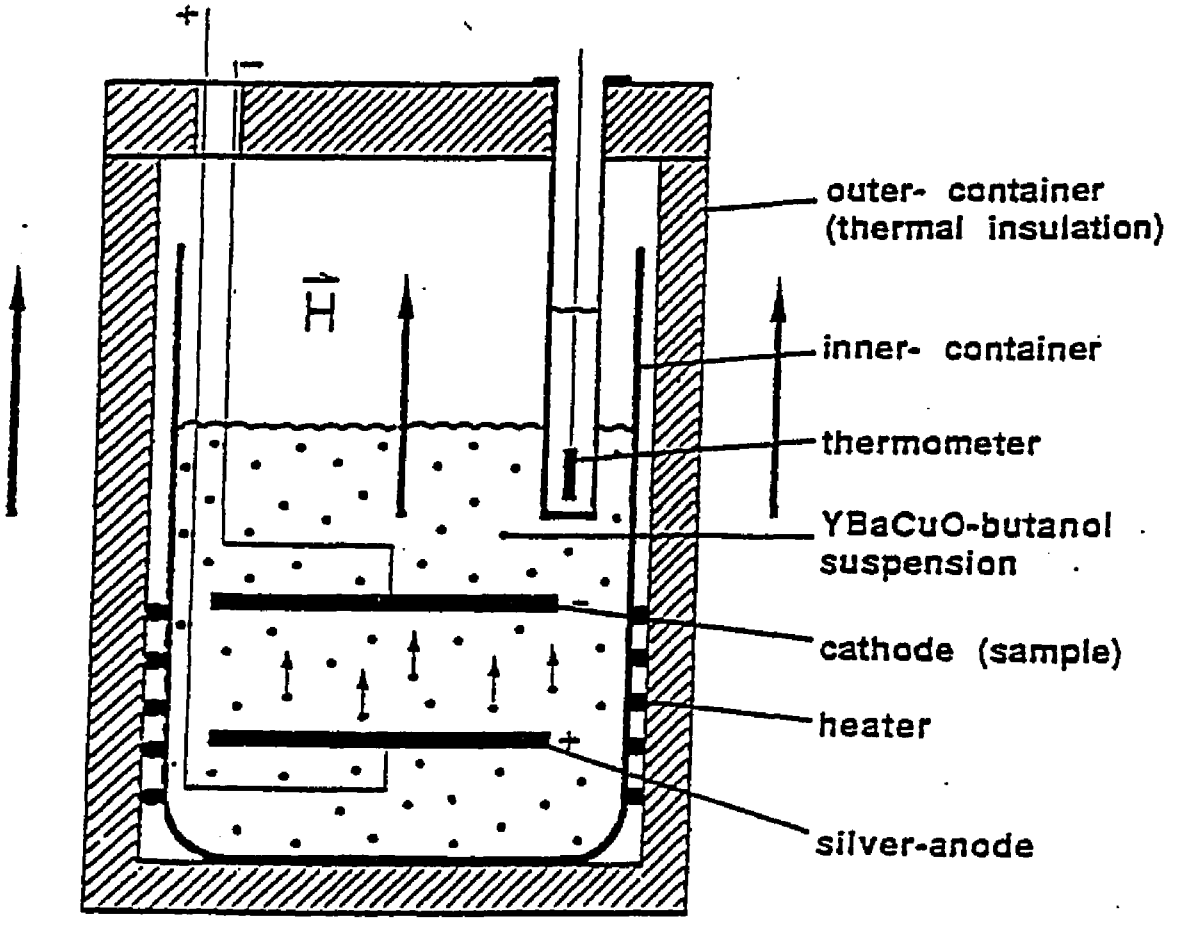

Figure 3.1.1 Diagram of a electrophoretic deposition set-up for the fabrication of textured thick films of the YBCO material.

Table 3.1.1

Electrophoresis for the Maser cavity

Purity of Acetone	99.9%
Temperature	20 C
Powder Concentration	2 g/l
Voltage	150 V
Electrode Distance	8 -10 mm
Water Content	< 0.2%
Current Density	5 -50 μ A/cm^2
Deposition Rate	1 - 5 μ m/min.

Deposition

The electrophoretic process uses stoichiometric 1:2:3 YBCO powder prepared by typical reaction methods [24]. A mixture of $BaCO_3$, Y_2O_3 and CuO powders is calcined in air for 24 hours at temperatures between 800 and 860°C and then reacted for 50 hours at 915°C in air. The resulting ceramic is ground, ball milled and then resintered for an additional 50 hours. This regrinding and second sintering step improves the homogeneity of the reacted powder. The completely sintered material is thoroughly wet milled in n-hexane to a fine powder and then dried before preparing the electrophoretic suspension [25].

The medium for the electrophoretic deposition is a colloidal suspension of the YBCO powder and an organic polar liquid. Butanol, pure acetone or acetone with a very small amount of iodine or ammonium added, have all been successfully used as the deposition solution [26]. However, due to the reaction of alcohols with YBCO, and the uncertain effects the acetone additives might have, pure acetone seems to be the best choice [24]. The YBCO powder is dispersed in the liquid (acetone) using ultra-sonic agitation followed by a sedimentation period. The dispersion of the powder by placing the solution container in the ultrasonic bath separates the agglomerates of particles. The sedimentation allows any non-colloidal particles to separate themselves from the working liquid. The anode and substrate are immersed in this solution and a 150V potential is applied between these two electrodes. Figure 3.1.1 diagrams the electrophoretic deposition process. Achieving reliable deposition depends on the suspension temperature, powder concentration, electric field strength,

and the amount of impurities in the liquid. Table 3.1.1 gives a summary of the deposition variables that have given reliable deposition.

The structure used for the deposition of the films was designed to hold the substrate and the anode so that fields between the anode and cathode are as uniform as possible. Since the complete surface of the cathode must be covered, the electrical and mechanical contacts to the substrate should cover a minimal surface area. This was accomplished by placing the anode and cathode in a brass and teflon frame where screws in the frame would pinch the electrodes, contacting them only on the upper and lower edges. The complete mounting structure was then immersed in the YBCO-acetone solution for deposition.

Electrophoretic deposition in a magnetic field has been shown to improve the microwave properties by producing oriented thick films [27]. The normal conducting magnetic anisotropy in the YBCO crystals aligns the crystal c-axis with the direction of the applied field. A field of $7T$ has reliably yielded oriented films on flat substrates with the c-axis perpendicular to the plane of the substrate. Since the magnetic texturing will align the c-axis in one direction, this process is restricted to microwave components (or pieces of components) where all of the microwave currents flow perpendicular to a single direction, along which the magnetic field is applied. For the loop-gap electrodes, the currents flow azimuthally and require that the c-axis be directed along the longitudinal axis of the cylindrical electrodes, parallel to the substrate surface. On flat substrates, the YBCO films remain oriented after long sinter times.

Sintering

Following the deposition onto the substrate the film is sintered in O_2 for at least 100 hours at temperatures between 920 and 930°C. At the end of the sinter cycle, the oven temperature is reduced at a rate of one degree per hour until the sample temperature is below 890°C. This slow cooling step enables recrystallizaton of all the liquid phases. From 890°C to room temperature, the sample is cooled at 50°C per hour.

During the sintering, liquid phases play a critical role. It has been reported that liquid phases at the silver-YBCO interface promote grain growth [28]. What these liquid phases exactly do is still unknown, but the following reactions are known to occur in O_2 at sinter temperatures:

-Silver dissolves significant amounts of oxygen which reduces the melting point of silver from 960°C to 939°C [29].

-Barium reacts with silver to reduce the melting point of the silver [29].

-Ag reacts with and dissociates the $BaCO_3$ and $BaCuO_2$ compounds [29].

-The melting temperature of the $BaCuO_2$ eutectic phase is 925°C, (896°C in air) [30].

The YBCO superconducting phase and the Y_2BaCuO_5 'green phase' are stable and remain solid at temperatures below 939°C and have no reaction with the silver or the barium eutectic phase [29]. Some of the above mentioned reactions occur during the sintering process and increase the average grain size compared to samples with similar sintering steps but without silver [31]. However, since the melting

temperature of YBCO is about $100°C$ above the melting temperature of silver in O_2, sintering of phase pure YBCO at $930°C$ is not expected to yield significant grain growth.

3.2 RF Measurements of the Loop-gap

The microwave measurements of the loop-gap resonator determine the cavity quality factor Q_c and the total power losses in the cavity. Q_c is measured by finding the full width of the resonant line, Δf, at half of the maximum power centered at frequency f. The Q_c is defined as

$$Q_c \equiv \frac{\omega U}{P_c} = \frac{f}{\Delta f} = \frac{G_c}{R_s}. \tag{3.2.1}$$

Here U is the total energy stored in the cavity, P_c is the power lost to the surfaces in the cavity, G_c is the cavity geometry factor and R_s is the surface resistance of the cavity material. The geometry factor of the resonator contains all of the geometric dependencies that can influence the Q_c and is defined as

$$G_c = \frac{\omega \int_{vol.} |\vec{B} \cdot \vec{H}| dv}{\frac{1}{2} \int_{area} |\vec{H}|^2 da}. \tag{3.2.2}$$

The volume integral sums the total energy in the cavity, the area integral gives the sum of the power lost on the surfaces [32]. When the resonator is constructed such that the losses from different materials, which have different R_s values, contribute to the total power lost in the cavity, then equation (3.2.2) must be evaluated for the different surfaces, each with its own geometry factor.

For example, if the loop-gap resonator was measured with a copper shield-can and electrodes made from silver, then the geometry factors are evaluated for each piece, separately

$$\frac{1}{G_c} = \frac{1}{G_{electr.}} + \frac{1}{G_{shield}} = \frac{\int_{electr.} |\vec{H}|^2 da}{2\omega \int_{vol.} |\vec{B} \cdot \vec{H}| dv} + \frac{\int_{shield} |\vec{H}|^2 da}{2\omega \int_{vol.} |\vec{B} \cdot \vec{H}| dv} \tag{3.2.3}$$

and the Q_c is given by

$$\frac{1}{Q_c} = \frac{R_{s,Ag}}{G_{electr.}} + \frac{R_{s,Cu}}{G_{shield}} = \frac{R_{s,Ag}\int_{electr.}|\vec{H}|^2 da}{2\omega\int_{vol.}|\vec{B}\cdot\vec{H}|dv} + \frac{R_{s,Cu}\int_{shield}|\vec{H}|^2 da}{2\omega\int_{vol.}|\vec{B}\cdot\vec{H}|dv} \ . \quad (3.2.4)$$

When the teflon support cylinders are considered, the equation for Q_c must be modified by a term describing the dielectric losses,

$$\frac{1}{Q_c} = \frac{R_{s,Ag}}{G_{electr.}} + \frac{R_{s,Cu}}{G_{shield}} + L\ tan(\delta)\ , \quad (3.2.5)$$

where $tan(\delta)$ is the loss tangent of the teflon and L is the total electric field inside the dielectric, given by [52],

$$L = \frac{\int_{diel.vol.}|E|^2 da}{\int_{vol.}|E|dv} \ .$$

The loss tangent for teflon at $6.5GHz$ and $1.4K$ is $tan(\delta) = 2.4 \times 10^{-6}$. This is the nearest measurement available. At $300K$ and $1GHz$, $tan(\delta) = 1.5 \times 10^{-4}$. The amount of the fringing fields near the gap, that will cause losses in the teflon, depends on the cylinder thickness, height, window size, etc., and therefore, this term is very difficult to determine. Furthermore, since no analytical solution for the loop-gap resonator exists, these electric fields cannot be calculated exactly. To minimize the dielectric losses, the dielectric near the electrode gaps is cut away, leaving windows in the teflon. Considering the temperature dependence of the loss tangent, these losses can be neglected at $4.2K$.

Since the geometry factors cannot be directly calculated, they must be measured. Unfortunately, this measurement must rely on at least one presumtion. Therefore, the surface resistance of copper at room temperature will be calculated and used to algebaically find the remaining geometry factors.

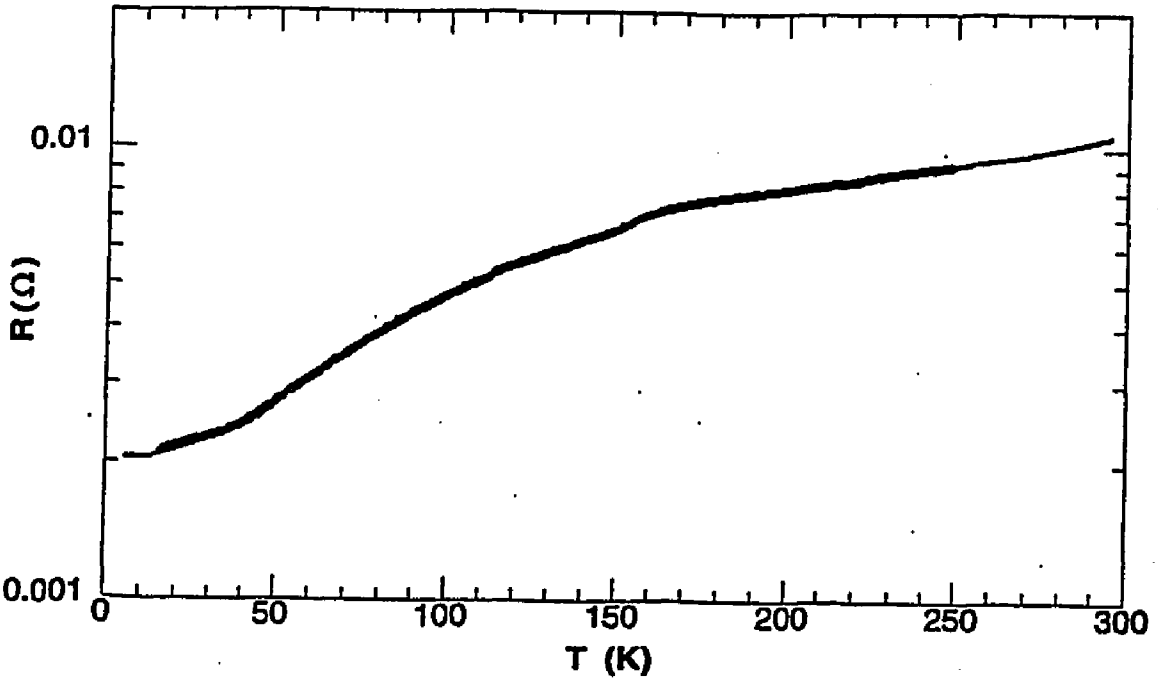

Figure 3.2.1 Surface resistance of copper measured as a function of temperature. The surface resistance was found by using the total geometry factor $G_c = 47\Omega$.

The amount of power lost on the surface of the shield-can is best determined by measuring niobium electrodes at $4.2K$. At liquid helium temperatures and $1.42GHz$, the surface resistance of the niobium is about $1\mu\Omega$, where the R_s of copper at the same temperature and frequency is $2.2m\Omega$. Therefore, the niobium electrodes will contribute less than 1% of the total losses, when it is assumed that 75% of the losses occur on the electrodes in a copper resonator. The Q_c found from this measurement was 89000 with a $11mm$ wide window in the teflon. If it is assumed that $R_s(Nb) \approx 0$ and the dielectric losses are small, then

$$\frac{1}{Q_c} = \frac{R_{s,Nb}}{G_{electr.}} + \frac{R_{s,Cu}}{G_{shield}} + L\ tan(\delta)\ , \tag{3.2.6}$$

reduces to

$$\frac{1}{89000} = \frac{R_{s,Cu}}{G_{shield}}\ . \tag{3.2.7}$$

The theoretical surface resistance of OFHC copper at room temperature is given by

$$R_s(300K) = \frac{\rho}{\delta} = \sqrt{\rho\pi\mu_o\nu} = 9.8m\Omega\ , \tag{3.2.8}$$

where δ is the skin depth of copper and the resistivity ρ is $1.72\mu\Omega\ cm$.

To find the geometry factor for the electrodes, the maser resonator Q_c was also measured from $4.2K$ to $300K$ with copper electrodes. In this warm-up measurement, the Q_c at $4.2K$ was 21500 and at $300K$ Q_c was measured to be 4700. The ratio of these Q measurements gives the improvement factor of $R_{s,Cu}$ cooling from $300K$ to $4.2K$;

$$\frac{Q_c(4.2K)}{Q_c(300K)} = \frac{21500}{4700} = 4.5\ .$$

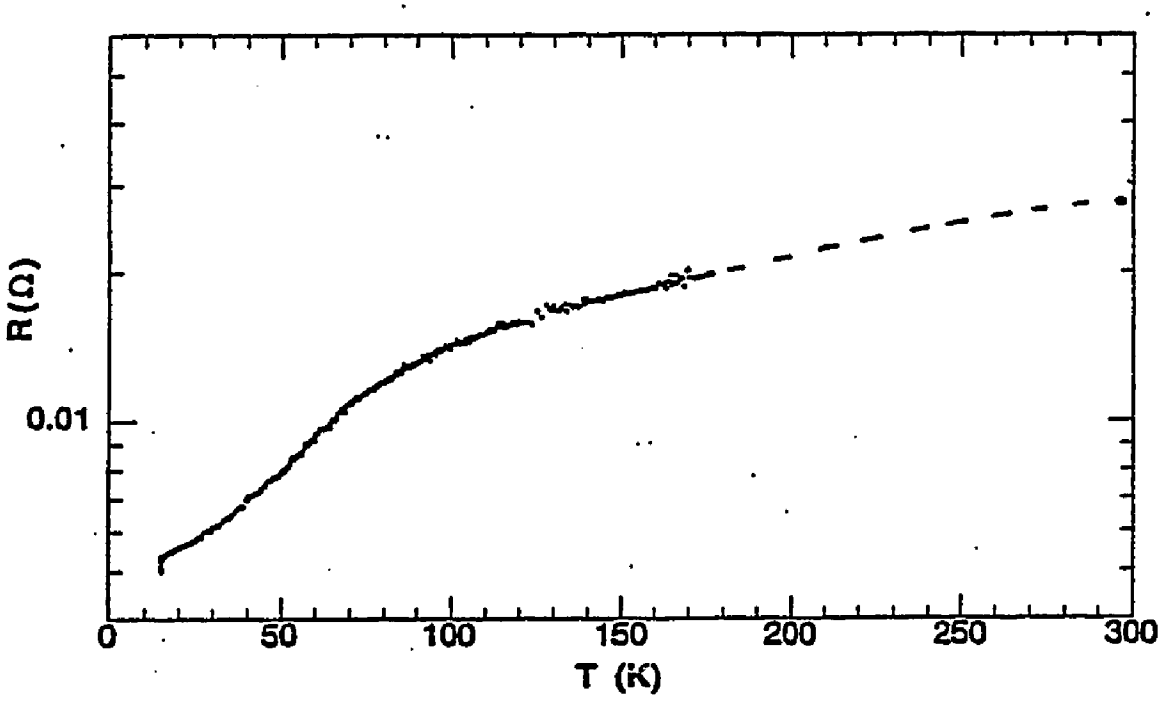

Figure 3.2.2 Surface resistance of niobium measured as a function of temperature.

From equation (3.2.8), $R_{s,Cu}(4.2K) = 2.2m\Omega$. This gives a total geometry factor G_c of 47Ω, $G_{shield} = 195m\Omega$ and therefore, $G_{electr.} = 63\Omega$. The measured curve of the copper surface resistance as a function of temperature is shown in figure 3.2.1.

To test these geometry factors, the quality factor of the cavity with the niobium electrodes was also measured from 4.2 to $300K$. Shown in figure 3.2.2, is the niobium surface resistance as a function of temperature, where the surface resistance was calculated from the warm-up measurement of Q_c using the geometry factors given above. There are three quantities that can be determined from this curve that describe the quality of the niobium. These are; the slope of the resistivity at $300K$, the actual resistivity at $300K$ and the residual resistance ratio (RRR). The manufacturer of the niobium quote that this sample of niobium has a resistivity slope of $5.925 \times 10^{-8} \frac{\mu\Omega}{^\circ C}$, a $300K$ resistivity is $15\mu\Omega\ cm$, and the RRR is 30. From figure (3.2.2), the slope of $\rho(300K)$ is calculated by finding two R_s values, solving for ρ for these points from equation (3.2.8), and dividing by the temperature spanned by these points. The measured slope is $6.5 \times 10^{-8} \frac{\mu\Omega}{^\circ C}$, which agrees to within 10% of the manufacturer's value. The measured value for $R_s(300K) = 29m\Omega$ is used to calculate $\rho(300K)$, yielding $\rho(300K) = 15.2\mu\Omega\ cm$ which agrees well with the manufacturer's value. The measured RRR is found by taking the ratio of the resistivity at $300K$ to the resistivity at $0K$ found from the extrapolated $R_s(0K)$ value. From figure 3.2.2, the extrapolated R_s at $0K$ is approximately $5m\Omega$, and RRR = 33. This good agreement suggest that these geometry factors adequately represent the maser resonator with the metal, normal conducting electrodes.

The loop-gap geometry factors indicate that 75% of the power losses occur on the electrodes. Without a quantitative understanding of the dielectric losses or an analytic solution for the fields, it would be difficult to improve on the accuracy of these numbers, or even comment on the error of the geometry factors. Since the niobium results are within 10% of the expected values, the total uncertainties must be about this size.

Results of YBCO Electrodes

The loop-gap resonator with YBCO electrodes was measured in a cryostat that allowed testing from $4.2K$ to room temperature. The cavity was evacuated to protect the YBCO from being contaminated by condensed water and to keep other liquids and ices from causing dielectric losses in the cavity. The cavity was immersed in liquid helium for cooling. While the cavity is cooled, the teflon cylinders provide the only heat path between the electrodes and the thermal bath. To improve the thermal contact between the electrodes and the rest of the cavity, the cavity is filled with helium gas. After the liquid cryogen boiled away, the cavity was allowed to slowly warm-up. During the warm-up, the cavity temperature and microwave properties were recorded by an automated measurement system, which is described elsewhere [71].

There have been more than a dozen pairs of superconducting electrodes. The quality of these electrodes, from 1989 to 1991, improved as the electrophoretic technique was customized for the unique application of the compact maser resonator. The following results are from selected electrode pairs, for comparison of magnet-

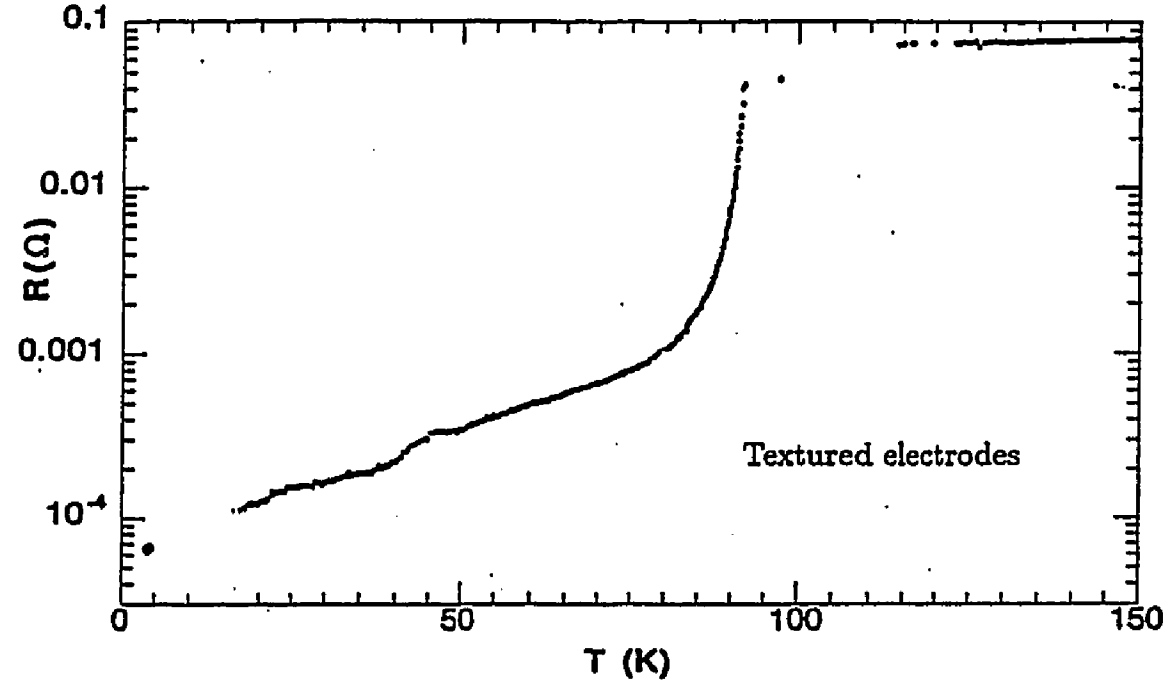

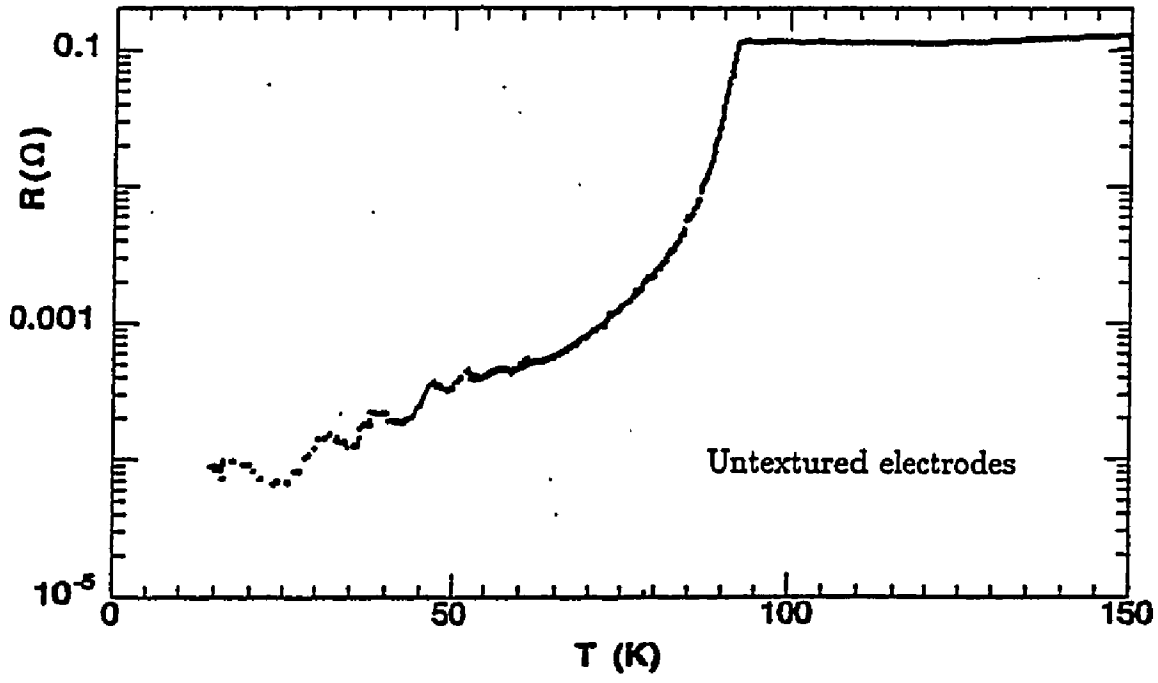

Figure 3.2.3 Surface resistance of textured and untextured YBCO layers on the silver electrode substrates.

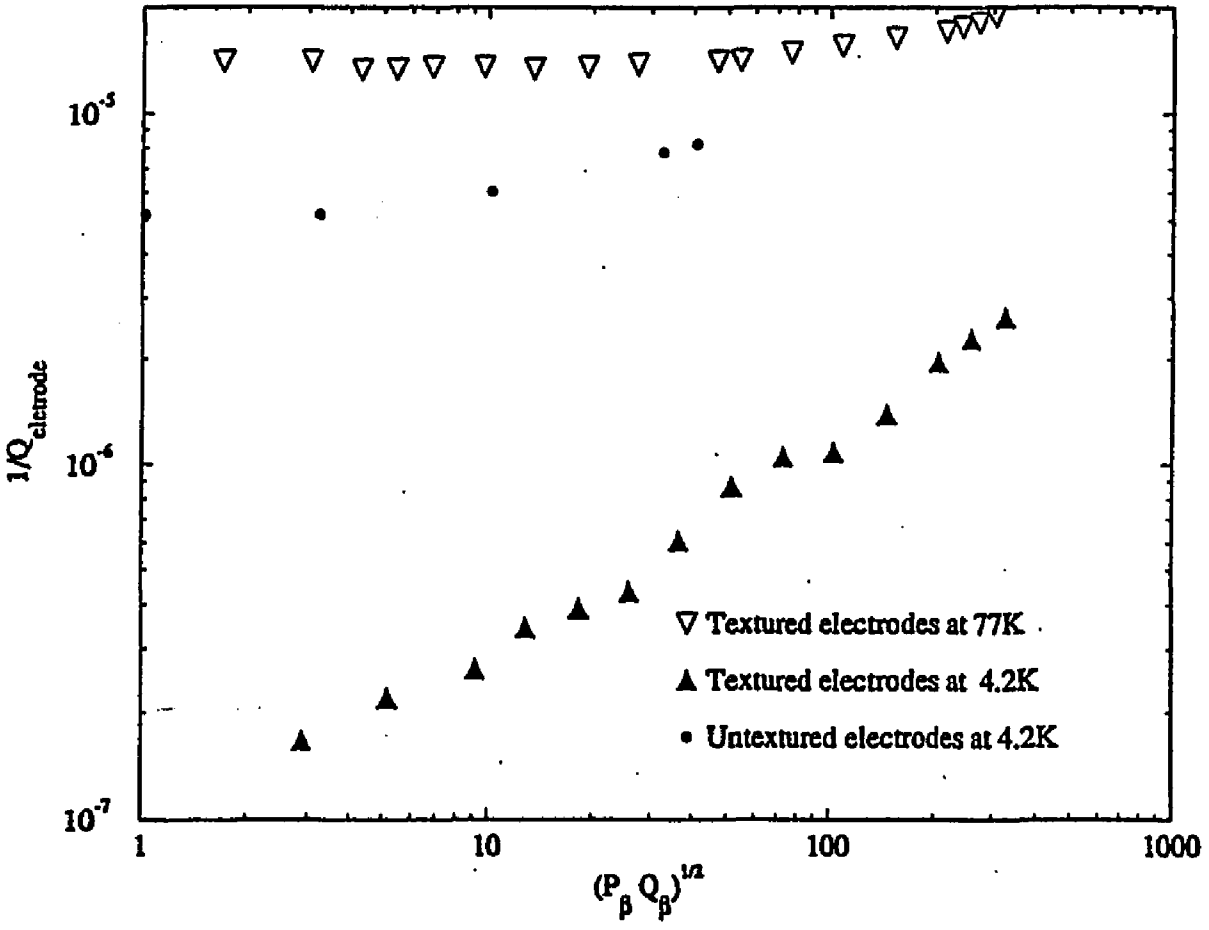

Figure 3.2.4 The measured inverse Q, $1/Q_{elect.}$, plotted as a function of the root of the total microwave energy in the cavity, measured for the untextured electrodes at $4.2K$ and the textured electrodes at $77K$ and $4.2K$.

Table 3.2.1 Measured Maser Resonator Q_c and R_s Values

Electrode Type		$R_s(m\Omega)[(P_\beta Q_\beta)^{1/2}]$	
		$77K$	$4.2K$
YBCO (textured)	$R_s =$	0.9 [17.1]	$\leq$ 0.10 [15]
YBCO (untextured)	$R_s =$	1.3 [43.3]	0.38 [12.2]
Copper	$R_s =$	3.9	2.2
Niobium	$R_s =$	10	$\approx$ 0.0001
Electrode Type		$Q_c[(P_\beta Q_\beta)^{1/2}]$	
		$77K$	$4.2K$
YBCO (textured)	$Q_c =$	31900 [17.1]	86000 [15]
YBCO (untextured)	$Q_c =$	26500 [43.3]	79500 [12.2]
Copper	$Q_c =$	12000	21500
Niobium	$Q_c =$	4800	89000

ically textured and non-textured electrodes. These results are compared with the loop-gap with copper electrodes to illustrate the improvement achieved with the YBCO electrodes.

Table 3.2.1 shows the Q_c values for the electrodes listed. Because Q_c is dependent on the magnitude of H_{rf}, the square root of the total stored energy in the cavity for each particular Q_c measurement is also given in table 3.2.1. At $77K$, the copper electrodes yield an unloaded Q_c of 12000. This is more than doubled with untextured YBCO electrodes, $Q_c = 26500$. Using electrodes that were magnetically textured during the deposition, increases the $77K$ Q_c to 31900. Using the geometry factors calculated above, the improvement of the textured electrodes over the untextured pair corresponds to a $0.4m\Omega$ decrease in $R_s(77K)$. Figure 3.2.3 shows the surface resistance of the textured and untextured electrodes as a function of temperature. Below the $92K$ critical temperature, the textured electrodes have a sharper transition than the untextured pair and the cavity with these electrodes reaches a higher $Q_c(77K)$.

Both the Q_c and the cavity frequency change with H_{rf}. The change in Q_c reflects the change in surface resistance of the YBCO as a function of the surface field. The change in frequency represents a change in the surface reactance X_s. The changes in these cavity parameters for the textured and untextured electrodes are listed in table 3.2.2. The magnetically textured electrodes are least sensitive to the increase in rf power. The Q_c goes from 88000 at the lowest power levels to 71000 over the power range measured. Figure 3.2.4 shows this dependence for

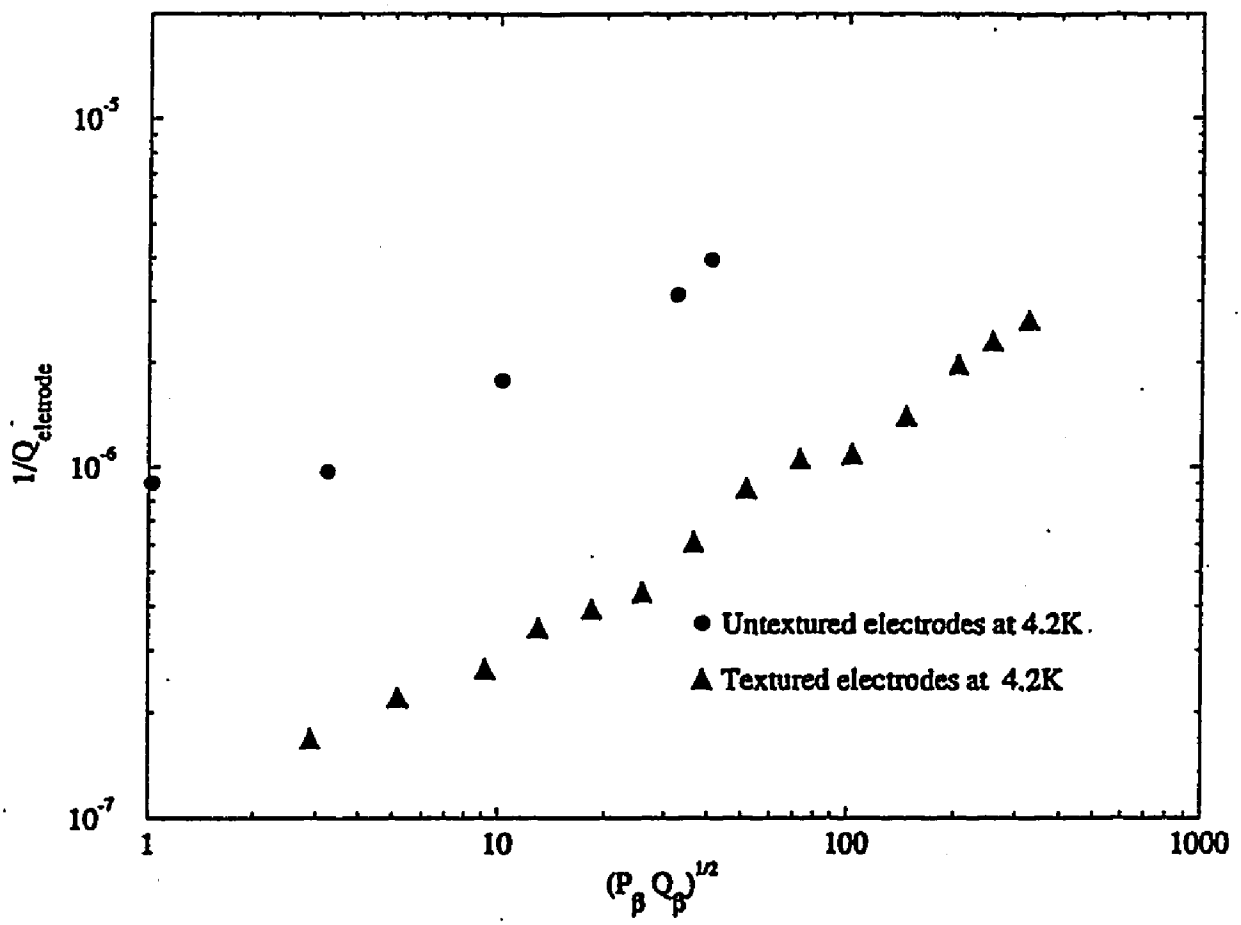

Figure 3.2.5 The measured inverse Q, $1/Q_{elect.}$, plotted as a function of the root of the total microwave energy in the cavity, measured for the textured and untextured electrodes at $4.2K$. A residual $Q_{elect.} = 4.3 \times 10^{-6}$ has been subtracted from the untextured electrode data, resulting in a line with a slope of 1/2. The residual $Q_{electr.}$ represents a residual resistanceof $R_{s,res.} = 280\mu\Omega$.

the untextured electrodes at $4.2K$ and the textured electrodes at 4.2 and $77K$. To remove the dependence on the geometry factors, the graph is plotted as the surface resistance divided by the geometry factor for the electrodes versus $(P_{\beta_1} Q_{\beta_1})^{1/2}$. The value is proportional to the maximum H_{rf} in the cavity, P_{β_1} is the power delivered to the cavity from the input coupling port and Q_{β_1} is the coupling Q of the input coupler.

At $77K$, the H_{rf} dependence of the surface resistance is not as obvious as the $4.2K$ dependence but this temperature dependence is consistent with results reported elsewhere [33]. For high rf fields the surface resistance increases as [8]

$$R_s = \omega\mu \left(\frac{\lambda_2 H_{rf}}{2J_c} \right)^{1/2} , \tag{3.2.9}$$

as defined in the introduction. The slope of the graph, for the textured $4.2K$ data, is approxiamately 1/2 which indicates that the YBCO is experiencing high rf fields somewhere in the cavity. The response of the untextured data at $4.2K$ does not have the same slope of the texture electrode data. This could be due to the large residual resistance dominating the relatively small changes of the R_s. Assuming that this last statement is correct, a constant value of $1/Q_{electr.,res} = 4.3 \times 10^{-6}$ can be subtracted from the untextured data. The residual surface resistance corresponding to the $1/Q_{electr.,res}$ is $R_{s,res} = 280\mu\Omega$. The resulting curve is shown in figure 3.2.5, where both the untextured and textured data have slopes of about 1/2. The untextured data in figure 3.2.5 form a line that is overall 5 times greater than the line formed by the textured electrode data. This difference between the textured and untextured data is indicative of a series resistivity, ρ_{2s}, that is 5 times larger

for the untextured material than for the textured material at $4.2K$.

Even though R_s is power dependent, the Q_c values obtained with the superconducting electrodes are large enough that a maser made with this compact maser resonator would oscillate. However, the stability of such an oscillation is unknown and will be evaluated in later sections. By equating the atomic beam power to the power loss found in the superconducting resonators, the threshold Q_c of oscillation is found to be about 14000. This threshold certainly depends on the many maser parameters and thus this threshold value is only an approximation.

CHAPTER 4

4.1 Mechanical Stability of the Resonator

As an accepted test device for the HTSSE experiment, the maser resonator was tested at NRL to insure the resonator's space worthiness. The testing of the resonator included rf and mechanical testing. During the mechanical tests, the cavity was vibrated for two minutes at a maximum level of $18.6 g_{rms}$ along each of the three body axes. It is not expected that a maser must operate under such violent conditions, rather, the devices must be qualified to survive such conditions during the satellite launch. To stabilize the electrodes from sliding in the teflon holders, a hole was drilled through the electrodes and teflon and a dielectric screw was inserted. The screw was placed in the center of the electrodes, where it would not seriously perturb the fields.

There was no discernable change in the Q_C of the resonator as a result of the vibration test. However, the frequency was slightly shifted. Upon inspection of the electrodes and teflon holders after the vibration test, it appeared that the electrodes were slightly misaligned at the gap. From this, it is concluded that there must have been some bending of the electrodes as the part of the electrodes near the gap, not supported by the teflon, is free to vibrate. However, this poses no problems for the HTSSE tests.

The teflon cylinders that support the electrodes have a larger thermal coefficient

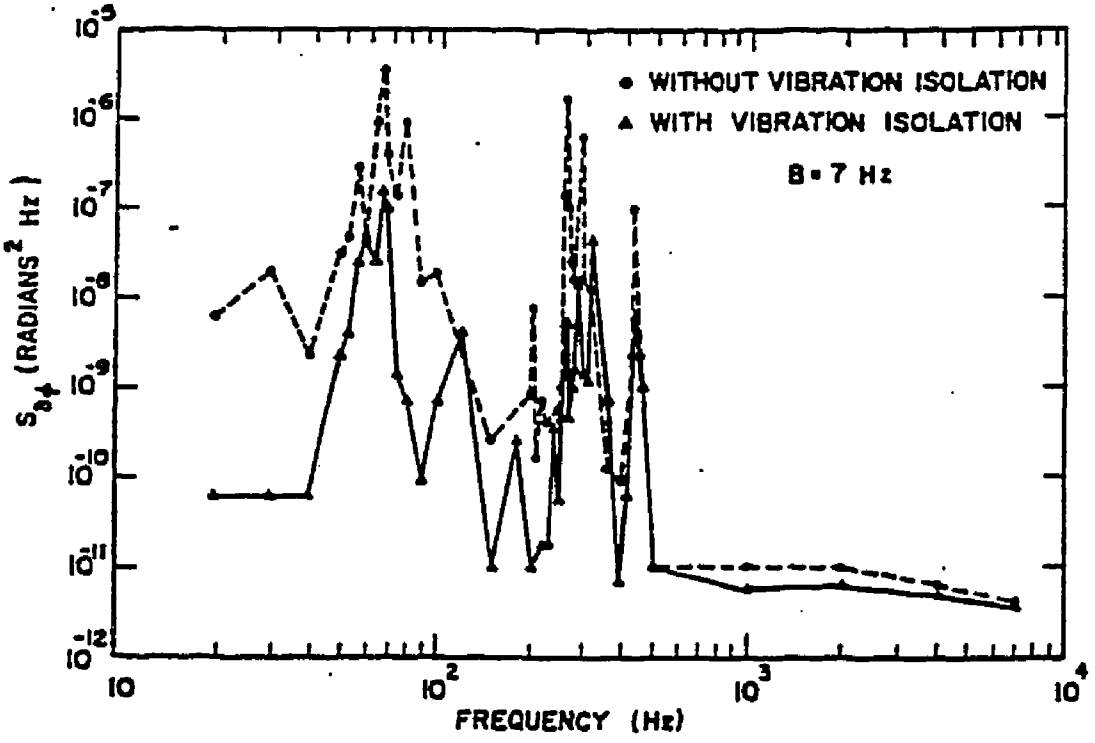

Figure 4.1.1 Noise spectrum of a superconducting stable oscillator before and after the test dewar was suspended from the laboratory floor. The vibrations are vibrations from vacuum pumps, air conditioning system and other natural vibrations of the building [34].

of expansion than the other materials in the cavity. The total contraction of the teflon in cooling from room temperature to $77K$ is 1.7%, where copper contracts only 0.3% over the same temperature range. Considering the teflon electrode holders, at $77K$, the teflon is more than $1mm$ shorter than the copper cavity (assuming that both copper and teflon where $7.5cm$ long at $300K$. The net effect of this contraction is that the teflon at $77K$ is not the same relative size as the copper and therefore, these pieces may become loose. If the electrodes and electrode holders are loose, they may be free to move or vibrate causing excessive fluctuations of the resonant frequency. Such vibrations are discussed more thoroughly in the next section.

Frequency Stability of the Resonator

The stability of the superconducting loop-gap resonator has been measured to determine if fluctuations due to the mechanical design of the resonator or the YBCO material would measurably affect the total stability of a maser using this cavity. Fluctuations of the superconducting loop-gap resonator will couple to the maser stability through the cavity pulling mechanisms described section 4.2 of this dissertation. Thus, fluctuations of the resonator frequency cause fluctuations of the hyperfine frequency that are about five orders of magnitude smaller than the measured resonator fluctuations. This implies that the loop-gap fluctuations must be very large before they will influence the maser stability. However, it has been reported that YBCO has $1/f$ fluctuations 7-10 orders of magnitude larger than normal metals and therefore this issue should be addressed. This excess noise is especially important if YBCO is to be used for superconducting stable oscillators (SCSO's).

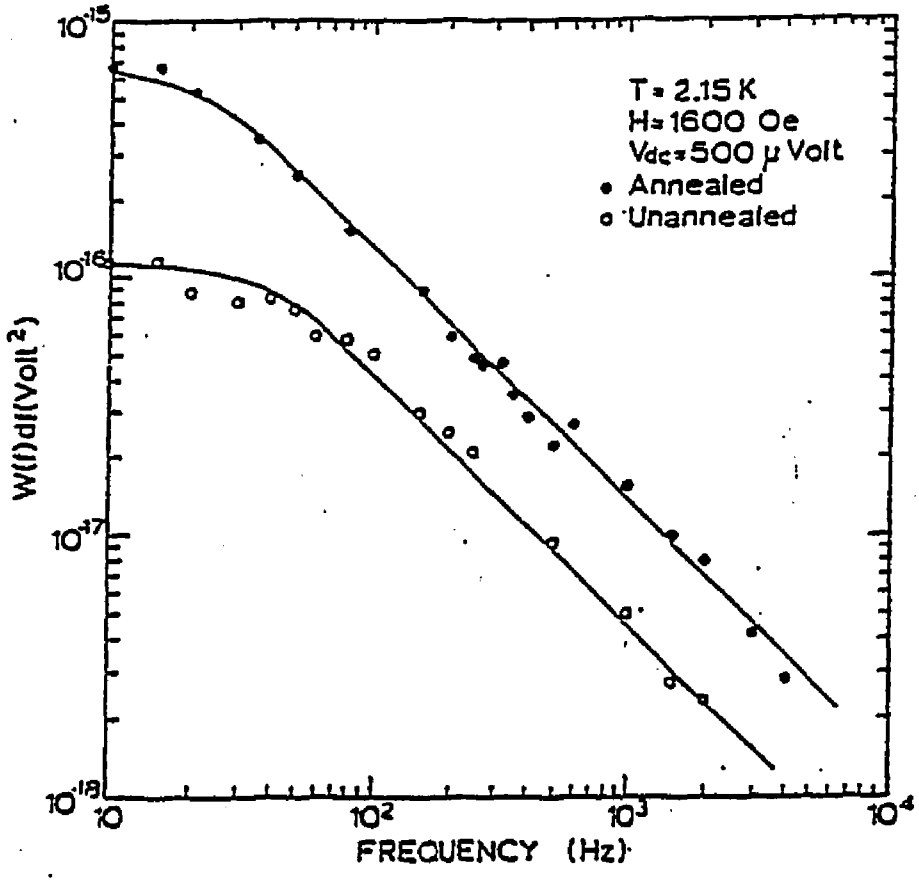

Figure 4.1.2 Grain size dependence of the noise power spectrum, measured before and after the sample was annealed. The lower curve is from the unannealed small grained sample and the upper curve was measured after the sample was annealed.

The noise measurements of SCSO's, passive resonators and other microwave components typically show the vibrational spectrum of the cryostat, vacuum system and the laboratory in which the tests are made. When these vibrations are strong enough, they shift the frequency of the resonator with the frequency of vibration, thus modulating the resonant signal. To minimize the coupling of vibrations the test cryostat can be lifted off the laboratory floor so that the dewar is hanging by "elastic suspension" [34]. Figure 4.1.1 shows the noise spectrum of an SCSO with and without this elastic suspension, taken from reference [34].

Noise measurements of the high temperature superconductors can also offer important information about the loss mechanisms in the material. Several studies on the flux flow state in type II superconductors have used the measurement of the noise power spectrum as an investigating technique. For dc noise measurements on low T_c superconductors (LTSC) it is found that the noise spectra arise from the fluxoids traversing the sample either singly or in bundles [35,36]. This motion gives rise to voltage pulses with a height proportional to the product of the bundle size and velocity. The duration of the voltage pulse is proportional to the transit time of the moving fluxons [37]. It is found that the grain size also affects the level of the noise power measured in granular $Pb_{80}In_{20}$ foil [35]. Given these results, it becomes necessary to consider the possibility of such fluctuations in the evaluation of high T_c superconducting resonators and devices.

LTSC

The technique used to measure the noise in the LTSC materials has generally

been a four probe measurement. Two leads apply a current across a sample while two other leads measure the voltage drop along a section of the sample parallel to the direction of the current flow. Whenever there is a magnetic field large enough to bring the superconductor into the mixed state and the Lorentz force acting on the fluxoid is larger than its pinning force, the fluxoids produce a flux-flow voltage. This voltage and the associated flux-flow noise is then measured by the two voltage sense leads. The voltage fluctuations are found to be proportional to $1/f$, for $f > 10^2 Hz$ and where f is the fourier frequency of the signal, as shown in figure 4.1.2. However the analysis of the power spectrum indicates that the level of noise is too large to be caused by the shot noise of single fluxoids but instead comes from the movement of flux bundles [38,39]. The fluxoids move in bundles due to the strong interaction between the fluxoids and due to the strong pinning effect. The bundles move in the same way as the single fluxoids would, but the bundle effect gives a flux-flow noise several orders of magnitude larger than predicted under the single fluxoid assumption. The voltage pulse caused by the bundle movement and the shape of the spectrum are assumed to be unchanged from the single fluxoid response [35].

The effects of grain boundries (pinning centers) have been measured on lead-indium foils [35]. The foils were first measured, using the four probe method, and then annealed and remeasured (figure 4.1.2). The results indicate that the grain boundaries impede the flux-flow and therefore effectively reduce the noise power in the sample by nearly an order of magnitude at the lowest frequencies. Conversely, when there are fewer pinning centers, the flux bundles can flow more freely and

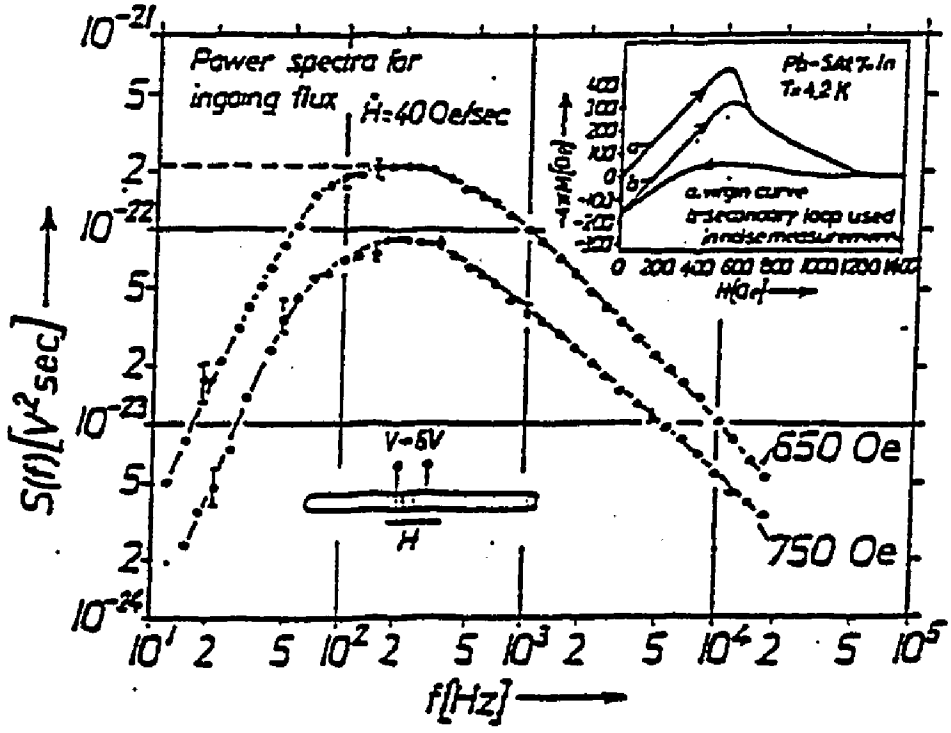

Figure 4.1.3 Noise spectrum of shot noise in a LTSC caused by fluxoid bundles entering a sample in a time dependent magnetic field [43].

produce more noise. Therefore, small grained samples have less flux-flow noise than large grained samples.

In a time dependent magnetic field, there are additional noise components that have a spectrum analogous to Barkhausen noise associated with domain switching in magnetic materials [38]. This is characterized as a broad maximum in the spectrum (a hump) between 100 and $1000Hz$ (figure 4.1.3). In superconductors this type of noise spectrum is attributed to the 'blocking effect' of flux bundles: this means that some fluxoids moving into the sample momentarily reduce the probability that other fluxoids can enter the material at the same location until the fluxoids move a distance into the material. Because there is a characteristic time for this process, there is likewise a frequency at which these events are most likely to be correlated [38].

HTSC

For the high temperature superconductors (HTSC) the noise spectra are found to be different than the spectra of the LTSC materials. There is no excess noise found at low frequencies ($1/f$), in the dc measurements of HTSC's, that can be directly associated with the superconducting state (like flux-flow in the LTSC materials). However, the YBCO and BSSCO materials have a much higher noise level in the normal state, above T_c, than is found in other metallic conductors. The temperature dependence of this noise is sometimes found to be continuous through the superconducting transition. This excess noise could hinder the detection of the noise processes associated with the superconducting state.

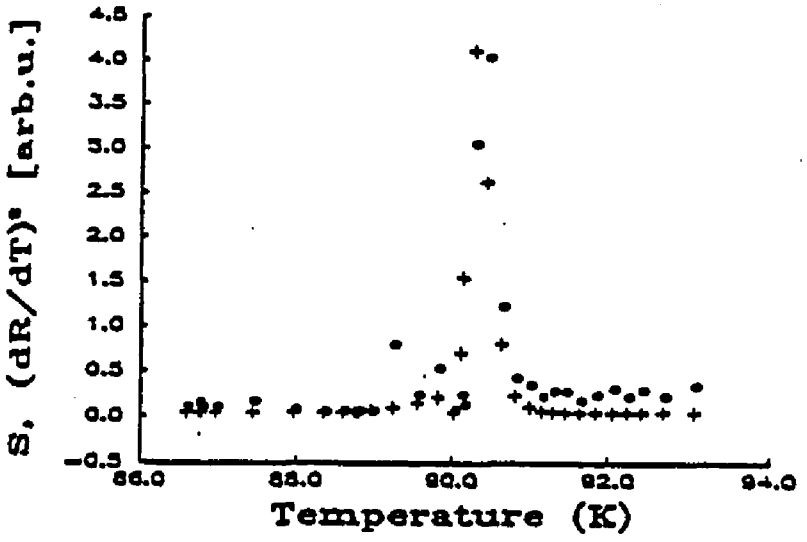

Figure 4.1.4 Excess noise in the spectrum measured near the superconducting transition temperature [41].

To date, the mechanisms of this $1/f$ noise in the copper oxide superconductors have not been identified although various models have been proposed. For instance, composite effects and an anisotropic conduction have been considered as possible sources of the excess $1/f$ noise [41]. Composite effects such as grain boundries, twin boundary layers, dislocation line defects, and stacking faults are all barriers that are *at least* 10 angstroms wide [42]. Some of these defects will be larger than the coherence length in the $a-b$ plane and could be a considerable tunnel barrier that can hinder conduction of the electrons (think of semiconductor shot noise with many small grains). Another possible source of the noise is the superconducting anisoptropy, and tunneling between copper oxide planes is presumed based on the difference between the c direction coherence length (<0.2 nm) and plane spacing (0.4 nm). However, both of these models could only justify excess noise measured in the superconducting state and not normal state noise. In the normal state, it is found that the magnitude of the $1/f$ noise spectral density is typically 7 - 10 orders of magnitude higher than that found in conventional materials with similar geometries and sizes [40]. This would imply that the measured noise in the HTSC materials is not necessarily a superconducting effect.

It has been found that the noise power remains unchanged or drops continously when the temperature is lowered through T_c. There are discrepancies in the literature regarding the measured noise spectra for temperatures near transition. Some authors report that there is a large increase in the noise power at transition [43] while other investigators have not found this temperature dependence (figure 4.1.4)

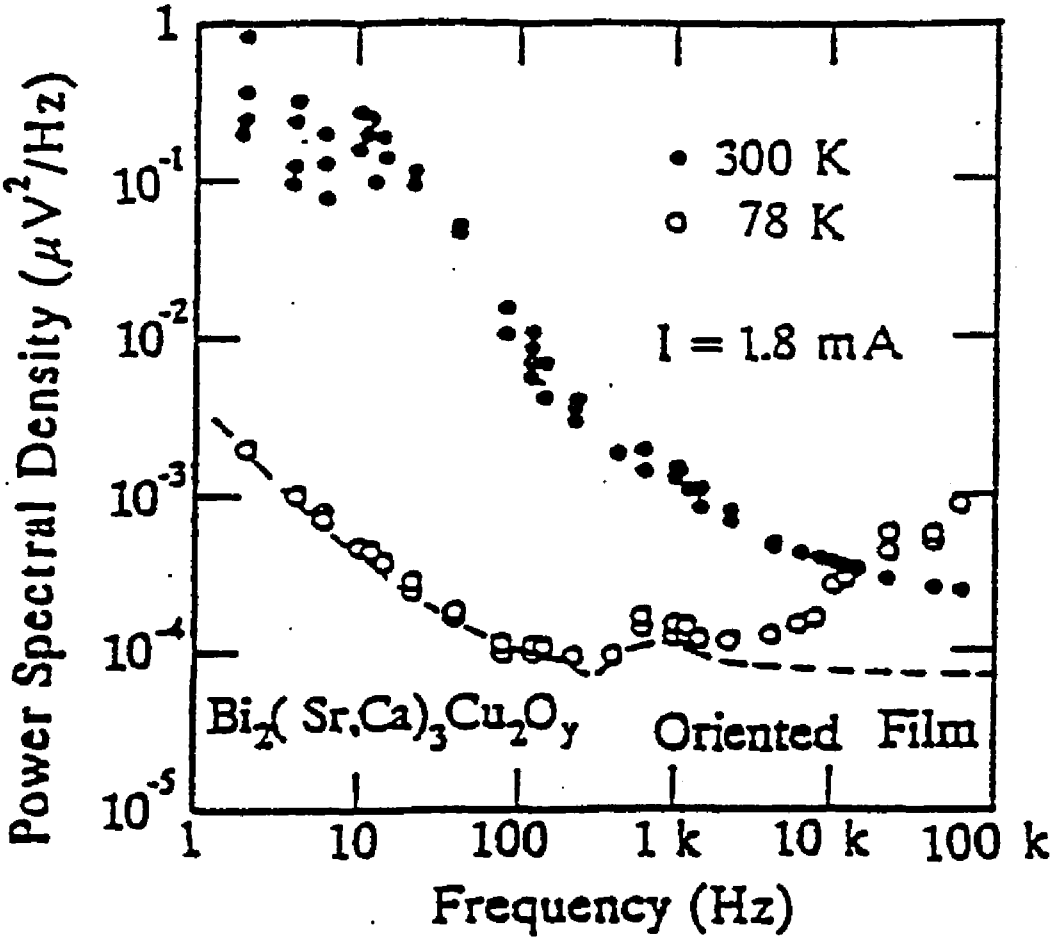

Figure 4.1.5 Noise spectrum measured in a HTSC sample at $300K$ and $78K$ [41].

[40]. The existence of this transition noise could be dependent on the quality of the samples but this is difficult to predict. However, in the HTSC materials the power spectral density of voltage fluctuations is found to be similar for both YBCO and BSSCO copper oxides. The normal state and superconducting state spectra are generally $1/f$ and, as mentioned above, have a much greater magnitude than LTSC materials in the normal state.

This excess noise has been measured for single crystal BSSCO, polycrystalline YBCO and BSCCO, and thin film YBCO and BSSCO [40,41,43]. The overall magnitude of the noise was comparably high for BSSCO single crystals, thin films and bulk samples. This would seem to imply that grain boundaries are not the dominant source of the excess noise. A common feature in two of these measurements [41,43] was an increase in the noise powers at Fourier frequencies above $100Hz$ (figure 4.1.5). Figure 4.1.5 shows this increase in the 78K data curve, where for frequencies less than $100Hz$ the spectrum is generally $1/f$.

One possible reason for this high level of noise is that the HTSC's are two dimensional conductors. In a study of $1/f$ noise in quasi one dimensional metal-oxide-semiconductors, it is reported that: "In one and two dimensions we have the novel results that the conductance fluctuations induced by moving a *single* scattering center are as large as those produced by changing the entire sample! Small ($\approx 0.5\%$) discrete conductance jumps have been observed ... and attributed to the filling of individual trap states in the oxide which affects the electron mobility " [44]. Perhaps these results could be applied to the HTSC materials.

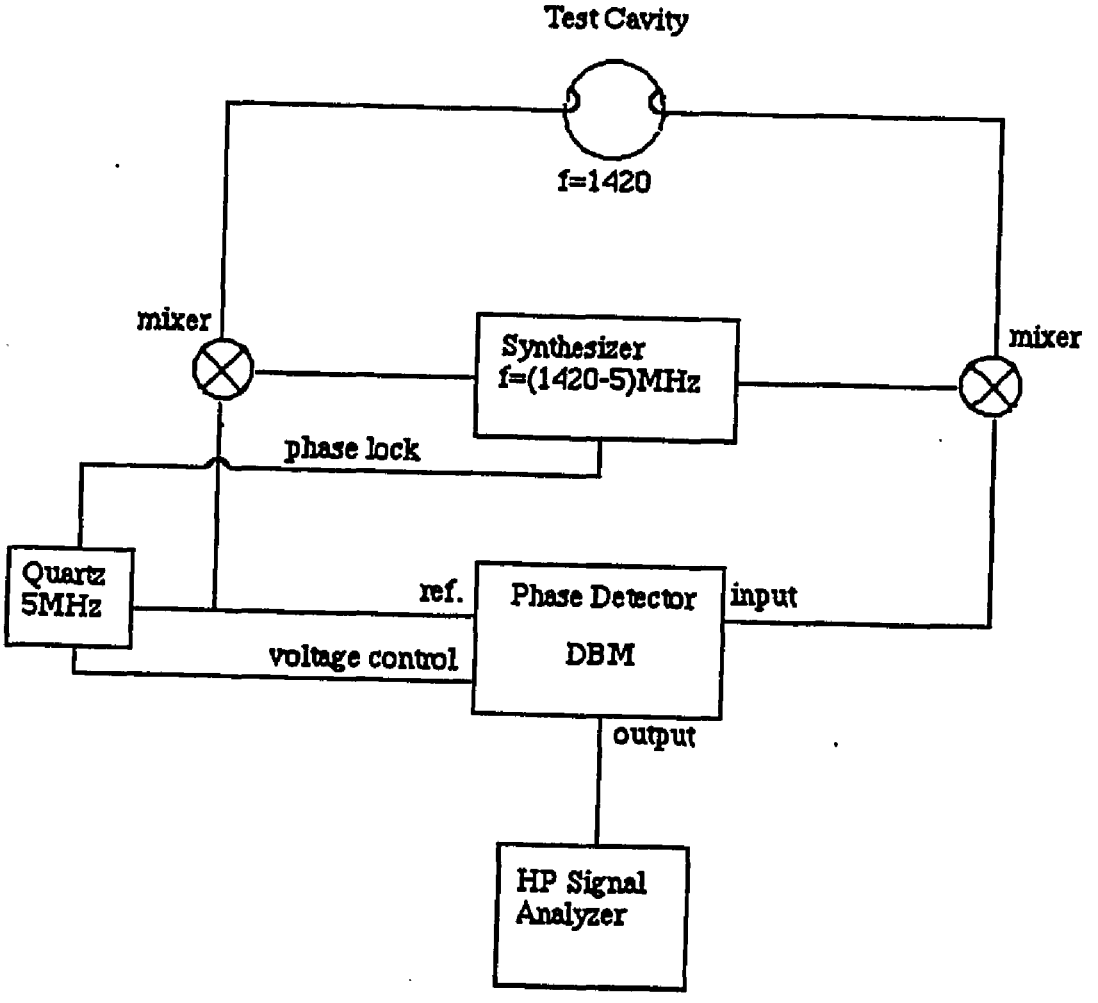

Figure 4.1.6 Schematic of test circuit used to measure the noise spectrum of the superconducting loop-gap resonator. For simplicity, amplifiers and attenuators were not included in the diagram. The quartz oscillator is phase locked to the synthesizer and voltage controlled by the phase detector.

So far there are many questions that are still not investigated. For example, Is there a frequency dependence to the HTSC noise spectrum? What are the relationships between noise spectra and R_s, X_s, applied magnetic magnetic field, etc.? In comparing the new superconductors with the classical superconductors, it is difficult to find similarities between the two groups. At this time, it is impossible to determine the sources of the noise measured in the HTSC materials. It seems fairly clear that the noise is much greater in these materials above *and* below transition when compared to the LTSC materials. This noise could in part be due to the relatively low number of charge carriers in the granular ceramic superconductors. It could also be linked to the dimensionality of the HTSC material [44]. Whatever the cause, this high intrinsic noise could easily dominate flux-flow or other noise processes reasoned to be found in the HTSC's, in analogy to the LTSC's.

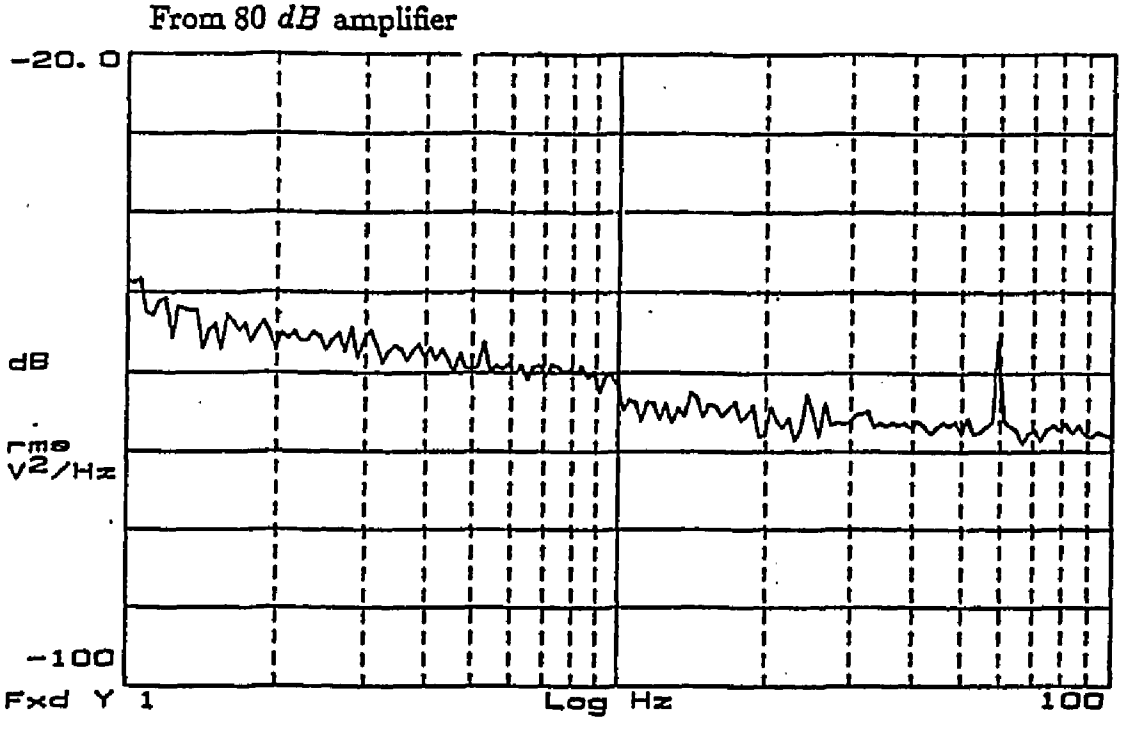

Figure 4.1.7 Measurement of the background noise spectrum in the test circuit shown in figure 4.1.6.

Noise Measurements

The noise measurements of the loop-gap cavity were made with the circuit shown in figure 4.1.6. A signal from a $5MHz$ quartz reference was mixed with a synthesized signal so that the two frequencies added to equal the cavity resonance frequency. This signal was passed through the loop-gap resonator. The output from the resonator was mixed with the same synthesized signal so that the carrier frequency was again $5MHz$. A phase detector, which is basically a dc coupled double balanced mixer (DBM) and a set of amplifiers, mixes the $5MHz$ output signal with the quartz reference frequency, giving a dc voltage whose fluctuations represent the loop-gap fluctuations about the carrier signal. The measured fluctuations are proportional to the difference in phase between the reference signal and the resonator output signal. The sensitivity of the phase detector depends on the phase slope of the resonator. In measuring the loop-gap resonator, the phase detector can resolve changes in cavity frequency as small as $100Hz$. The output of the DBM is sent to a signal analyzer (HP 3561A) that produces a graphical representation of either the time or frequency domain response of the DBM. The output of noise power versus frequency is, as described in the introduction, a single sideband measurement; the absolute value of the fourier frequency is plotted.

Before the loop-gap is measured, the background noise of the measurement circuit is recorded. To maintain the same phase detector input level during both the cavity and background tests, the cavity is replaced with attenuators that have the same insertion loss as the loop-gap, at its resonant frequency. The background

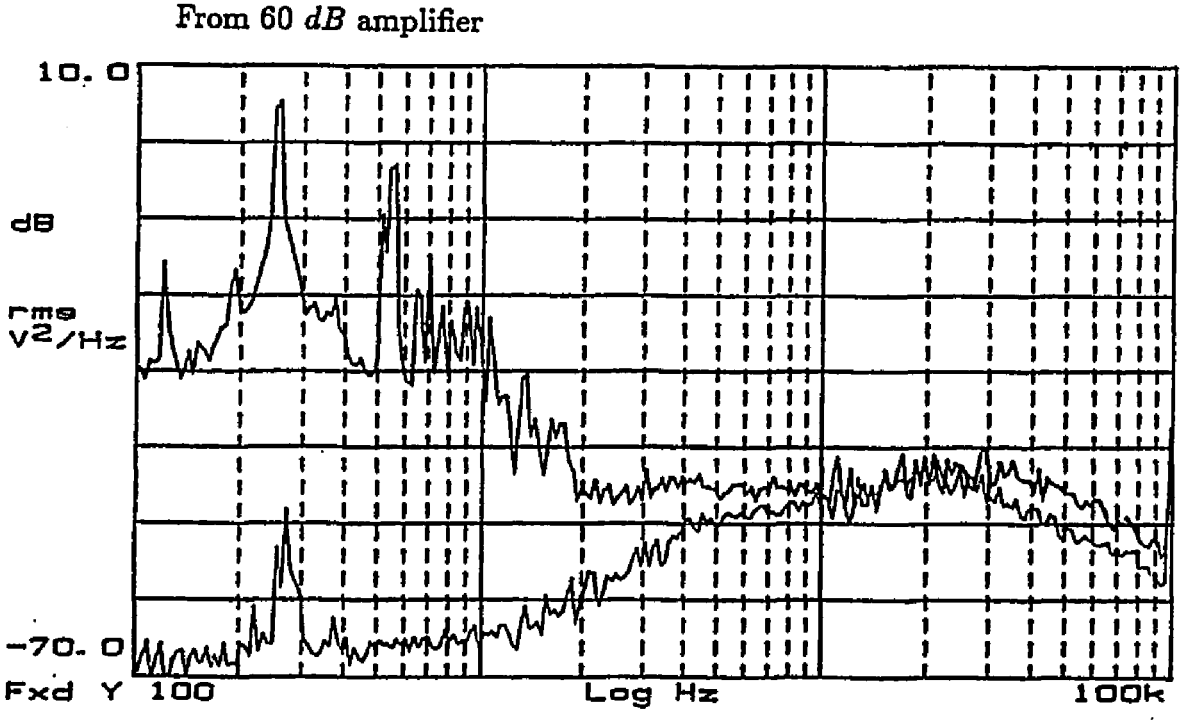

Figure 4.1.8 Measured noise spectrum for the loop-gap resonator showing the improvement achieved by using a elastic hanger for vibration isolation. The upper curve is without isolation against vibrations and the lower curve is measured with the cryostat hanging from an elastic strap.

measurement is shown in figure 4.1.7. This spectrum was measured using an 80 dB amplifier at the output of the DBM and the power levels must be appropriately adjusted. From $20Hz$ out to 10^5Hz, the background signal is flat at a level of $-150dB$ on the V^2/Hz scale. Below $20Hz$, the spectrum is $1/f$. The scale of power is measured in terms of V^2_{rms}/Hz. This can be converted to the familiar form of $S_\phi(f)$, which is expressed as $radians^2/Hz$, by multiplying V_{rms} by the calibration factor of the DBM. The DBM was calibrated and found to have $30rad/V$ at $30dB$ gain, corresponding to $1.07V_{rms}/rad$. Therefore, form table 2.3.1, the background level at $1Hz$ corresponds to a $\sigma(\tau = 1sec.) = 6.4 \times 10^{-12}$.

For isolation from mechanical vibrations, the cavity was suspended from an elastic hanger. A small dewar was filled with LN_2 and a stainless steel can was placed in the nitrogen. The steel can had no nitrogen in it but was surrounded by liquid nitrogen, so when the test cavity was suspended in the steel can, radiative heating was minimized. This also kept the cavity from being vibrated from boiling cryogen. To cut down on convective heating, two foam baffles were fixed to the suspension line. These baffles made no physical contact with the dewar but were a close fit. Figure 4.1.8 shows the improvement of mechanical isolation using this design.

Noise Test Results

The power spectral density of frequency fluctuations in the loop-gap resonator was measured at $77K$ with both copper and YBCO electrodes. The cavity with the copper electrodes is used to determine the fluctuations due to mechanical vibrations. The measured difference between the copper and YBCO electrodes should indicate noise associated with the YBCO material.

The cavity with copper electrodes measured at $300K$ shows a slightly increased $1/f$ component, where below $100Hz$ the power spectrum has a slope of minus one. This spectrum was measured with the cavity suspended in the dewar before LN_2 was filled. The lowest level reached is $-130dB$, which is $20dB$ higher than the background measured without the cavity. Above 10^3Hz the noise power rises to a maximum of $-110dB$ at $20KHz$. This maximum is characteristic of amplifier residual phase noise [45]. This spectrum shows very few vibration peaks due to the elastic isolation.

When the copper cavity is cooled to $77K$ the noise level between 10^2 and 10^5Hz remains unchanged. However, the low frequency spectrum is greatly increased. Below $1Hz$ the curve is proportional to $1/f^3$ and between 1 and $10Hz$ the curve is proportional to $1/f^2$. These low frequency fluctuations indicate changes with long time constants such as temperature drift. During the $77K$ measurement, the frequency would drift faster than the phase lock loop could compensate. The phase lock was an integrated voltage that changed proportionally to the drift. Seldom did the frequency drift slower than $100Hz/5min$ and the low frequency spectra take at

least $15min$ per measurement, longer if the spectrum is averaged over several measurements. Using the cavity frequency temperature coefficient of $10KHz/K$, this frequency drift arises from a temperature drift of $0.002K/min$. This was also a problem with the superconducting electrode measurements at $77K$. The temperature fluctuations also dominated the spectrum so that the measurements gave results similar to those for cold copper electrodes. Unfortunately, the temperature drift made the determination of additional noise from the superconductors impossible.

Throughout all of the measurements, the loop-gap cavity was extremely microphonic. The sensitivity to vibrations created the need to physically isolate the cavity which caused, in turn, poor thermal contact to the nitrogen bath and therefore, the temperature was not constant. The measured results show vibrations that are typical of SCSO's that have Q_c values orders of magnitude larger than the superconducting loop-gap cavity and therefore steeper phase slope. The fact that this cavity reacted to laboratory vibrations like a SCSO but with a phase slope orders of magnitude lower implies the need for a sturdier mechanical design which would make the electrodes more rigid.

In a redesigned cavity the teflon should also be replaced with a material that has a thermal expansion coefficient similar to the electrode expansion coefficient. As the teflon electrode holder shrinks with decreasing temperature, the electrode gap becomes smaller and the frequency decreases (see figure 2.2.5). As the teflon shrinks, the electrodes are also contracting but the thermal coefficient of the teflon is much larger than the thermal coefficient of the electrode material (silver). The

net thermal contraction causes the gaps to become smaller and the frequency is reduced. This would greatly reduce the temperature frequency drift and may serve as a frequency compensation technique.

4.2 Maser at 77k

The performance of a frequency standard can be judged according to two separate criteria; the precision of the oscillation frequency (stability), or the reproducibility (accuracy) of the oscillation frequency. For example, a cesium clock is used as the world time keeping standard because it reproducibly oscillates at a given frequency. However, a cesium clock has fractional frequency fluctuations that are generally one to two orders of magnitude larger than a hydrogen maser and therefore a maser is more precise than a cesium clock. The collisions in the hydrogen maser storage bulb perturb the hyperfine frequency such that the unperturbed or 'free space' frequency cannot be determined. A cesium clock has an atomic beam so that there are collisions with a storage container. Also the atoms of the atomic beam have roughly the same velocity so there are no atomic collisions. As a result of these collisions, the maser frequency is shifted by an amount that cannot be determined. Since no such collisions are present in the cesium standards, a cesium clock is more accurate.

For the maser considered here, frequency stability is the objective and not necessarily the actual oscillator frequency. However, frequency shifts do become important when the frequency shifts couple to the frequency stability. This happens when the frequency shifts are a function of systematic variables like temperature, humidity, magnetic field, and so on.

The systematic and random perturbations that are inherent in the maser will affect the hyperfine line width and the frequency of the measured hyperfine signal.

The line width or line quality factor, Q_l, is an important parameter because, for a given signal to noise ratio, it is easier to determine the center of a narrow line than that of a broad line. Furthermore, a reduction in the line Q will increase the coupling between the hyperfine frequency and the cavity frequency (cavity pulling) [47]. For this reason the broadening mechanisms must be identified and minimized wherever possible.

Relaxation Processes in the Maser

The hyperfine transition from the $|F = 1, m = 0\rangle$ to the $|F = 0, m = 0\rangle$ state will spontaneously occur very infrequently. In free space, the decay of the upper state has a transition lifetime of about 10^7 years. This decay time would lead to a negligibly small contribution to the linewidth. The hydrogen radiation rate is increased by a factor of 80 when the radiating atom is enclosed in a cavity whose resonant frequency is tuned to the transition frequency [46]. Of much greater importance to the measured linewidth is the effect of coherent radiation that can stimulate the transition. The radiation lifetime is reduced by a factor equal to the difference in the number of atoms in the two energy levels [46]. In the hydrogen maser, the presence of nearly 10^{12} upper energy level atoms in the interaction region of a microwave cavity reduces the radiation time to about 10 seconds [46]. However, this total relaxation time is still much longer than that encountered when all of the processes in the maser are considered.

All of the relaxation processes in the maser fall into one of two categories: processes that affect the coherence of the atomic transition phase with the applied rf

field; and processes that effectively prevent an atom from making further contributions to the radiation field. The loss of coherence is analogous to the transverse relaxation in nuclear magnetic resonance (NMR), while the loss of atoms able to make the desired transition is analogous to longitudinal relaxation. Using the standard NMR terminology, the total longitudinal relaxation time is given by T_1, and the corresponding longitudinal relaxation rate is $\gamma_1 = 1/T_1$. Likewise, the transverse total relaxation time is given by T_2 and the total transverse relaxation rate is $\gamma_2 = 1/T_2$.

We consider that T_1 is the characteristic time for the loss of atoms in the upper energy state. These atoms are lost due to escape from the bulb or non-adiabatic collision with other atoms or the teflon coated walls. These collisions leave the interacting atoms chemically reacted or in a different atomic state [47]. Furthermore, when two hydrogen atoms collide there is a possibility of spin exchange between the atoms. Additionally, if the applied dc magnetic field in the cavity is not uniform, a moving atom experiences a time varying magnetic field that can cause Zeeman transitions analogous to Majorana transitions in atomic beams [47].

The total transverse relaxation is the sum of the adiabatic contributions to the decorrelation of atomic phase coherence and the non-adiabatic terms can also contribute to broadening because of the finite atomic state lifetime. The total perturbation rate is related to the hyperfine linewidth by

$$Q_l = \frac{\nu_o}{\Delta\nu_o} = \frac{\omega_o T_2}{2} = \frac{\omega_o}{2\gamma_2} , \tag{4.2.2}$$

where Q_l is the atomic line quality factor, $\Delta\nu_o$ is the hyperfine full width at half

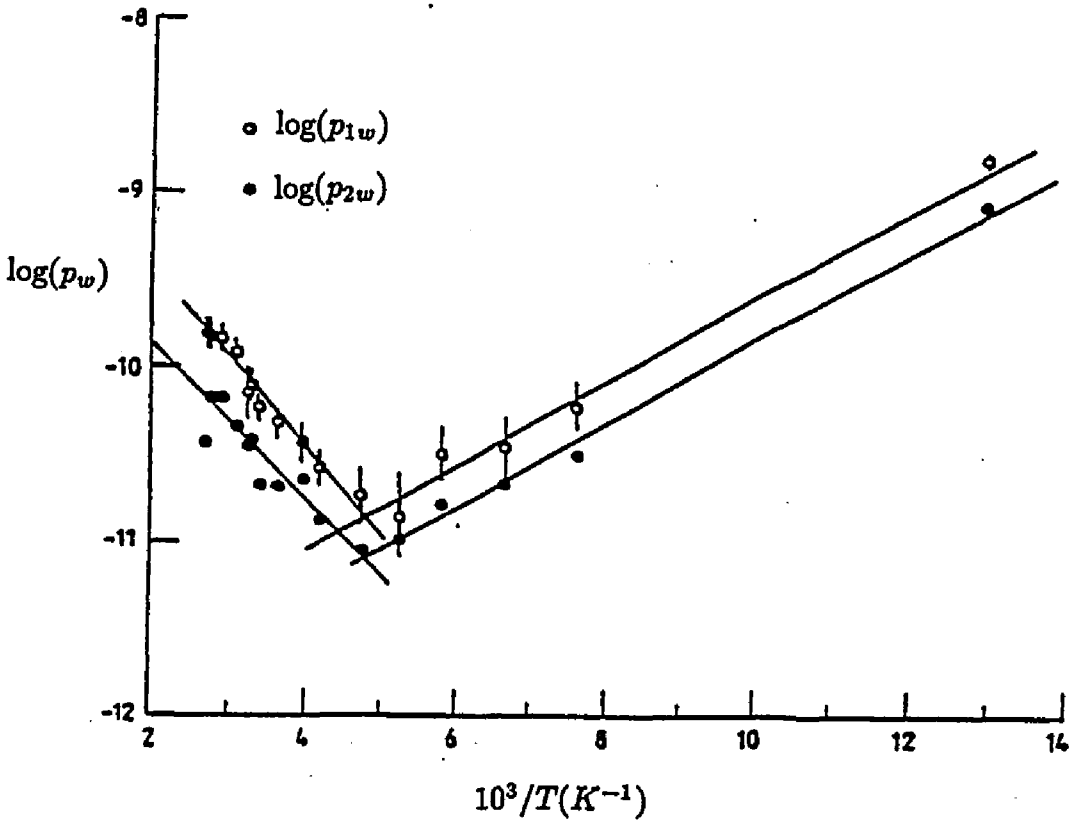

Figure 4.2.1 Relaxation probability of the population (p_{1w}) and the coherence (p_{2w}) of the hydrogen atoms on a teflon surface as a function of temperature (from reference [6]).

maximum, and ν_o and ω_o are the resonant and resonant angular frequencies, respectively.

In general there are more transverse relaxation mechanisms than longitudinal mechanisms since all of the longitudinal (T_1) processes are also processes that can cause line broadening. As mentioned above with T_1, adiabatic collisions, the spread of frequencies associated with magnetic field inhomogeneities, escape from the bulb, and spin exchange are also line broadening processes. Other contributions to T_2 come from first and second order Doppler broadening, and pressure broadening. In the storage bulb, the atoms are perturbed by collisions with the teflon walls. These perturbations from the atom-wall collisions increase exponentially as the operating temperature of the maser is decreased and the interaction time of the collision becomes long [6,47]. The other transverse relaxation mechanisms are dependent on the temperature through the velocity of the hydrogen atoms.

Table 4.2.1 lists the largest perturbative mechanisms that contribute to the total transverse and longitudinal relaxation rates calculated for the compact maser at $77K$ and $340K$. Because the average atomic velocity at $77K$ is half of the average $340K$ velocity, the spin exchange relaxation processes, which are proportional to velocity, are about half as large as the warmer maser values. Conversely, the magnetic inhomogeneity rates are larger at $77K$ because these rates are a function of the time between wall collisions and therefore inversely proportional to atomic velocity [47].

At the lower temperatures, the wall relaxation becomes the limiting broadening

Table 4.2.1 Relaxation Processes in the Compact Maser

Process	*Equation**	$\gamma(77K)$	$\gamma(340K)$
Wall Relaxation:			
	$\gamma_{1w} = n_w \left(7.3 \times 10^{-6} exp(230/T)\right)$	$4.45 sec^{-1}$	$1.0 sec^{-1}$
	$\gamma_{2w} = 1.33\gamma_{1w}$	$3.34 sec^{-1}$	$0.5 sec^{-1}$
Magnetic Field Inhomogenieties:			
Majorana Transitions	$\gamma_{1H} = \frac{3300}{n}$	$0.11 sec^{-1}$	$0.054 sec^{-1}$
Phase Decorrelation	γ_{2H} = see ref. [47]	$4 \times 10^{-7} sec^{-1}$	$2 \times 10^{-7} sec^{-1}$
Spin Exchange Relaxation: $n = 2 \times 10^9 cm^{-3}$			
	$\gamma_{1s.e.} = (n\sigma\bar{v}_r)$	$0.85 sec^{-1}$	$1.80 sec^{-1}$
	$\gamma_{2s.e.} = 2\gamma_{1s.e.}$	$1.7 sec^{-1}$	$3.60 sec^{-1}$

mechanism. The wall relaxation is caused by the interaction of the hydrogen atoms with the storage bulb surface. The strength of this perturbation is a function of the hydrogen-wall interaction time which in turn depends on the available thermal energy to remove the atom from the wall [49]. These relaxation rates have been measured and are found to be [6]

$$\gamma_{1w} = p_{1w} n_w$$

and

$$\gamma_{2w} = \frac{3}{4}\gamma_{1w} = p_{2w} n_w \ , \tag{4.2.3}$$

where n_w is the average collision frequency of the atoms with the walls,

$$n_w = \frac{A_b}{4V_b}\bar{v}_a \ ; \quad \bar{v}_a = \left(\frac{8KT}{\pi m}\right)^{1/2} \ , \tag{4.2.4}$$

where V_b is the storage bulb volume, A_b is the storage bulb inner surface area and v_a is the average atomic velocity and p_{1w} and p_{2w} are the probabilities of relaxation per collision.

Figure 4.2.1 shows the temperature dependence of the longitudinal and transverse relaxation rates. For temperatures below $200K$, the relaxation probability per collision is empirically found to be $p_{1w} = 7.3 \times 10^{-6} exp(230/T)$.

The bulb relaxation rate, γ_b, due to the atoms escaping from the bulb is not listed in table 4.2.1 because this relaxation rate can be adjusted after the maser resonator has been designed. γ_b is a function of the bulb volume V_b, velocity of the atoms $\bar{v}_a$, and the entrance aperture area A_a,

$$\gamma_b = K\frac{\bar{v}_a A_a}{4V_b} \ , \tag{4.2.5}$$

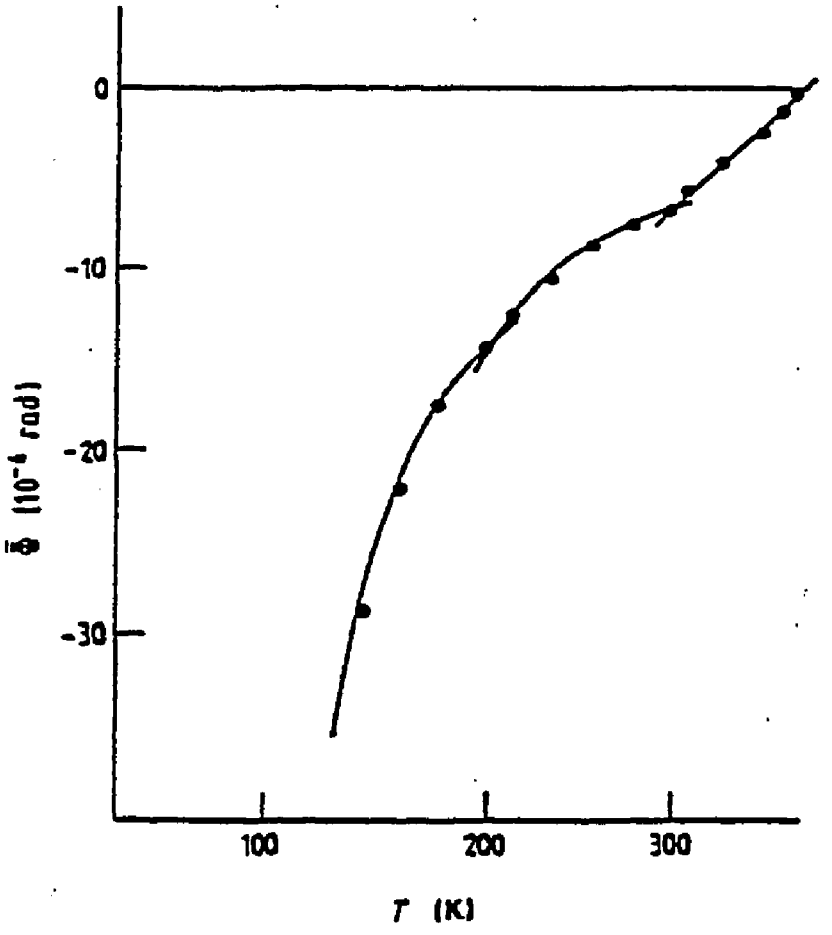

Figure 4.2.2 Average phase shift per collision of hydrogen atoms with a teflon surface (from reference [6]).

Here K is a correction for a collimating tube at the entrance of the bulb [15]. The relaxation rate can be chosen by changing the size of the aperture or the length of the collimator tube, such that the stability of the maser frequency is maximized. The bulb relaxation contributes equally to the total relaxation rates, γ_1 and γ_2 [47] and for a properly built maser, $\gamma_1\gamma_2 \approx \gamma_b^2$ [50].

The spin exchange relaxation rates are also not fixed. Since the spin exchange depends on the number density of atoms, n, and n is a function of the atomic beam current and γ_b, these relaxation terms will depend on the maser operating conditions. This will be discussed in the maser optimization section. The spin exchange rates given in the table are approximate values.

Frequency Shifts

The measured value of the hydrogen hyperfine transition frequency is always different from the true 'free space' value. This frequency offset adds uncertainties in the determination of the actual (unperturbed) maser frequency. As the operating temperature is decreased to $77K$ and below, the frequency shift increases exponentially.

The frequency shift mechanisms are listed in table 4.2.2. The largest frequency shift in the maser operating at $77K$ is the shift caused by the atoms colliding with the teflon walls of the storage bulb. This frequency shift is given in terms of the phase shift per collision, ϕ_w, multiplied by the mean atom-wall collision frequency, n_w, as [49],

$$\Delta\nu_w = \frac{\phi_w\, n_w}{2\pi} \,. \tag{4.2.6}$$

The phase shift per collision as a function of temperature is shown in figure 4.2.2 [49]. For temperatures below $200K$,

$$\phi_w = -3.9 \times 10^{-6} exp(\frac{260}{T}) = -1.14 \times 10^{-4} \frac{rad}{collision} , \qquad (4.2.7)$$

and the mean collision frequency is a function of the storage bulb size and the mean atomic velocity, $\bar{v}_a$. The frequency shift and fractional frequency shift are therefore,

$$\Delta\nu_w(77K) = -0.557Hz ,$$

$$\frac{\Delta\nu_w}{\nu_o} = -3.9 \times 10^{-10} . \qquad (4.2.8)$$

Cavity pulling also causes a shift in the measured hyperfine frequency. When the hydrogen excites the cavity at a frequency ω_o, and ω_o is not the cavity frequency, then the signal coupled from the cavity will have a measured frequency ω, according to [47]

$$Q_c(\omega_c - \omega) = Q_l(\omega - \omega_o) . \qquad (4.2.9)$$

The frequency offset of the measured hydrogen transition frequency is found by adding $Q_c(\omega - \omega_o)$ to both sides of the above equation which gives,

$$\frac{Q_c}{Q_l + Q_c}(\omega_c - \omega_o) = (\omega - \omega_o) = 2\pi\Delta\nu_p . \qquad (4.2.10)$$

This describes the hyperfine frequency shift in terms of the cavity frequency offset. As the cavity offset is increased, the hyperfine frequency is pulled away from the free space value. This process is called cavity pulling. For the compact maser at $77K$, assume that $Q_l = 5 \times 10^8$, and $Q_c = 3 \times 10^4$, now

$$\Delta\nu_p = \frac{1.5 \times 10^{-5}}{2\pi}(\omega_c - \omega_o) . \qquad (4.2.11)$$

If the cavity offset is $100Hz$, then the cavity pulling is given by,

$$\Delta\nu_p = 1.5 \times 10^{-3} Hz$$

and

$$\frac{\Delta\nu_p}{\nu_o} = 1.1 \times 10^{-12} \,. \tag{4.2.12}$$

The velocity dependent frequency shifts are smaller at $77K$ than found in traditional room temperature masers. Other shifts in the frequency are comparable in both warm and cold masers. In total, the frequency shifts in the compact $77K$ maser will be $1-2$ orders of magnitude greater than in full size warm masers.

Temperature Dependence of Frequency

Some of the frequency shift mechanisms in the hydrogen maser have temperature coefficients that describe the frequency stability of the maser oscillator in terms of the maser's temperature stability. Therefore, the level of temperature control will also limit the level of frequency control achievable for the maser oscillator. The compact maser will have the same sources of frequency perturbations found in conventional masers and possibly some additional frequency shift mechanisms due to the superconducting nature of the resonator.

The frequency shift caused by the collision of the hydrogen atoms with the walls of the storage bulb (wall shift) has a strong temperature dependence at $77K$ [6]. The slope of this frequency shift increases exponentially as the temperature of the bulb is decreased. The sensitivity of the frequency with changing temperature,

Table 4.2.2 Frequency Shifts for the Compact Maser Resonator

Frequency Shift	*Equation*	$\frac{\Delta\nu}{\nu_o}$ *(77K)*	$\frac{\Delta\nu}{\nu_o}$ *(340K)*
Wall Shift	$\frac{\Delta\nu_w}{\nu_o} = \frac{\phi_w n_w}{2\pi\nu_o}$	-3.9×10^{-10}	-1.0×10^{-11}
1st Order Doppler	$\frac{\Delta\nu_w}{\nu_o} = \frac{1}{5\nu_w}\frac{1}{Q_p Q_l}$	6.5×10^{-20}	1.6×10^{-20}
2nd Order Doppler	$\frac{\Delta\nu_D}{\nu_o} = \frac{1}{2}\frac{v_r^2}{c^2}$	-1.3×10^{-11}	-4.0×10^{-11}
Cavity Pulling*	$\frac{\Delta\nu_p}{\nu_o} = \frac{Q_c}{Q_l}\frac{\nu_c-\nu_o}{\nu_o}$	1.1×10^{-12}	2.5×10^{-13}
Zeeman Effect	$\frac{\Delta\nu_z}{\nu_o} = \frac{2750}{\nu_o}H^2$	$< 10^{-13}$	$< 10^{-13}$
Spin Exchange Shift*	$\frac{\Delta\nu_{s.e.}}{\nu_o} = \frac{\lambda n_a v_r}{8\pi\nu_o}(\rho_{1,0} - \rho_{0,0})$	6.4×10^{-12}	2.5×10^{-12}

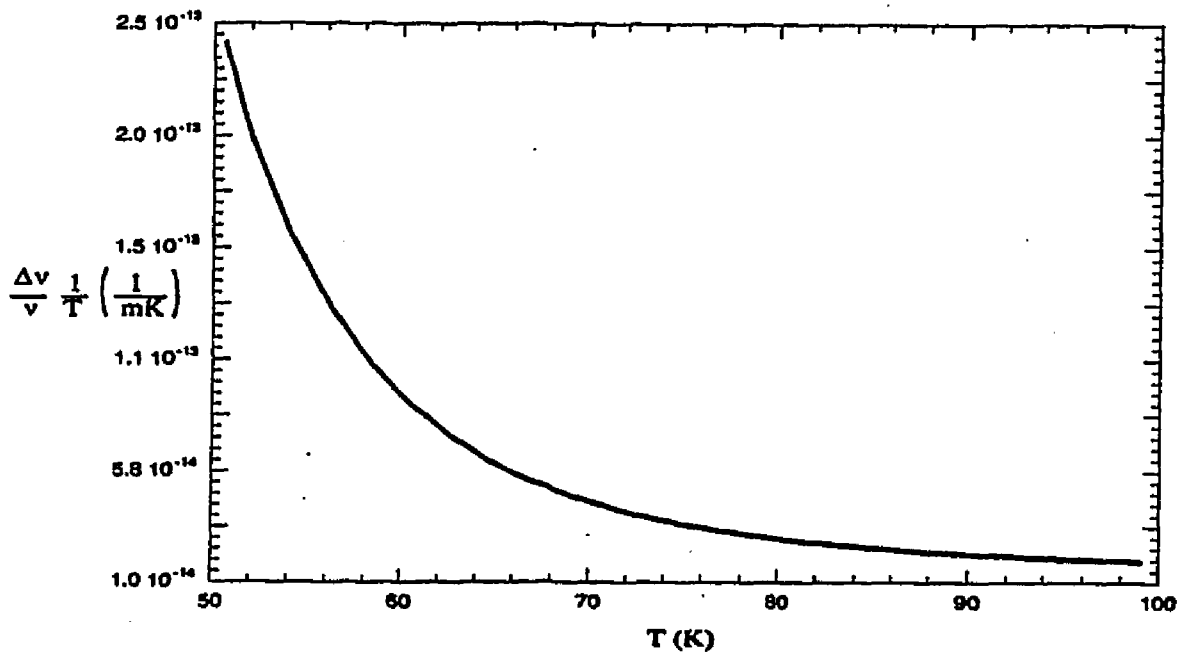

Figure 4.2.3 Fractional frequency shift per milli-Kelvin due to the teflon storage bulb in the superconducting compact maser.

evaluated at $77K$, is given by

$$\frac{\Delta\nu_w}{\Delta T} = \frac{\Delta\phi_w}{\Delta T}\frac{n_w}{2\pi} + \frac{\Delta n_w}{\Delta T}\frac{\phi_w}{2\pi} = -0.040\frac{Hz}{K} , \qquad (4.2.13)$$

or a fractional frequency shift per degree milli-Kelvin of

$$\frac{1}{\nu_o}\frac{\Delta\nu_w}{\Delta T} = 2.81 \times 10^{-14}(mK)^{-1} . \qquad (4.2.14)$$

Shown graphically in figure 4.2.2 is the phase shift as a function of temperature from $50K$ to $350K$. Figure 4.2.3 shows the temperature dependence of the fractional frequency shift as a function of temperature near $77K$, indicating that as the temperature decreases, this sensitivity increases.

Through cavity pulling, the measured maser frequency can be temperature sensitive if Q_l, Q_c or the cavity frequency ω_c are temperature dependent. In the superconducting resonator, the possibility exists that the cavity quality factor and resonant frequency are changing quickly with temperature at $77K$. The sensitivity can be found from considering the differential changes in frequency as a function of temperature using equation (4.2.10),

$$\frac{1}{\nu_o}\frac{\Delta\nu_p}{\Delta T} = \frac{\Delta Q_c}{\Delta T}\frac{1}{Q_l}\frac{(\nu_c-\nu_o)}{\nu_o} - \frac{\Delta Q_l}{\Delta T}\frac{Q_c}{Q_l^2}\frac{(\nu_c-\nu_o)}{\nu_o} + \frac{\Delta\nu_c}{\Delta T}\frac{Q_c}{Q_l}\frac{1}{\nu_o} . \qquad (4.2.15)$$

The last term in equation (4.2.15) describes the maser frequency sensitivity to the changes in the cavity frequency. During the testing of the maser resonator, the resonator typically had a frequency temperature slope of $10^4 Hz/K$, therefore the hyperfine frequency will be temperature sensitive according to,

$$\frac{\Delta\nu}{\Delta T} = 0.30\frac{Hz}{K} ,$$

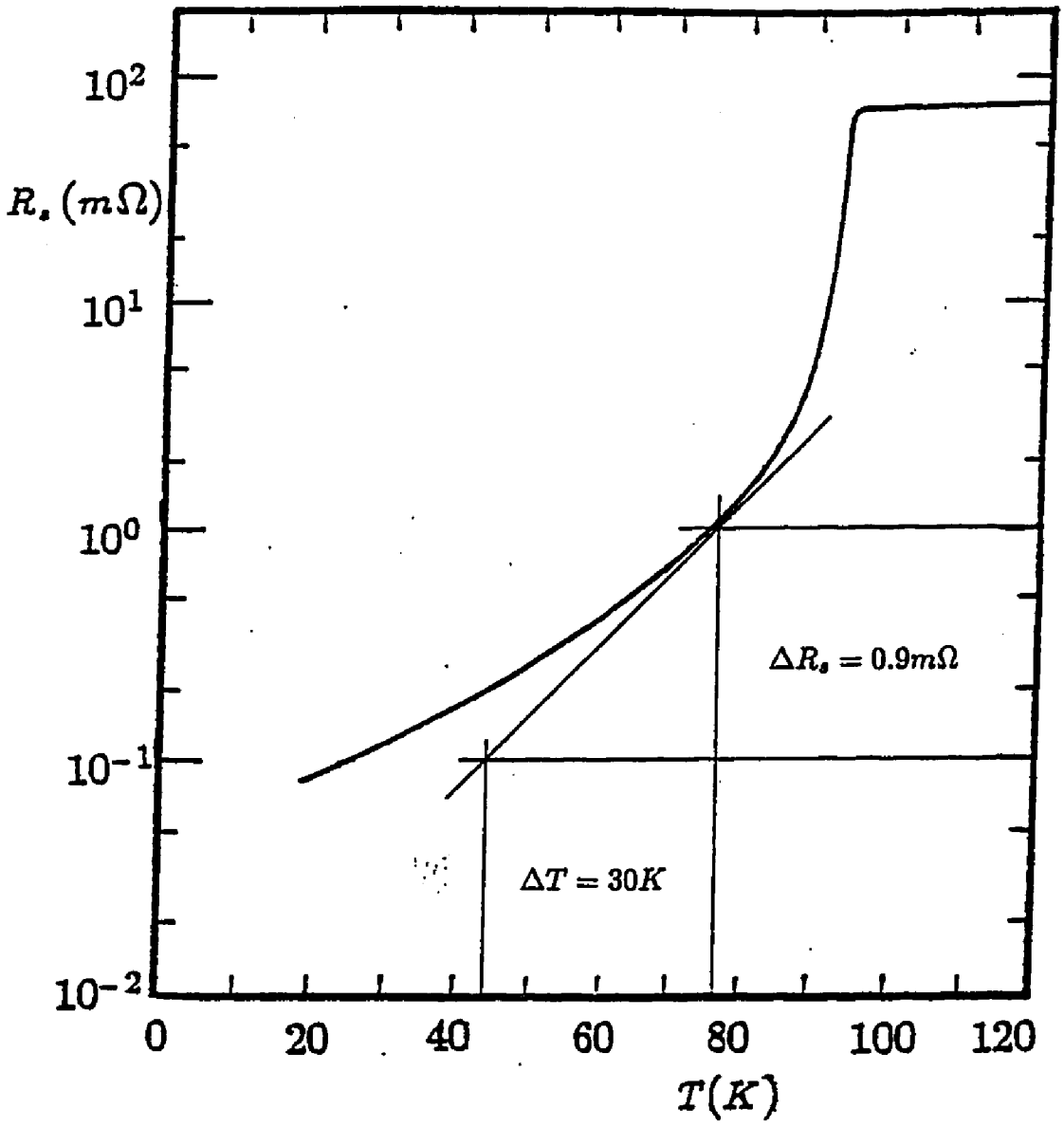

Figure 4.2.4 Typical plot of the YBCO surface resistance versus temperature for the maser resonator electrodes. The slope at $77K$ is $\approx 30\mu\Omega/K$.

$$\frac{1}{\nu_o}\frac{\Delta\nu_c}{\Delta T} = 2.1\times10^{-10}\frac{1}{K} = 2.1\times10^{-13}\frac{1}{mK}\ . \qquad (4.2.16)$$

It should be noted that this term is proportional to the ratio of Q_c and Q_l and as mentioned above, the line Q is relatively lower at $77K$, increaseing the magnitude of this term.

This cavity pulling is also sensitive to the change in cavity Q as a function of temperature. The slope of the superconducting surface resistance (R_s) as a function of temperature (shown in figure 4.2.4)indicates that Q_c changes by 450 per degree. Putting this dependence into the first term yields,

$$\frac{\Delta\nu}{\Delta T} = 4.5\times10^{-7}\frac{(\nu_c-\nu_o)}{\nu_o} \qquad (4.2.17)$$

This temperature dependence is linear with the cavity frequency offset. If the cavity is mistuned by $1000Hz$, then

$$\frac{\Delta\nu}{\Delta T} = 4.5\times10^{-4}\frac{Hz}{K}$$

$$\frac{1}{\nu_o}\frac{\Delta\nu}{\Delta T} = 3.16\times10^{-13}\frac{1}{K} = 3.16\times10^{-16}\frac{1}{mK}\ . \qquad (4.2.18)$$

This is almost 3 orders of magnitude smaller than the cavity frequency temperature coefficient, calculated above.

Finally, the temperature dependence of Q_l is found by finding the differential change of γ_2 versus change in temperature. Again considering that the cavity frequency offset is $1000Hz$,

$$\frac{\Delta\nu}{\Delta T} = 1.16\times10^{-3}\frac{Hz}{K}$$

$$\frac{1}{\nu_o}\frac{\Delta\nu}{\Delta T} = 8.18\times10^{-13}\frac{1}{K} = 8.18\times10^{-16}\frac{1}{mK}\ . \qquad (4.2.19)$$

Table 4.2.3 Requirements to Maintain a Frequency Stability of 1×10^{-15}

Frequency Shift		*Requirements for* $\frac{\Delta\nu}{\nu_o} = 1 \times 10^{-15}$	
		$77K$	$300K$
Wall Shift	$\Delta T =$	$3.6 \times 10^{-5}K$	$6 \times 10^{-3}K$
Cavity Pulling	$\Delta T =$	$4.8 \times 10^{-6}K$	$2 \times 10^{-4}K$
2nd Order Doppler	$\Delta T =$	$2.73 \times 10^{-2}K$	$7 \times 10^{-3}K$
Zeeman Effect ($H = 1mOe$)	$\Delta H =$	$2.5 \times 10^{-7}Oe$	$2.5 \times 10^{-7}Oe$

This term is also small compared with the resonator's temperature frequency sensitivity.

These shift sensitivities are summarized in table 4.2.3. In this table, the greatest tolerable fluctuations of temperature and dc magnetic field are listed as requirements for maintaining a frequency stability of 1×10^{-15}. The sensitivity to temperature fluctuations associated with the cavity pulling is the largest contribution to the total sensitivity. The size of this shift is strongly dependent on the cavity design; the loop-gap structure, as designed, has a large temperature coefficient due to the large expansion coefficient of teflon. This term could become negligible if the teflon support structure was replaced with a material with the same coefficient of expansion as the electrodes themselves. However, the temperature sensitivity of the wall shifts will always remain a problem for liquid nitrogen maser operation. Compared to a maser operating at $300K$, the wall shift temperature coefficient is at least two orders of magnitude larger at $77K$. This increased sensitivity to temperature fluctuations at $77K$ requires that the cavity temperature needs to controlled more carefully to achieve the same stability found in the $300K$ maser.

If great care is taken, the level of temperature control obtainable should be about $0.2 - 0.3mK$ [51]. For the maser considered here, this implies that the frequency will fluctuate, following the uncontrollable temperature fluctuations, corresponding to a level of fractional frequency fluctuations of $\approx 2 \times 10^{-14}$. For comparison, it is reported that for masers operating above $340K$ the cavity temperature is assumed to be constant to $2 \times 10^{-5}/°C$ [20]. For this type of maser, the values for

the measured coefficients range from $1 \times 10^{-17}/°C$ [53] to $< 5 \times 10^{-18}/°C$ [66]. Assuming that the $77K$ maser obtain the same level of temperature control reported above for the $340K$ masers, the best frequency stability achievable would be a few parts in 10^{-15}.

Other Sensitivities

The effects of aging (or decay) of the superconducting properties as a function of time would cause frequency drift of the oscillator. Aging is a problem in masers currently operating and is manifested in creep of the microwave cavity dimensions, degradation of the electronic components, and aging of the shield's magnetic domains [52]. Perhaps the $77K$ operating environment would slow some of the aging processes but the additional aging of the superconducting properties must be considered as a possibility. The HTSSE project is designed to answer the question of aging in the possibly damaging environment of space. This question will be answered in the future, but for now, assume the aging of the YBCO–through radiation damage, oxygen loss, physical damage from vibrations, etc.– is found to be $\Delta Q_C = 1/day$. Using the cavity pulling equation,

$$\frac{1}{\nu_o}\frac{\Delta\nu_p}{\Delta t} = \frac{\Delta Q_c}{\Delta t}\frac{1}{Q_l}\frac{(\nu_c - \nu_o)}{\nu_o} \ . \tag{4.2.19}$$

This change of the cavity quality factor will 'un-pull' the measured maser frequency and therefore be measured as a drift in the oscillator frequency given by,

$$\frac{1}{\nu_o}\frac{\Delta\nu_p}{\Delta t} = 1.4 \times 10^{-16} day^{-1} \ , \tag{4.2.20}$$

for every $100Hz$ that the cavity is offset from the hyperfine frequency. For comparison, it is reported that active masers at $340K$ have a frequency drift less than 10^{-14} per day [53].

The frequency of the maser is also a function of the applied dc magnetic field. The frequency shift caused by this field is given in table 4.2.2

$$\frac{\Delta\nu_z}{\nu_o} = \frac{2750}{\nu_o}H^2 \ .$$

The sensitivity to the magnetic field is

$$\frac{1}{\nu_o}\frac{\Delta\nu_z}{\Delta H} = \frac{5500}{\nu_o}H \ . \tag{4.2.21}$$

Assuming that the applied field is $1mOe$, and the this field fluctuates by 1%, then the sensitivity is

$$\frac{1}{\nu_o}\frac{\Delta\nu_z}{\Delta H} = 3.87 \times 10^{-9}(mOe)^{-1} \ .$$

This requires a very stable dc field source, the requirements of which are shown in table 4.2.3.

These fluctuations of the frequency will be altered if the rf shield-can is made to be superconducting. The YBCO superconductor has been shown to shield/trap magnetic flux at temperatures below T_c [54]. The field levels required for the hydrogen maser are relatively low, about $0.5mG$. For higher field levels, more than $20G$, a time dependent decay of the shielding currents has been measured, where the trapped fields decay by about 3% after 10^3 seconds. Our measurements of shielding currents in a closed shielding structure have shown no time dependence within experimental resolution ($1mG$) for times up to 10^6 seconds. As the time constant of

the trapped flux becomes longer, the field fluctuations will cause frequency fluctuations only for times on the order of the time constant. Therefore, a compact maser with a superconducting shield-can would still need a dc magnetic field source but the time constant of the YBCO could damp frequency fluctuations for up to 10^6 seconds.

Summary

The superconducting compact maser is expected to have larger frequency shifts, shorter transition lifetimes and greater sensitivity to temperature changes than a typical active maser. This is a consequence of the inner surface of the storage bulb having a longer interaction time with the colliding hydrogen atoms. The net effect of the changes in the relaxation rates and frequency shifts is that the maser's frequency stability is more strongly coupled to the systematic fluctuations of the oscillator. In such a design, the temperature control presents a challenge. However, the superconducting shield-can could stabilize the resonator against magnetically induced frequency shifts.

CHAPTER 5

5.1 The Loop-gap Resonator

The loop-gap resonator is a type of magnetron resonator whose origins extend back at least to 1935 [55]. The applications and characteristics of this resonator design have been discussed in many (at least 15) publications over the past decade. Applications for this design are found in nuclear magnetic resonance, electron spin resonance, radar, and maser spectroscopy at frequencies from 200MHz to 11GHz. The compact hydrogen maser resonator using the lumped element loop-gap design was originally suggested by H. E. Peters [3]. Descriptions of the electric and magnetic fields in the loop-gap have been described by many authors. From these references, one finds various empirical relations for the frequency and quality factor as a function of resonator geometry. However, no analytic solution for this resonant mode exists. All of these articles mentioned above overlook the most striking feature of the rf magnetic field profile; specifically, the greatly enhanced magnetic field density at the edges of the electrodes. It is this field enhancement that dominates the losses in the superconducting resonator and leads to errors in the measured R_s values for the YBCO electrodes. Moreover, a (maser) resonator's filling factor, defined as the ratio of stimulating field energy in the maser interaction region to the total energy,

$$\eta' = \frac{\langle H_z \rangle^2_{bulb}}{\langle H^2 \rangle_{cavity}} , \tag{5.1.1}$$

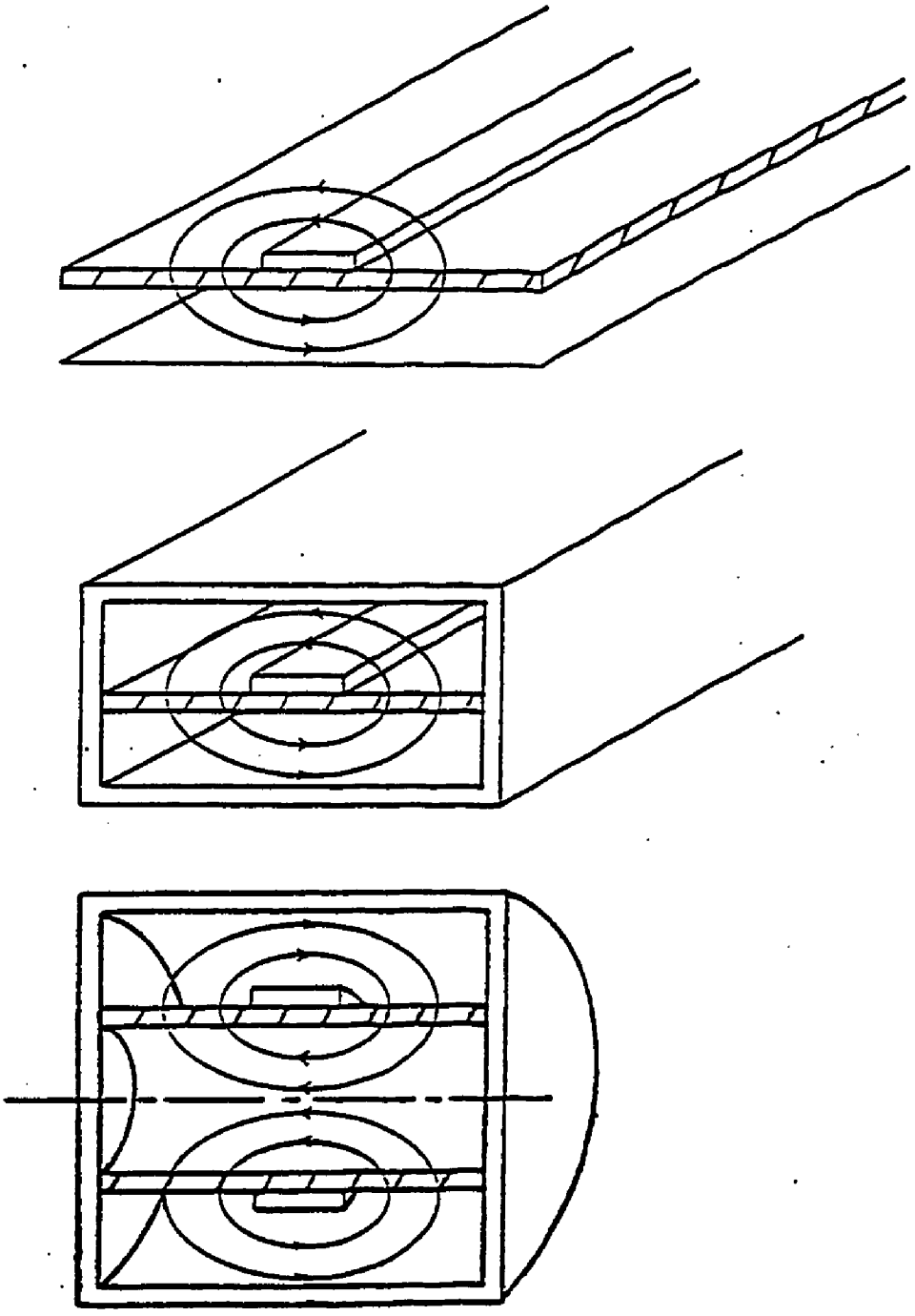

Figure 5.1.1 Diagram of the microstrip, shielded stripline, and the maser resonator illustrating the analogy between the three stuctures. The direction of the rf magnetic fields are shown at the cross section.

cannot be calculated properly without first accounting for this effect.

A general description of the resonant mode has been given in the other papers [3,56,57,58]. The magnetic nature of the mode is qualitatively similar to fields of a solenoid which is in an oscillating circuit. The currents flow azimuthally (solenoidally) around the electrodes, and consequently, on the surface of the rf shield-can. However, it should be noted, that although the current distribution on the surface of the electrodes is solenoidal, one can infer from the high frequency boundary conditions that the classical picture of a solenoid is an inadequate approximation. Since a solenoid has flux lines that can close *through* its body; while the boundary conditions in the loop-gap, in contrast, will force all flux lines to close around the ends of the conductor and not through the electrode surfaces, which results in substantially different distributions of current.

This loop-gap resonator can be best understood by analogy with the shielded stripline. Such a device consists of an infinitely long coaxial conductor of rectangular cross-section. Another related problem is the microstrip geometry where three sides of the shielded stripline are at distances very large (infinite) compared to the separation between the strip conductor and the remaining conducting plane. These three models, the loop-gap, the microstrip and the shielded stripline, may be considered as closely related problems as shown in figure 5.1.1. The coordinate system for these descriptions is one where the $\hat{z}$ is parallel to the ground plane and perpendicular to the direction of current flow, which is along the strip. For the cylindrical loop-gap resonator, this becomes the typical cylindrical coordinate

system. The coordinate system for the striplines is rectangular but for consistancy, the logitudinal direction is labled as the $\hat{\phi}$ axis.

The currents and the fields for these three similar structures can be described as TEM. The analogy between the shielded stripline and the loop-gap resonator is visualized by a transformation of the striplines longitudinal axis, centered on the inner conductor, to the circle that describes the electrodes circumference. Finally, the radius of what has become the inner shield wall is reduced to zero. In the cross-section of the loop-gap, in the r, z plane ($0 < r < R$), the profile of conducting surfaces and the boundary conditions are the same as the shielded stripline. Standing waves on the stripline structures can be compared with the resonant mode in the loop-gap resonator. At a specific point along the stripline, when the electric field is zero across the r, z plane, the rf magnetic fields of the stripline will qualitatively map to the resonant magnetic fields of the loop-gap cavity. For the range of frequencies considered, the fields are TEM with respect to the currents flowing in the loop-gap $\hat{\phi}$ direction and propagating azimuthally between the electrodes and the rf shield.

The motivation for considering these other geometries is that an understanding of the simpler shielded stripline will lend insight to the loop-gap problem. As mentioned above, all of the geometries in this class of problems (microstrip, shielded stripline, loop-gap,...) provide current distributions that are not constant along the strip or loop-gap electrodes width. Specifically, the current density increases sharply at the conductor edges [59,60,61]. This is true so long as the fields are considered

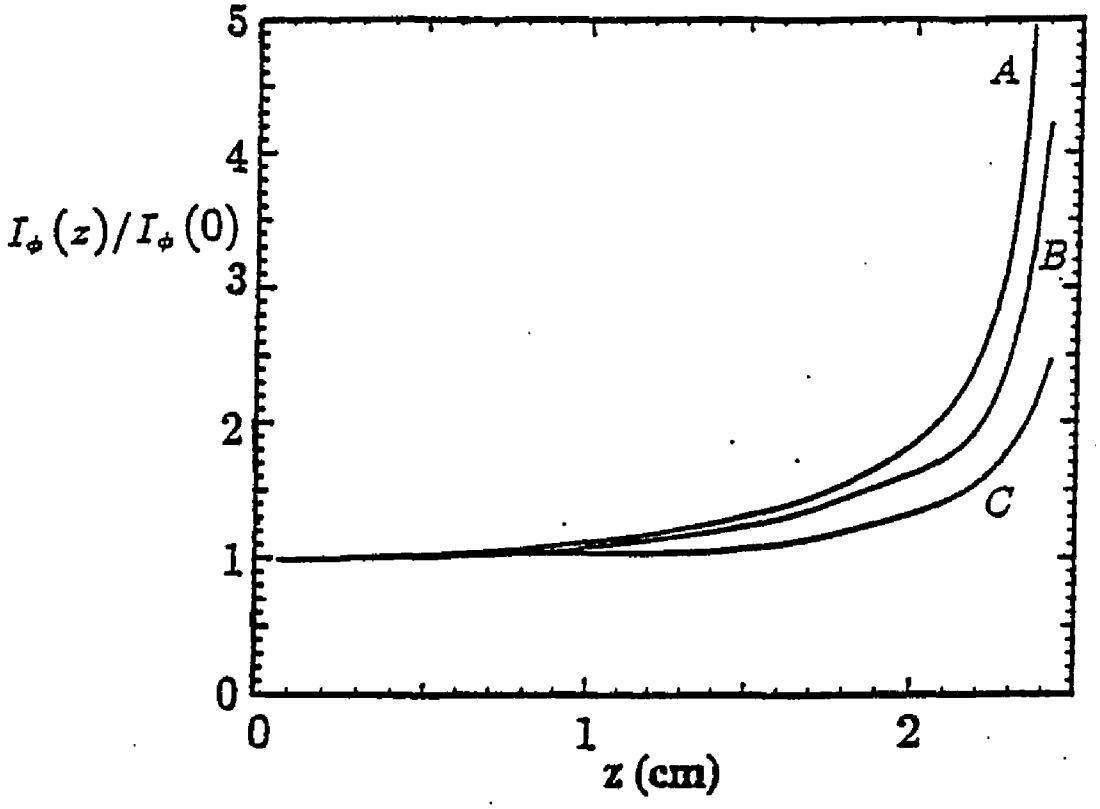

Figure 5.1.2 Distribution of the currents calculated along the $\hat{z}$ axis using three different methods: (A) conformal mapping, (B) Green's function, (C) MAFIA finite element calculation.

to be in the "quasi-static" limit; the fields are TEM and the dimensions of the strip conductor are small compared to the wavelength [59]. In this quasi-static limit, the current distribution is related to the distribution of excess static charge placed on the isolated strip conductor. This relation for the currents on the microstrip is

$$I_\phi(z) = v\sigma(z) \ , \tag{5.1.2}$$

where v is the phase velocity and $\sigma(z)$ is the static charge distribution. The solution for an infinitely thin isolated conducting strip above a ground plane was derived by Maxwell [62]. He found that by using a conformal mapping technique, the static charge distribution on an infinitely thin conducting sheet above a ground plane is given by,

$$\sigma(z) = \frac{\sigma_o}{\pi\sqrt{1-(2z/l)^2}} \ , \tag{5.1.3}$$

where l is the half of the width of the strip conductor ($l = L/2$) and z is the point along the strip where the charge is evaluated. The coordinate system is the same cylindrical system used for figure 5.1.1. In this solution the current distribution is infinite but integrable at the conductor edges.

A more realistic solution is found by using a Green's function method [60]. The Green's function and conformal mapping solutions are plotted in figure 5.1.2.The general feature of both of these solutions is the uniform current distribution in the center of the strip, and a sharp increase at the edges. For the shielded stripline, the edge currents on the strip are further increased by the existence of images in the shield wall [59]. Again, this is analogous to electrostatic image problems. Recently,

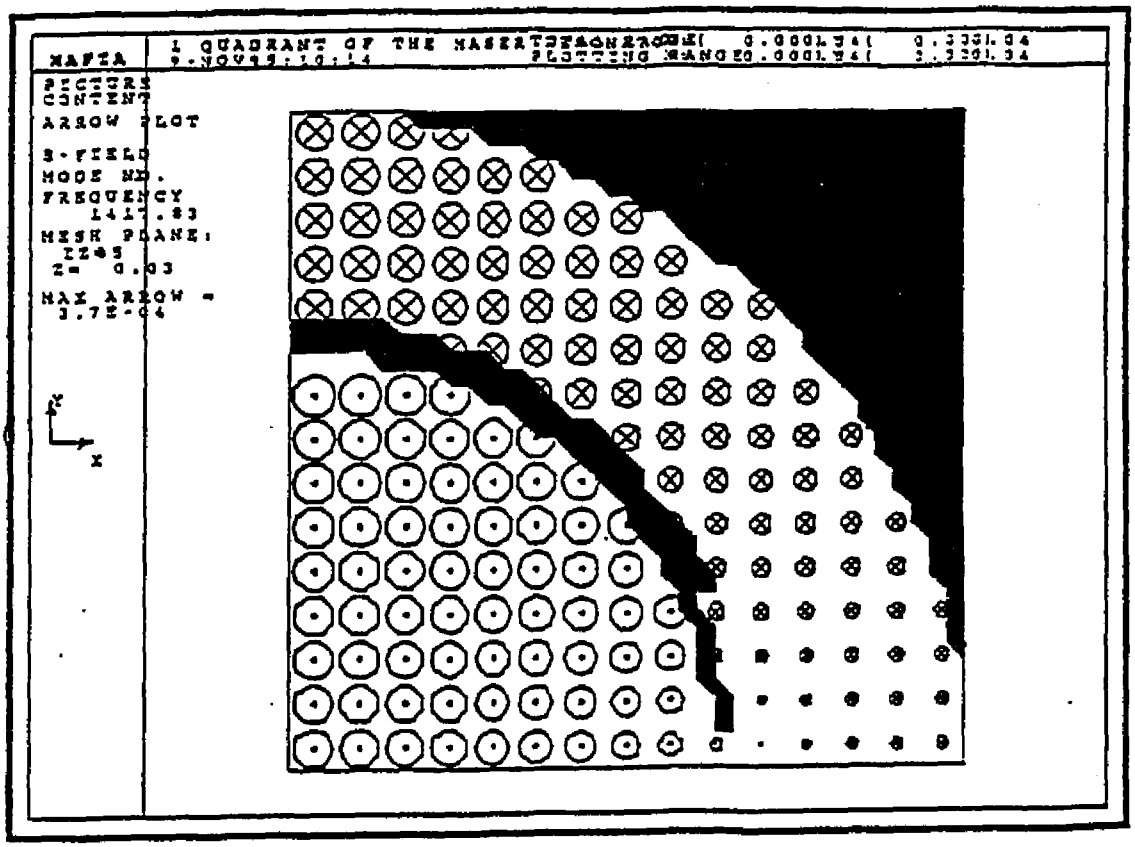

Figure 5.1.3 Distribution of axially directed rf magnetic field in one quadrant across the center of the cavity. The size of the circles gives the relative magnitude of the field. The gap between the electrodes is along the x axis.

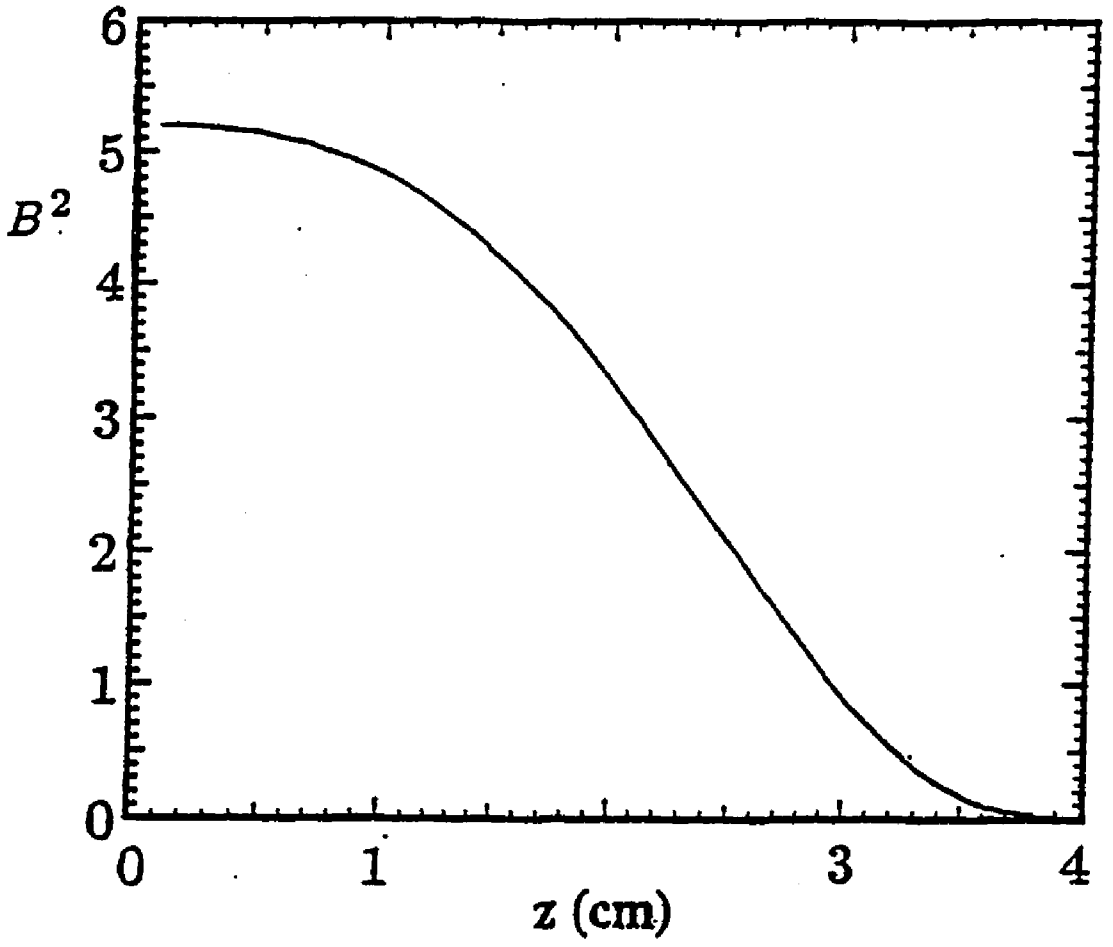

Figure 5.1.4 Profile of the magnetic field energy along the $\hat{z}$ axis where $r = 0$ showing the solenoidal field profile within the interaction region of the cavity.

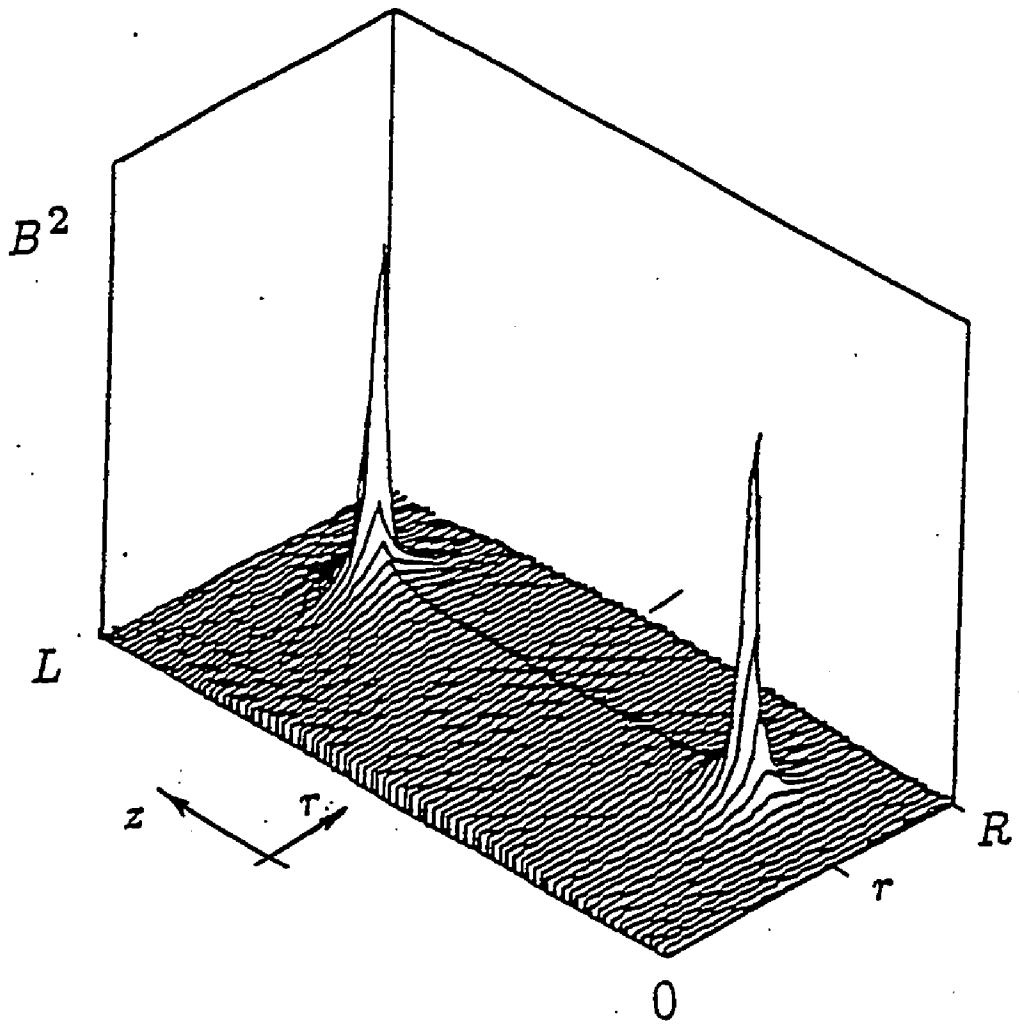

Figure 5.1.5 Plot of the field energy in the $r - z$ plane. The peaks in the energy distribution are located at the upper and lower edges of the electrodes. The relative magnitude of the fields in figure 5.1.4 are nearly too small to be seen on the scale appropriate to the peak field values.

an exact solution for the shielded stripline problem was published demonstrating that this electrodynamics problem is contemporary and non-trivial [63].

Unfortunately, the exact solution for the shielded stripline does not obviously transform to the cylindrical geometry of the loop-gap. Instead, a three dimensional finite difference code, MAFIA, was used to investigate the fields [67]. Plots of the magnetic and electric fields from MAFIA confirm the qualitative field descriptions reported in other loop-gap papers. As expected, the electric field is concentrated in the gap regions and the magnetic fields are generally in the axial direction within the interaction region of the maser cavity. Figure 5.1.3 shows the distribution of axially directed magnetic field in one quadrant across the center of the cavity. The field is described by arrowheads ($\odot$) and arrowtails ($\otimes$) to indicate the direction, and the relative magnitude is given by the size of the circles normalized to the largest field in the quadrant. Figure 5.1.4 is a plot of the rf magnetic field magnitude in the center of the cavity ($r = 0$) from $z = 0$ up to the shield-can endplate, where $z = L/2$. From field profile measurements, it is found that this axial profile is very similar to the static fields of a dc solenoid and its image, so that the boundary conditions are satisfied at the endplates. However, in the regions near the electrodes, differences between the solenoid model and the loop-gap arise from the high frequency boundary conditions on the electrode surfaces. The current is distributed to satisfy these boundary conditions as shown in figure 5.1.2. Figure 5.1.5 shows the profile of magnetic field energy across the r, z plane, where $0 < r \leq R$. The enhancement of the magnetic field energy at the edges of the electrodes is as expected, and is in

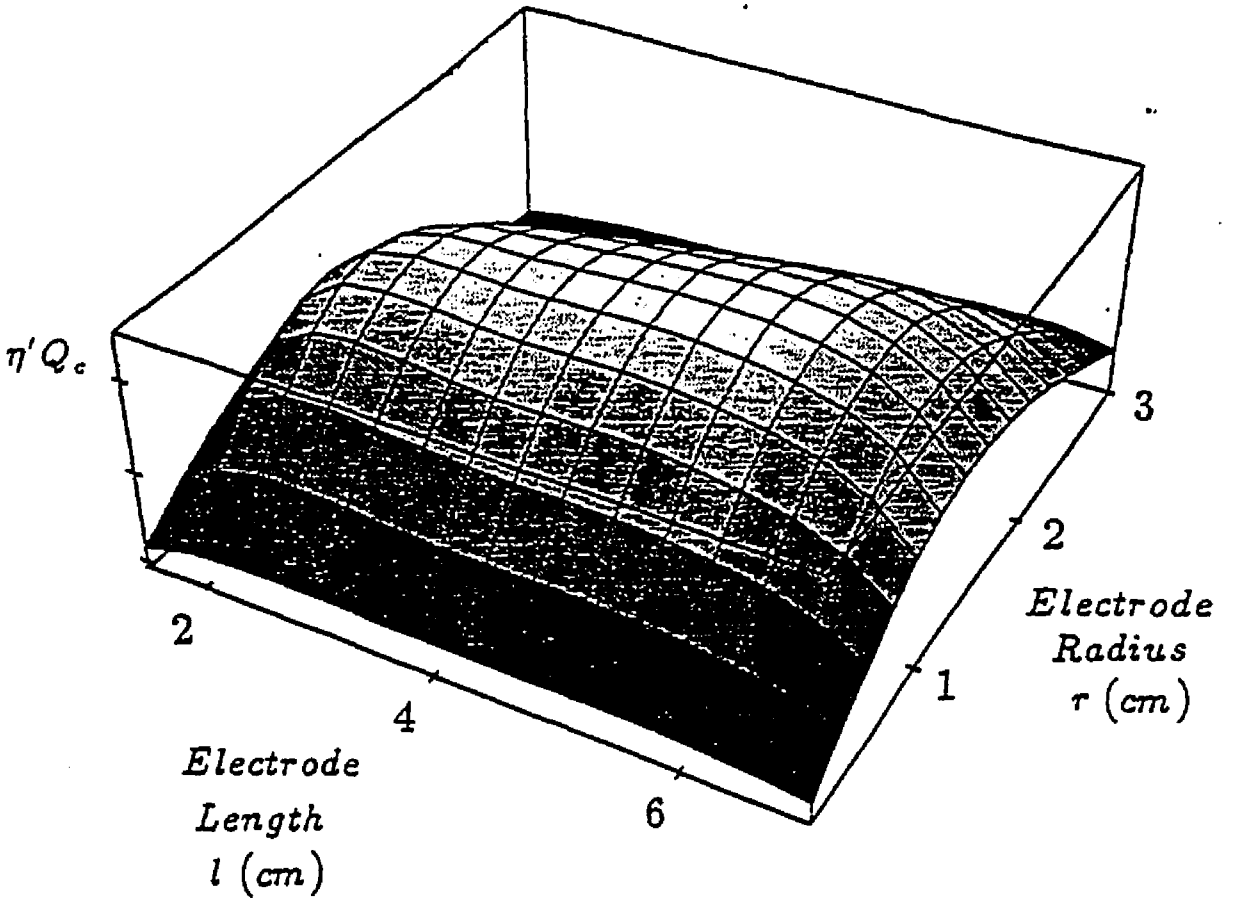

Figure 5.1.6 Plot showing the product of $\eta' Q_c$ as a funtion of the electrode length and radius calculated for a give shield-can geometry.

agreement with the stripline analogy.

The significance of this magnetic field energy distribution, and the effects this will have on the performance of a maser, is that the filling factor and the distribution of power losses in the resonator cannot be accurately calculated without knowing the fields. If the magnetic field is constant in the interaction region then the filling factor is approximated as [3],

$$\eta' = \left(\frac{r_b}{r}\right)^2 \left[1 + \frac{\left(\frac{L}{l}\left(\frac{R}{r}\right)^2 - 1\right)}{\left(\left(\frac{R}{r}\right)^2 - 1\right)^2}\right]^{-1} , \tag{5.1.4}$$

where r_b is the bulb inner radius. From figure 5.1.4, it is clear that considering the fields to be uniform causes an over estimation of $\langle H_z \rangle^2_{bulb}$. When the total field energy is summed over the volume of the cavity, the concentration of the fields at the edges will lead to an underestimation of $\langle H^2 \rangle_{cavity}$. Therefore, the approximation that the fields are generally uniform leads to an overestimation of η'. For example, the filling factor for the cavity design shown in figure 2.2.4 is 0.30, compared to the uniform field approximation value (equation (5.1.4)), $\eta' = 0.40$ when $r_b = 2.2cm$.

The current distribution on the electrodes and on the surfaces of the shield-can will vary in the same qualitative manner as in the shielded stripline. As the edges of the electrode conductor are moved closer to the shield surfaces, the currents will increase in this region due to the image currents on the shielding surfaces [60]. This change in the current distribution increases the local field energy and thereby reducing the fraction of total magnetic energy in the interaction region. The effect that this has on the Q_c and η' is shown in figure 5.1.6. This graph shows the product of η' and Q_c as a function of the electrode radius and length for a given

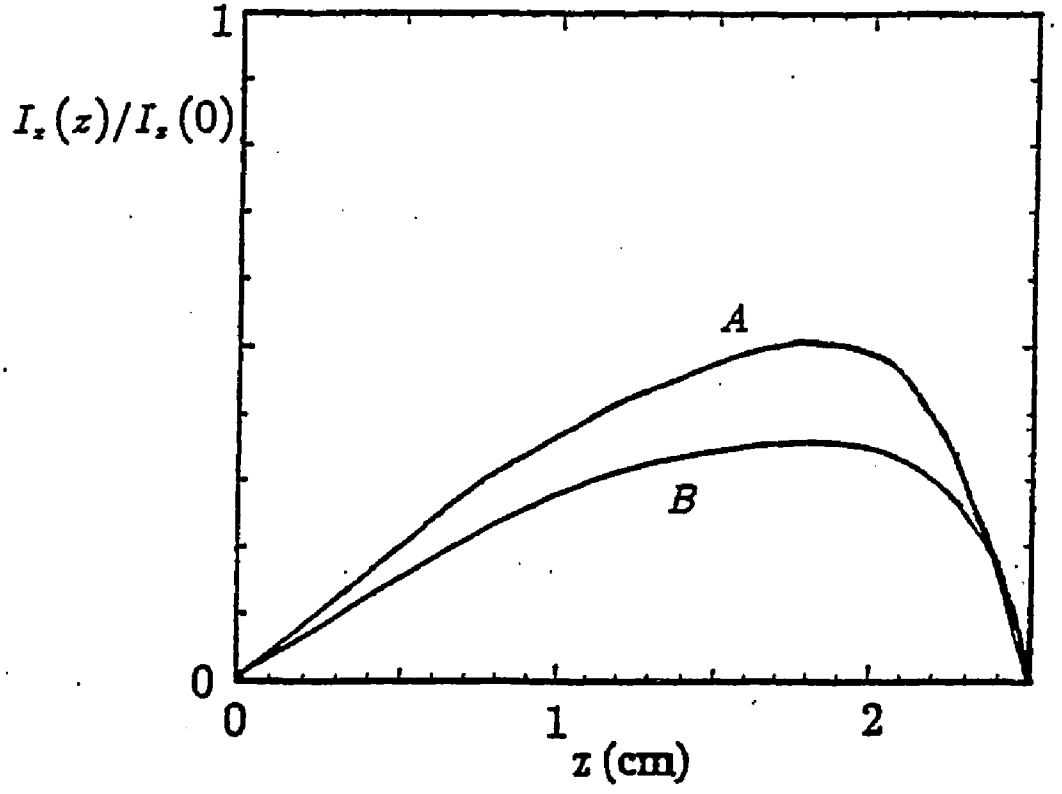

Figure 5.1.7 The component of the rf currents on the electrodes that are perpendicular to the direction of the TEM currents. The upper curve (A) is from the MAFIA calculation and the lower curve (B) is from the relationship given in reference [59].

shield-can size. The maximum for this product is found in the region where the electrode radius is about half of the shield-can radius and the electrode length is about 80% of the shield-can length.

Measuring the Q_c, and therefore surface resistance in the YBCO superconducting resonator, is complicated by this current distribution on the electrodes. It has been shown that the R_s of polycrystalline YBCO is dependent on the magnitude of the rf magnetic fields at the surface [64]. The expected behavior is that the R_s remains fairly constant with increasing surface field up to a critical value, then R_s will increase sharply with further increases in the field. Figure 3.2.4 indicates that for a broad range of rf power levels, some part of the superconducting surface in the loop-gap resonator is experiencing field values beyond this critical point, even though the input power to the cavity is as low as $-30dbm$ (the coupling Q was $> 10^6$). This effect makes the characterization of the resonator surface difficult but should not be a problem at the picowatt power levels expected in an oscillating maser.

Previously, an assumption has been made that the frequency is sufficiently low so the wavelength is much larger than the dimensions of the strip and the fields are perfectly TEM. The effect of operating at a frequency where the wavelength is on the order of the strips dimensions is that a perpendicular component to the $I_z(z)$ vcurrent distribution, $I_\phi(z)$, is also present along the strip. It has been suggested that the form of this component will be similar to [59],

$$I_z(z) = \begin{cases} I_{z0} \sin\left(\frac{\pi z}{0.7l}\right), & |z| \leq 0.8\frac{l}{2}; \\ I_{z0} \cos\left(\frac{\pi z}{0.2l}\right), & 0.8\frac{l}{2} < |z| \leq \frac{l}{2}. \end{cases} \tag{5.1.5}$$

The magnitude of I_{z0} is proportional to the normalized strip width l/λ, where λ is the wavelength corresponding to the resonant frequency. When $l/\lambda < 0.1$, the average current amplitude I_{z0} across one half of the strip width is less than ten percent of the average value of the current amplitude,$I_\phi(z = 0)$. For the cavity considered here, the condition that $l/\lambda < 0.1$ is not satisfied. Specifically, for an operating frequency of $1.42GHz$ (corresponding to a $21cm$ wavelength), and an electrode length of $5cm$, this cavity is not obviously operating within the quasi-static limit. This would imply that in the maser resonator, the currents no longer flow only azimuthally around the electrodes but that there is also a component to the flow in the longitudinal direction. Shown in figure 5.1.7 is a MAFIA plot of $I_z(z) \propto B_\phi$ at the surface of the conductor compared with the function in equation (5.1.5). The shape of this curve is similar to that expected from a stripline where $l \not< 0.1\lambda$. However, the transverse fields from the I_z current components, as found in the numerical analysis, are much smaller ($<$ 0.01%) than the magnetic field component parallel to the $\hat{z}$ axis over most of the interaction region, therefore this will not be a serious perturbation to the maser oscillation. However, if the overall size of the loop-gap cavity increases, this effect also increases and, at some point, would become significant.

Using the stripline analogy to understand the nature of the loop-gap resonant mode has proven very useful. Without this interpretation, the experimental results in figure 3.2.4 could not otherwise be explained. The solution to the loop-gap resonator current distribution is also a valid solution to other boundary value prob-

lems that otherwise are very difficult. For example, the high frequency boundary conditions on the surface of the electrodes are the same as the dc magnetic superconducting boundary conditions (Meissner state) in shielding problems when the shield-can is large compared to the electrodes. Therefore, the current distribution from the loop-gap resonant solution is essentially the solution to a superconducting cylinder in a longitudinally applied magnetic field; the currents distributions on the electrodes are the same as the current distributions on the superconducting cylinder described above.

For the evaluation of the compact maser, the most important result from the numerical analysis is that shown in figure 5.1.6: the relationship of the cavity Q and filling factor product as a function of cavity dimensions. With this relationship, the cavity design can be optimized to achieve the greatest stability.

5.2 Optimization of the Loop-gap Design

In order to find the loop-gap maser resonator design that will minimize the Allan deviation for integration times between 100 and 10000 seconds, the $\sigma_l(\tau)$ due to thermal noise within the atomic linewidth must be minimized. The goal is to express $\sigma_l(\tau)$ in terms of geometric variables like the resonator length and diameter as well as the cavity quality factor, Q_c. The bulb relaxation rate γ_b, will be taken as an implicit variable, and thus given fixed values. The spin exchange relaxation rate, $\gamma_{s.e.}$, can be removed from the expressions for the deviation because there is a minimum in the deviation with respect to $\gamma_{s.e.}$. With these simplifications and the relationship in figure 5.1.6, the filling factor and the quality factor as a function of the cavity geometry, the deviation can be minimized in terms of the cavity dimensions.

The thermal frequency noise term of the Allan deviation from equation 1.3.15 is

$$\sigma_l(\tau) = \frac{1}{Q_l}\sqrt{\frac{kT}{2P\tau}}\,. \tag{5.2.1}$$

Where Q_l is the atomic line quality factor, k is Boltzmann's constant, T is the temperature inside the cavity, and P is the power delivered by the atomic beam to the cavity. When $\sigma_l(\tau)$ is plotted on a logarithmic scale, the function is a line with slope of $-1/2$. Therefore, minimizing at $\sigma_l(\tau = 1sec)$ will describe the deviation for τ values up to where other random or systematic deviations dominate; $\tau \sim 10000\ sec.$

Equation (5.2.1) can be written as

$$\sigma_l(\tau) = \sqrt{\frac{kT}{2\pi^2\nu_o^2}}\sqrt{\frac{1}{PT_2^2}}\tau^{1/2} \tag{5.2.2}$$

when $Q_l = \pi\nu_o T_2$. The first term under the radical is a constant when evaluated at the operation temperature of $77K$ and for the operating frequency, ν_o, equal to $1.42GHz$. Therefore it is only necessary to maximize the product PT_2^2 for the thermal noise deviation to be minimized. Separating out terms that are constant for changes in cavity geometry and defining these terms as constants A and B, we have

$$\begin{aligned} PT_2^2 &= BV_b\left(\frac{\gamma_1}{\gamma_2}\right)\left(A\frac{\gamma_b\gamma_{1s.e.}}{\gamma_1\gamma_2} - \frac{1}{\eta' Q}\right) \\ A &= \frac{\mu_o\mu_B^2 C_b}{\hbar\sigma v_r} \\ B &= \frac{\hbar^2\pi\nu_o}{\mu_o\mu_B^2} \end{aligned} \tag{5.2.3}$$

The total relaxation rates are defined as

$$\begin{aligned} \gamma_1 &= \gamma_b + \gamma_{1w} + \gamma_{1s.e.} \\ \gamma_2 &= \gamma_b + \gamma_{2w} + \gamma_{2s.e.}. \end{aligned} \tag{5.2.4}$$

In the above expressions, γ_1 and γ_2 are the total longitudinal and transverse relaxation rates, respectively. $\gamma_{1s.e.}$ is the spin exchange relaxation rate. As described in reference [47]:

$$\begin{aligned} \gamma_{1s.e.} &= 2\gamma_{2s.e.} \\ &= n\sigma\bar{v}_r = n\sigma 4\left(\frac{kT}{\pi m}\right)^{1/2}. \end{aligned} \tag{5.2.5}$$

Here, σ is the spin exchange cross section, $\bar{v}_r$ is the average relative atomic velocity, and n is hydrogen density given by

$$n = \frac{I_{tot}T_b}{V_b}. \tag{5.2.6}$$

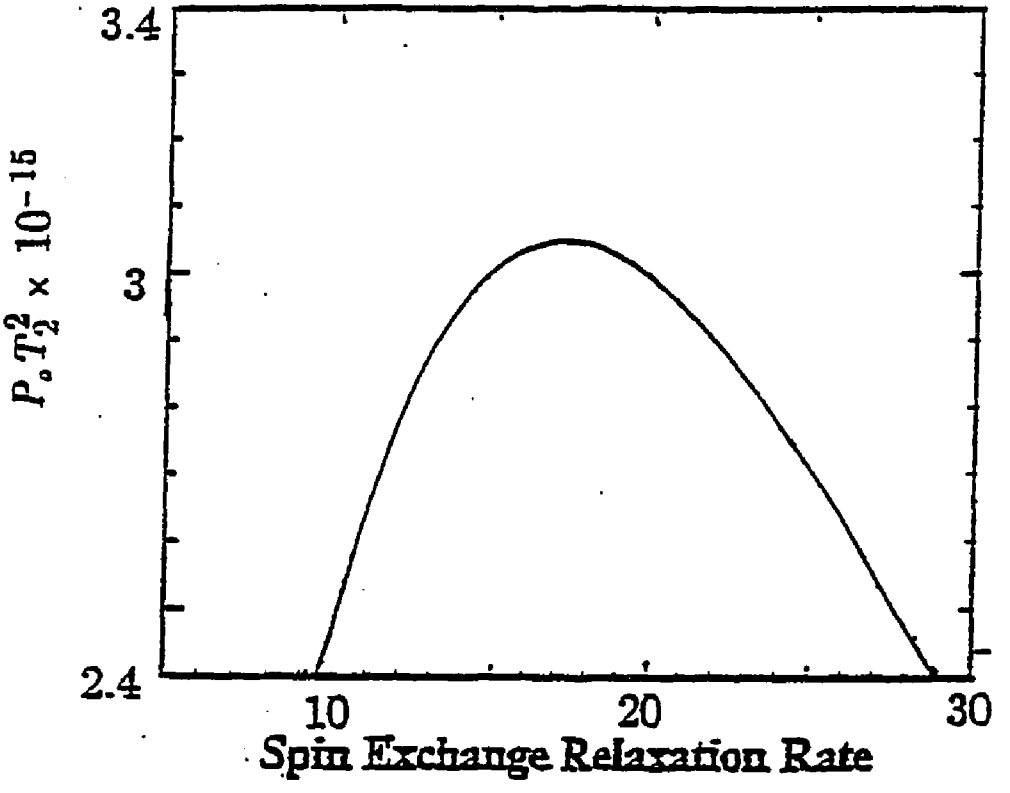

Figure 5.2.1 The product of PT_2^2 as a function of $\gamma_{1s.e.}$ which is proportional to the density of atoms in the storage bulb.

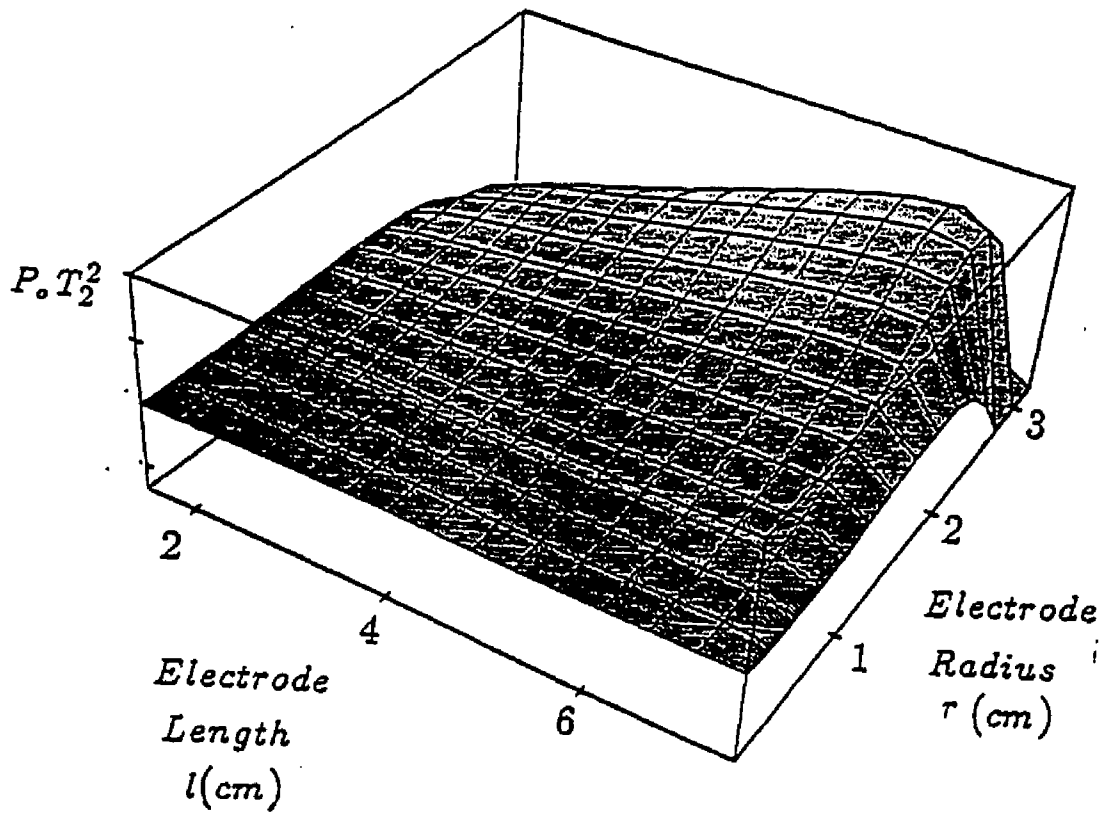

Figure 5.2.2 The product of PT_2^2 evaluated at the optimum atomic density is shown as a function of the electrode length and radius for the shield can shown in figure 2.2.4.

The relaxation rates, γ_{1w} and γ_{2w} describe the loss rate of the desired atomic state and loss of phase coherence between the atoms due to collision with the sides of the storage container. For this atom-wall interaction, p_{1w} is defined as the transverse relaxation probability per collision and τ_c is the average time between atomic wall collisions [6]. At $77K$ and for A_b defined as the surface area of the storage container,

$$\gamma_{1w} = \frac{p_{1w}}{\tau_c} \approx \frac{4}{3}\gamma_{2w}$$

$$p_{1w} = 7.3 \times 10^{-6} exp\left(\frac{230}{T}\right) = 1.45 \times 10^{-4} .$$

$$\frac{1}{\tau_c} = \frac{mean\ atomic\ velocity}{mean\ free\ path} = \sqrt{\frac{8kT}{\pi m}}\frac{A_b}{4V_b}. \qquad (5.2.7)$$

Since the spin exchange relaxation rate is proportional to the hydrogen density in the bulb, we can solve for the condition of optimal density. A plot of PT_2^2 as a function of $\gamma_{1s.e.}$ is shown in figure 5.2.1. By setting the derivative of PT_2^2 with respect to $\gamma_{1s.e.}$ equal to zero and solving for $\gamma_{1s.e.}$, we determine the condition where PT_2^2 is always evaluated at the optimal beam current. This condition on $\gamma_{1s.e.}$ is in terms of the other parameters and is substituted back into equation (5.2.3). This ensures that the product of PT_2^2 is always evaluated at the optimal hydrogen density within the bulb. It is found that $\gamma_{1s.e.}$ for optimal stability is given by

$$\gamma_{1s.e.} = \frac{2(\gamma_{2w} + \gamma_b)(2\gamma_{2w} - \gamma_{1w} + \gamma_b - 2A\gamma_b\eta' Q_c)}{\gamma_{1w} - 2\gamma_{2w} - \gamma_b - 2A\gamma_b\eta' Q_c} \qquad (5.2.8)$$

We consider that the bulb relaxation rate can be adjusted by changing the collimator tube length. All the other variables are dependent on the particular

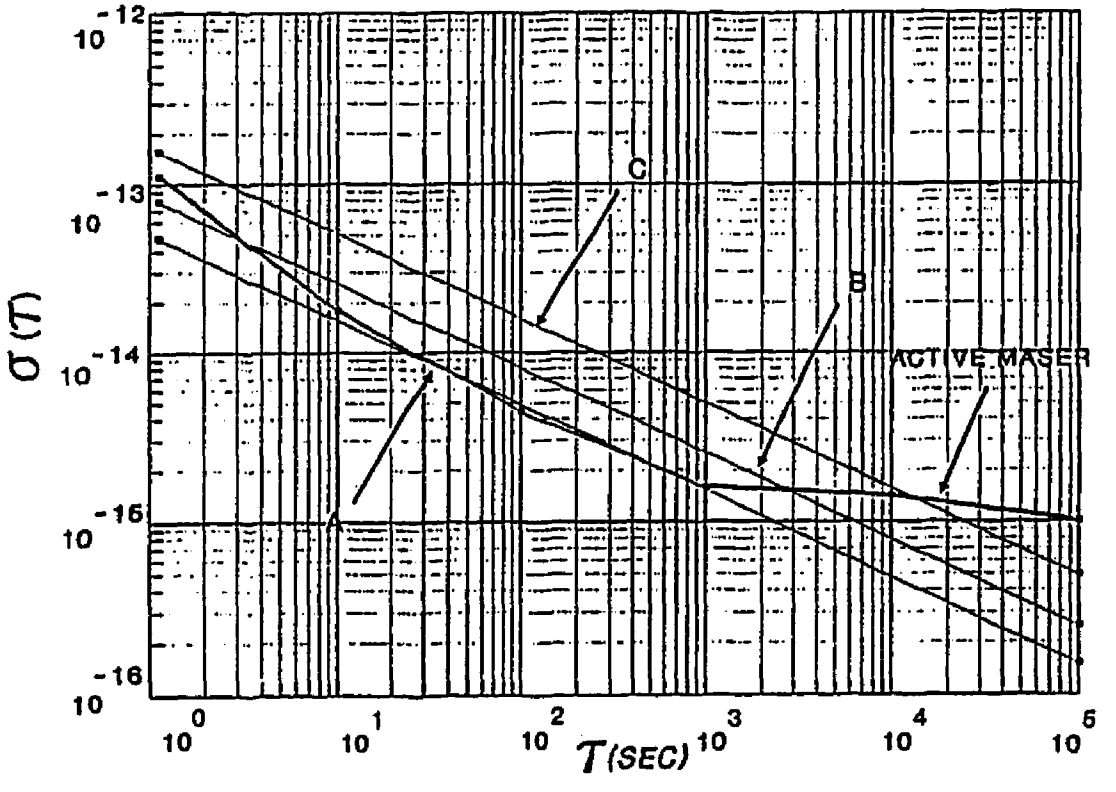

Figure 5.2.3 The Allan deviation as a function of the integration time for three different cavity geometries: (A) optimal design according to the electrode geometry with maximum PT_2^2, (B) the cavity shown in figure 2.2.4, (C) a cavity designed for maximum $\eta' Q_c$.

cavity geometry, such as the filling factor, the bulb volume, the atomic collision rate with the walls, and the quality factor, Q_c. Since no analytical solution exists for the fields in the cavity yielding analytical expressions for Q_c and $\eta\prime$, a numerical optimization has been performed by choosing a shield-can geometry and finding the electrode geometry that would give the best stability in that case. In order to find the optimal resonator design, many iterations of this process were needed. Figure 5.2.2 shows the value of PT_2^2 plotted as a function of the electrode radius and length for a given shield can geometry. There is a maximum of the product PT_2^2 as a function of electrode geometry which indicates the optimal design for the resonator electrodes with this particular shield can geometry. The cavity geometry where this maximum occurs is determined by the collision rate of the atoms with the storage bulb walls, because the wall relaxation rate, γ_{2w}, will dominate PT_2^2. It is indicated from the equations above that the minimum Allan deviation can be achieved for larger storage bulb volumes. In fact, in the limiting case where $\gamma_t/\gamma_b \rightarrow 1$, $\sigma_l(\tau)$ is inversely proportional to the bulb volume. Therefore, if the overall cavity size is reduced, the stability is also reduced.

The Allan deviation can now be calculated for any given loop-gap cavity design. This is shown for three cases in figure 5.2.3. A cavity geometry designed using the maximum $\eta' Q_c$ criteria will have a narrow storage bulb and therefore a large wall relaxation rate. This is represented by curve C in figure 5.2.3. Curve B describes the predicted level of thermal fluctuations for the cavity shown in figure 2.2.3. Curve A represents the minimum fluctuations for a cavity with a shield-can diameter and

length equal to $7.5cm$ and electrodes $6.8cm$ in length and $3.2cm$ in radius. The level of fluctuations is reduced by a factor of three in going from the $\eta' Q_c$ geometry to the PT_2^2 design where $\sigma_l(1) = 6 \times 10^{14}$. The Allan deviation due to thermal fluctuations in this cavity would limit the stability at $\sigma_l(10000) = 6 \times 10^{-16}$. Also shown in figure 5.2.3 is the measured Allan deviation for an active maser currently in operation at the Naval Research Laboratory [53]. From about $10sec$ to $10^3 sec$ the calculated stability agrees with the measured results. Therefore, this compact maser design at $77K$ could be competitive with full-size room-temperature masers if the systematic effects listed in table 4.2.3 can be controlled.

CHAPTER 6

CONCLUSION

Hydrogen masers are the most stable frequency standards available. The applications of hydrogen masers in space programs like GPS are limited by the costs involved in launching full-size masers. Miniaturized masers have been suggested, including a loop-gap resonator design which reduces the size of the overall maser package but also reduces the cavity quality factor to a point such that hydrogen atoms cannot provide enough power to sustain self oscillation. As discussed in this thesis, a loop-gap resonator has been constructed with superconducting YBCO surfaces that reduce the cavity's power loss resulting in a Q_c of 31000. The loop-gap resonator has been evaluated as a $77K$ maser resonator. Noise measurements indicate that the resonator should be redesigned to minimize vibrations and frequency drift with temperature. The fields of the resonant mode have been calculated using a 3-d finite element program yielding an empirical relationship for the fields as a function of resonator geometry. This relationship is then used to optimize the cavity design for greatest maser stability. For comparison, a normal conducting loop-gap resonator at $77K$ has a Q_c of about 12000. This improvement of the Q_c, due to the superconducting electrodes, is enough so that this compact maser design can sustain self oscillation.

An electrophoretic process was used to create the superconducting thick film surfaces. The electrophoretic deposition of YBCO thick films on silver substrates

yields surface resistance values that are about 4 times lower than copper at $77K$ and $1.42GHz$. This thick film technique allows the deposition of superconducting films onto large non-planar surface areas. With the electrophoretic technique, a superconducting loop-gap resonator has been constructed in which the loop-gap electrode structure is completely covered with the YBCO material. The total superconducting surface area in the resonator considered here is about $160cm^2$.

The loop-gap resonator is a simple resonant device that has been successfully used for many applications. An exact solution for the fields of the loop-gap does not exist and therefore, empirical relations have, in the past, been developed to qualitatively describe the fields, energy, frequency, quality factor and filling factor of the cavity. These empirical descriptions of the rf fields have failed to consider features of the field profile that are expected from the high frequency boundary conditions. In this thesis, a new approach is introduced in which the loop-gap is considered to be a type of stripline device. Considering the loop-gap electrodes as stripline conductors above a ground plane (where the shield-can is the ground plane) leads to the conclusion that the rf magnetic fields are greatly enhanced at the edges of the electrodes. Such a field distribution is known to exist around stripline conductors. The existence of the field enhancement at the electrode edges is manifested as a power dependence in the measured YBCO surface resistance. The three dimensional finite element code MAFIA was used to confirm the field distributions, calculate the filling factor and find the cavity quality factor for this type of resonator.

With the results from the MAFIA calculations, the cavity geometry has been optimized to yield the minimum Allan deviation of frequency fluctuations from thermal noise within the linewidth of the hyperfine transition. The optimized cavity design is calculated to have an Allan deviation of $\sigma_l(10000) = 5 \times 10^{-16}$. This indicates that there is no fundamental reason why the compact superconducting hydrogen maser would not achieve nearly the same stability measured in a full size active maser.

There are known difficulties to operating a maser at liquid nitrogen temperatures. The relaxation rates, frequency shifts and frequency shift sensitivities have been calculated to determine which parameters of maser operation will dominate the systematic fluctuations in the oscillating maser. The temperature sensitivity of the compact maser places strict limitations on the allowable temperature fluctuations of the maser cavity. The sensitivity of the maser frequency to temperature fluctuations requires that the cavity temperature must be constant to $3.6 \times 10^{-5} K$ (considering that a redesigned cavity has reduced cavity pulling temperature sensitivity and the wall shift sensitivity is dominant). This is within the limit of achievable temperature control as suggested in reference [20]. Therefore, the systematic fluctuations of frequency due to temperature drift should allow frequency control better than 1×10^{-15}, which is more than an order of magnitude better than current GPS frequency standards.

It is concluded from the above summary that the superconducting compact hydrogen maser presents a challenging yet feasible opportunity for a compact highly

stable frequency source. Several aspects mentioned above deserve further consideration. The cavity should be redesigned to minimize mechanical vibrations. The results of the HTSSE project can be used to determine the degradation of the YBCO superconducting properties in the space environment. Furthermore, the dc magnetic field behavior of the maser cavity with a superconducting shield-can needs further investigation and development. Finally, servo techniques for temperature and frequency control of the maser oscillator will need to be developed and applied to this particular application.

REFERENCES

[1] H. Chaloupka and H. Piel, Proc. of the 3rd Workshop on RF Supercond., K. W. Shepard,ed., Argonne National Lab., ANL-PHY-88-1, 273 (1988).

[2] D. E. Oates, A. C. Anderson and P. M. Mankiewich, *J. of Supercond.* **3** , 251 (1990).

[3] H. E. Peters, *Proc. of the 32nd Annual Symp. on Freq. Control*, 469, 1978.

[4] S. Wolf, Naval Research Lab., Washington D.C., private communication.

[5] R. F. C. Vessot et al., *16th Annual PTTI*, 357 (1984).

[6] M. Desaintfuscien, J. Venniet and C. Audion, *Metrologica* **13**, 125 (1977).

[7] N. W. Ashcroft and N. D. Mermin, *Solid State Physics*, Saunders College, Phila. PA, 1976.

[8] T. G. Bednorz and K. A. Müller, *Z. Phys.*. **B64**, 189 (1986).

[9] G. Müller et al., *J. Supercond.* **3**, 235 (1990).

[10] N. McN. Alford, ICI U.K., private communication.

[11] C. W. Turner and T. Van Duzer, *Principles of Superconductive Devices and Circuits*, North Holland, New York, 1981.

[12] M. Tinkham, *Introduction to Superconductivity* , McGraw-hill, New York, 1975.

[13] J. P. Gordon, H. J. Zeiger and C. H. Townes, *Phys. Rev.* **99**, 1264 (1955).

[14] E. M. Purcell and R. V. Pound, *Phys. Rev. bf 81*, 279 (1951).

[15] D. Kleppner, H. C. Berg, S. B. Crampton, N. F. Ramsey, R. F. C. Vessot, H.

E. Peters and J. Vanier, *Phys. Rev.* **A 138**, 972 (1965).

[16] D. B. Opie, et al, *Proc. of the 45th Annual Symp. on Freq. Control*, 1991.

[17] D. A. Howe, D. W. Allan and J. A. Barnes, *Proc. of the 35th Annual Symp. on Freq. Control*, pp. 1-47 (1981).

[18] F. L. Walls and David W. Allan, *Proc. IEEE* **74**, No. 1, 162 (1986).

[19] R. F. C. Vessot,*22nd Annual PTTI Applications and Planning Meeting*, 29 (1990).

[20] E. M. Mattison, *22nd Annual PTTI Applications and Planning Meeting*, 453 (1990).

[21] R. F. C. Vessot, et al., *IEEE Trans. UFFC* **34**, 622 (1987).

[22] A. J. Berlinsky and W. N. Hardy, *13th Annual PTTI*, 547 (1982).

[23] D. J. Shaw, *Electrophoresis*, Academic Press, New York, 1969.

[24] M. Hein et al., ICMC Topical Conference on High Temperature Superconductors, May 1990.

[25] D. Wehler, Diplom Arbeit, Universität Wuppertal, Germany.

[26] N. Koura, et al., *J. Electrochem. Soc. Japan* **56**, 208 (1988).

[27] M. Hein et al., *J. Appl. Phys.* **66**, 5940 (1989).

[28] C. C. Schüler, et al., MRS Fall Meeting, Boston, 1989.

[29] J. Deslandes, et al., *Solid State Commun.* **71**, 407 (1989).

[30] H. J. Scheel, *Physica* **C153-155**, 44 (1989).

[31] B. Souletie, et al., *Solid State Commun.* **78**, 717 (1991).

[32] J. D. Jackson, *Classical Electrodynamics*, J. Wiley and Sons, Inc., New York,

1975.

[33] J. R. Delayen, C. L. Bohn and C. T. Roche, *J. Supercon.* **3**, 243 (1990).

[34] S. R. Stein and J. P. Turneare, *Proc. of the 27th Annual Symp. on Freq. Control*, 414. (1973).

[35] F. Habbal and W. C. H. Joiner, *J. of Low Temp. Phys.* **28**, p.83 (1977).

[36] G. J. Van Gurp, *Phys. Rev.* **B 166**, 436 (1968).

[37] J. R. Clem, *Phys. Rev.* **B1**, 2140 (1970).

[38] H. Bittel, *Physica* **83B**, p.6 (1976).

[39] H. M. Choe and A. van der Ziel, *Physica* **81B**, 237 (1976).

[40] Y. Song et al., *Phys. Rev. Lett.* **66**, 825 (1991).

[41] J. A. Testa et al., *Phys. Rev.* **B38**, 2922 (1988).

[42] Y. Zhu et al,. *Appl. Phys. Lett.* **54**, 374 (1989).

[43] A. Meada et al., Physica **C162-164**, 1203 (1989).

[44] S. Feng et al., *Phys. Rev. Lett.* **56**, 1960 (1986).

[45] T. E. Parker and K. Montress, *Tutorial Presented at the 40th Annual Symp. on Freq. Control* , May 28 1991.

[46] Wittke and Dicke, *Phys. Rev.* **103**, 620 (1954).

[47] D. Kleppner, Goldenberg and N. F. Ramsey, *Phys. Rev.* **123**, 603 (1962).

[48] R. F. C. Vessot, E. M. Mattison and E. Imbier, *Proc. of the 37th Annual Symp. on Freq. Control*, 49 (1983)

[49] J. Vanier and C. Audion, *The Quantum Physics of Frequency Standards*, Adan Hilger, Phila. PA USA, 1989.

[50] E. M. Mattison and R. F. C. Vessot, *22nd Annual PTTI Applications and Planning Meeting*, (1990).

[51] George Furukawa, NIST, Washington D. C., private communication.

[52] N. Yahyabey, P. Lesage and C. Audion, *IEEE Trans. Instr. and Meas.* **38**, 74 (1989).

[53] H. Peters, H. B. Owings and P. A. Koppang, *22nd Annual PTTI Applications and Planning Meeting*, 283 (1990).

[54] U. E. Isrealsson and D. M. Strayer, *IEEE Trans. Mag.* **27**, (1991).

[55] G. B. Collins, *Microwave Magnetrons*, Maple Press Co., York, PA, 1948.

[56] M. Mehdizadeh and T Koryu Ishii, *IEEE Trans. Micro. Theory and Tech.* **37**, (1989).

[57] W. Fronsicz and J. S. Hyde, *J. of Mag. Resonance* **47**, 515 (1982).

[58] V. A. Bochov, et al., *Radio Eng. and Electr. Physics* **26**, 151 (1981).

[59] E. J. Denlinger, *IEEE Trans. Micro. Theory and Tech.* **19**, (1971).

[60] T. G. Bryant and J. A. Weiss, *IEEE Trans. Micro. Theory and Tech.* **16**, (1968).

[61] H. A. Wheeler, *IEEE Trans. Micro. Theory and Tech.* **13**, 172 (1965).

[62] J. C. Maxwell, *A Treatise on Electricity and Magnetism*, 3rd ed., vol. 1, New York: Dover, 1954, pp. 296-297.

[63] J. Fikioris et al., *IEEE Trams. Micro. Theory and Tech.* **37**, 21 (1989).

[64] H. Piel, et al., *Physica* **C 153-155**, 1604 (1988).

[65] R. F. Feynman, et al., *The Feynman Lectures on Physics*, vol. 3, Addison-Wesley, Reading Mass., 1965.

[66] N. A. Demidov and A. A. Uljanov, *22nd Annual PTTI Applications and Planning Meeting*, 187 (1990).

[67] MAFIA; see T. Weiland *Part. Accel.* **15**, pp. 245-292 (1984).

[68] C. G. Kuper, *An Introduction to the Theory of Superconductivity*, Clarendon Press, Oxford, 1968

[69] A. Portis and M. Hein, Internal Report, University of Wuppertal, January, 1991.

[70] T. C. Choy and A. M. Stoneham, *Proc. R. Lond.* A **434**, 555-570 (1991).

[71] A. S. Brust, Diplom Arbeit, Universität Wuppertal, Germany.

[72] M. K. Wu, et al., *Phys. Rev. Lett.* **58**, 908 (1987).

VITA

David B. Opie Was born June 16, 1961 in Flint, Michigan. Graduated from Brighton High School, in that city in June, 1979. Recieved B.A. of Arts and Science from the University of Delaware in June, 1986. In August of 1986 he began graduate studies in Physics at the College of William and Mary in Virginia, where he earned an M.S. in May, 1988.